HARVARD UNIVERSITY
Graduate School of Arts and Sciences

THESIS ACCEPTANCE CERTIFICATE

The undersigned, appointed by the

Division of Engineering and Applied Sciences

have examined a thesis entitled

"First Principles Studies of Interface Interactions and Their Implications for Heterogeneous Catalysis and Novel Electronic Devices"

presented by Su Ying Quek

candidate for the degree of Doctor of Philosophy and hereby certify that it is worthy of acceptance.

Signature .....
Typed name: Professor E. Kaxiras

Signature .....
Typed name: Professor C. Friend

Signature .....
Typed name: Professor M. Aziz

Date: September 25, 2006

First principles studies of interface interactions and their implications for heterogeneous catalysis and novel electronic devices

A thesis presented by

Su Ying Quek

to

The Division of Engineering and Applied Sciences

in partial fulfillment of the requirements

for the degree of

Doctor of Philosophy

in the subject of

Applied Physics

Harvard University

Cambridge, Massachusetts

September 2006

INFORMATION TO USERS

The quality of this reproduction is dependent upon the quality of the copy submitted. Broken or indistinct print, colored or poor quality illustrations and photographs, print bleed-through, substandard margins, and improper alignment can adversely affect reproduction.

In the unlikely event that the author did not send a complete manuscript and there are missing pages, these will be noted. Also, if unauthorized copyright material had to be removed, a note will indicate the deletion.

ProQuest Information and Learning Company
300 North Zeeb Road
P.O. Box 1346
Ann Arbor, MI 48106-1346

Dissertation Advisor: Professor Efthimios Kaxiras Su Ying Quek

Dissertation Co-advisor: Professor Cynthia M. Friend

First principles studies of interface interactions and their implications for heterogeneous catalysis and novel electronic devices

Abstract

Nanoscale and surface-mediated materials are of extreme current interest in a wide range of fundamental fields, from heterogeneous catalysis to molecular electronics. The properties of these materials frequently differ from well-established bulk properties, and in particular, are especially sensitive to the nature of their atomic-scale geometry and electronic structure. In this work, I shall present first principles studies of the electronic properties of four different surface-related systems. First, we propose an atomic-scale model for novel commensurate MoO_3 monolayers on Au(111), and explore the implications of interface interactions on catalysis. Second, we extend our work to a model catalyst: Au(110) films on ultrathin titania, where we consider the impact of changes in interface interactions on O_2 adsorption. Third, we propose an atomic-scale model for an incommensurate, ordered, two-dimensional AuS layer on Au(111). Our model is remarkably robust, reflects the rich coordination chemistry of Au, and reproduces experimental observations. Finally, we consider cyclopentene on Si(001), a prototypical organic/Si system which exhibits negative differential resistance (NDR) in

low temperature STM experiments. We examine the electronic coupling and level alignment in this and related systems, and discuss general implications for NDR in silicon-based molecular electronics.

Table of Contents

Acknowledgements

Penning this section is perhaps the most relaxing step toward completing my thesis. It is also arguably one of the most important. I am indebted to numerous mentors, teachers, colleagues, friends and family members, without whom the ensuing pages would never have been written.

I am immensely grateful to my advisor, Professor Efthimios Kaxiras, for giving me the opportunity to take the path of a computational physicist. Through his guidance, I learnt research skills that will undoubtedly remain highly relevant throughout my research career. He was flexible and understanding, and placed me in contact with many scientists from whom I also learnt a great deal.

I am also extremely grateful to my co-advisor, Professor Cynthia M. Friend, for her valuable guidance in chemistry and surface science, as well as for her warmth in welcoming me to her group. She and her group have equipped me with knowledge about experimental technicalities as well as the ability to critically assess literature reports on experimental surface science.

I would like to express my appreciation to numerous other Harvard faculty for their excellent tutorship, including Professors Michael Tinkham, David Nelson, Lene Hau, Roger Brockett, Donald Anderson, and my thesis committee member Professor Mike Aziz.

Professor Umesh Waghmare is someone I have learnt a great deal from even though we have never met in person. Thanks also go to Joydeep Bhattacharjee and Jonathan Yates for sharing with me their knowledge and insights into Wannier orbitals.

I am also privileged to have worked with Professor Steven G. Louie and his group, and would like to thank him for his hospitality and guidance during the final year of my studies. I am grateful to have worked closely with Jeff Neaton, from whom I gained many insights into physics as well as tips on presentation skills. It was my great fortune too to have worked with Mark Hybertsen. Interacting with him is somewhat like taking a booster shot because you always get so much out of one sitting.

It has also been my pleasure to be a member of the Kaxiras and Friend groups, as well as a visiting member of the Louie group. I would like to thank everyone in the Kaxiras and Friend groups for coming to my thesis defense: Maria, Mike, Meng Sheng, Wenguang, Yina, Dilini, Tom (thanks a lot for the placards!), Ryan, Xiaoying, Weiwei, Ling, and Andreas. Thanks especially to Maria, Mike, Vincenzo, Xiaoying, Dilini, Tom, Ryan, Weiwei, Meng Sheng, Young-Shin, Xingyi and Jeff for their humor and encouragement leading up to my defense. Over the years, I have benefited from scientific discussions with Gang, Argyrios, Paul, Mike, Juergen, Monika, Xingyi, Byoung-Koun, Tom, Young-Woo, Amy, Jack, Manos, Cheol-Hwan, Nick and David Prendergast. I would especially like to thank Juergen, Monika and Xingyi, with whom I worked closely. The following are people I interacted most with and who have made the lab an especially enjoyable place: Argyrios, Mike, Maria, Vincenzo, Amy, Jack, Nick, Young-Woo, Manos, Cheol-Hwan, Jay and Kim. It has also been a great pleasure to have known and worked with Richard Schalek. Thanks also go to our custodian, Dennis, and group secretaries, Wanda, Julie and Katherine, who maintained our working conditions in tip-top shape.

I would also like to thank Meishan, Jialu, Shirleen, Shu Sin and Brenda for their support. Special thanks to Jialu for generously offering me a place to stay in my final year. I would especially like to thank her for providing a conducive working environment for me prior to my defense, and for her cheerful brand of encouragement. Thanks to Jialu, Shu Sin and Shirleen for coming to my defense.

I owe a big thank you to my parents and sister, Su Juian, for their unceasing support and encouragement. I am also grateful to my parents-in-law and sister-in-law, Huanqian, for their words of encouragement.

I am indebted to my husband, Zhi Heng, for his patience, humor and moral support. He is a key pillar to my successful completion of this thesis, for it was he who strongly encouraged me to pursue my interest in computational materials science, even though my background was in mathematics.

Glossary of Acronyms

AO	Atom-centered localized Wannier Orbital
BO	Bond-centered localized Wannier Orbital
CVD	Chemical Vapor Deposition
DFT	Density Functional Theory
EELS	Electron Energy Loss Spectroscopy
GGA	Generalized Gradient Approximation
GW	A many-body perturbative approach to calculating the electron self-energy (G is the dressed Green's function, W is the screened Coulomb interaction)
LDA	Local Density Approximation
LEED	Low Energy Electron Diffraction
NDR	Negative Differential Resistance
PW91	Perdew-Wang 91 exchange-correlation functional
PVD	Physical Vapor Deposition
STM	Scanning Tunneling Microscopy
XPS	X-ray Photoelectron Spectroscopy

Chapter 1

Introduction

Advances in experimental techniques have resulted in the growth of many interesting and novel systems. Examples include surface-mediated metastable phases[1-4] (materials that are not stable in isolation or as bulk materials, but are stabilized by an underlying substrate), such as a well-ordered $Al_{10}O_{13}$ film that forms on the NiAl(100) surface.[4] However, progress is often hampered by the lack of an atomistic-scale understanding of these materials. In this context, first-principles calculations can play a role by providing some degree of atomic-scale modeling that can aid in material characterization or the prediction of new properties.

The content of this thesis centers around two main, complementary, objectives. One is to determine the atomic structure of novel materials, synthesized by my co-workers in the Friend lab. The second is to understand why these systems are stable, and in some cases, to make predictions on their properties. In conjunction with this work, we also seek to understand experimental observations in other systems that have potential applications as catalysts or molecular electronic devices, as well as make predictions on related materials.

The thesis is divided into six Chapters. Following the introduction in Chapter 1, I provide in Chapter 2 an overview of the theoretical concepts employed in this work. Chapter 3 describes an atomic-scale model for commensurate MoO_3 monolayers synthesized on Au(111), and discusses its implications for catalysis. In Chapter 4, I discuss O_2 adsorption on a model oxidation catalyst: Au(110) thin films on ultrathin

layers of titania supported on a molybdenum substrate. In Chapter 5, I return to the topic of proposing atomic-scale models for novel materials, but this time, for a more complex, incommensurate system, a AuS layer on Au(111). We introduce fresh approaches within density functional theory to take into account charge transfer in the incommensurate system, and the resulting model is consistent with experimental observations and is remarkably robust. It has previously been proposed that negative differential resistance (NDR) can occur through a resonant tunneling mechanism in organic/Si systems. Our focus here is to assess the possibility of resonant tunneling NDR in specific systems, such as cyclopentene on Si(001) (a prototypical organic/Si system). Through our studies, we seek to provide guidelines for optimizing the conditions for resonant tunneling NDR in Si-based molecular electronics.

One unifying theme in Chapters 3-6 is the importance of interface interactions. For example, we find that the MoO_3 monolayer on Au(111) (Chapter 3) is remarkably flexible and can distort to fit the Au surface, suggesting the possibility of tuning the properties of monolayer transition metal oxides using interface interactions. The resulting strain in the oxide layer also enhances H adsorption. In Chapter 4, we find that O_2 adsorption is stabilized as a result of changes in the Au/titania interface interactions during the adsorption process, an effect that is related to the flexibility of ultrathin titania films. On the other hand, even in the incommensurate AuS layer, in which intra-layer bonds are weaker than bonding with the Au substrate, we find that interface interactions in the form of charge transfer are important in explaining the robustness of the structure, as well as the experimentally observed unit cell size. Finally, the nature of electronic coupling between the organic molecule and its silicon substrate plays a major role in

affecting the possibility of resonant-tunneling NDR in the system. In particular, we find that the resonant tunneling mechanism requires the existence of molecular states that are weakly coupled to the substrate and close enough to the Si band edges.

References

[1] J. C. Love, L. A. Estroff, J. K. Kriebel, R. G. Nuzzo, and G. M. Whitesides, Chem. Rev. **105**, 1103 (2005).

[2] C. T. Campbell, Surf. Sci. Rep. **27**, 1 (1997).

[3] M. M. Biener, J. Biener, and C. M. Friend, Langmuir **21**, 1668 (2005).

[4] G. Kresse, M. Schmid, E. Napetschnig, M. Shishkin, L. Köhler, and P. Varga, Science **308**, 1440 (2005).

Chapter 2

Theoretical Concepts

2.1 Landau Quasiparticles and the single-particle approximation

The electronic structure of a system can only be determined exactly by solving the many-body Schrödinger equation:

$$H\Psi = E\Psi \tag{2.1.1}$$

where Ψ, the many-body wavefunction is a function of the positions r_i of each and every electron in the system, and H, the many-body Hamiltonian, is given by

$$H = T + V_{ext} + V_{many-body}, \tag{2.1.2}$$

$$T = -\sum_i \frac{\hbar^2}{2m}\nabla_i^2, \tag{2.1.3}$$

$$V_{ext} = \sum_i V_{ion}(r_i), \tag{2.1.4}$$

$$V_{many-body} = \sum_{ij} V(r_i, r_j) \equiv \sum_{ij} \frac{e^2}{|r_i - r_j|}. \tag{2.1.5}$$

Solving the many-body Schrödinger equation is currently intractable for most systems. However, considerable insight into the problem can be obtained by conceptualizing the sea of electrons as a system of weakly-interacting quasiparticles. The quasiparticles, introduced by Landau, represent some form of collective excitations of the original strongly-interacting particles (in this case, electrons). Landau's idea for describing the properties of a system of strongly-interacting particles with those of weakly-interacting quasiparticles, has worked remarkably well. The quasiparticles that

are relevant here can be thought of as 'dressed' electrons, or bare electrons that are surrounded by a cloud of constantly changing holes and electrons.

While the introduction of quasiparticles greatly simplifies the strongly-interacting many-body problem, it is still difficult to solve for the quasiparticle spectra exactly. Importantly, however, the weak interactions between quasiparticles make the quasiparticle problem amenable to perturbation theory.[1] Specifically, the long-range inter-electron interaction $V(\boldsymbol{r}, \boldsymbol{r}')$ can be replaced by a weaker , dynamically screened Coulomb interaction $W(\boldsymbol{r}, \boldsymbol{r}, t, t')$. The quasiparticle energies can then be calculated to first order in W; this is known as the GW approximation and is described in Section (2.4).

Density-functional Kohn-Sham theory is the work-horse of electronic structure calculations and is significantly more scalable than the GW approximation. In this case, however, the corresponding "quasiparticles" are non-interacting, fictitious particles with no physical interpretation; therefore, the Kohn-Sham eigenvalues have little quantitative significance. We shall discuss this approach in greater detail in Section (2.3). In the next section, we briefly review another single-particle approximation (Hartree-Fock) which is instructive for the present discussion.

2.2 Hartree-Fock approximation

In the Hartree-Fock approximation, the many-body wavefunction Ψ is written as a Slater determinant of single-particle orbitals ϕ_k. The Slater-determinant is an antisymmetrized wavefunction (exchanging the positions of any two electrons flips the sign of Ψ), and thus exactly takes into account the Pauli exchange energy. A variational calculation involving ϕ_k yields the Hartree-Fock equation:

$$(-\frac{\hbar^2}{2m}\nabla^2 + V_{ext} + V_H)\phi_k(r) + \int dr' V_X^{HF}(r,r')\phi_k(r') = E_k\phi_k(r) \tag{2.2.1}$$

where

$$V_H(r) = \sum_{k'\neq k} \int dr' V(r,r')\phi_{k'}^*(r')\phi_{k'}(r') \tag{2.2.2}$$

and

$$V_X^{HF}(r,r') = -V(r,r')\sum_{k'\neq k}\phi_{k'}^*(r')\phi_{k'}(r). \tag{2.2.3}$$

The so-called Hartree potential $V_H(r)$ is the mean-field potential that an electron at r feels due to Coulomb interactions with all other electrons. $V_X^{HF}(r,r')$ is the exact exchange potential for the bare Coulomb interaction.

As we discuss below, the exact exchange term $V_X^{HF}(r,r')$ captures the exchange-correlation energy to first order in the bare Coulomb interaction $V(r, r')$; effects of electron correlations are completely omitted. Since $V(r, r')$ is a long-range interaction, the single-particle orbitals ϕ_k cannot be thought of as representing weakly interacting quasiparticles, nor can their eigenvalues E_k represent quasiparticle excitation spectra. Nonetheless, it can be shown that within the approximation in which correlations are neglected, the eigenvalue E_k of a filled (empty) orbital is equal to the change in total energy when an electron is removed from (added to) the system, i.e. decreasing (increasing) the size of the Slater determinant representing the wavefunction, by removing (adding) a row and column involving an orbital ϕ_k, *with all other orbitals unchanged*. This is known as Koopman's theorem.[2]

2.3 Density-functional Kohn-Sham approach

The density-functional Kohn-Sham approach is by far the most prevalent computational tool in electronic structure, because of its tractability for many molecular and extended systems, and its success in calculating *relative* total energies. The successful implementation of this approach follows several key propositions in the 1960s, the first of which were the Hohenberg-Kohn theorems in 1964.[3] The theorems state that: (I) For any system of interacting particles in an external potential $V_{ext}(\boldsymbol{r})$, the potential $V_{ext}(\boldsymbol{r})$ is determined uniquely (up to a constant) by the ground state particle density $n_0(\boldsymbol{r})$. (II) The total energy of a system can be defined as a universal functional $E[n(\boldsymbol{r})]$ of the density, for any external potential $V_{ext}(\boldsymbol{r})$. The exact ground state energy of the system is then given by the global minimum value of this functional; the corresponding density $n(\boldsymbol{r})$ is the exact ground state density $n_0(\boldsymbol{r})$. These theorems greatly simplify the many-body problem, since the many-body wavefunction does not need to be explicitly constructed, and in principle, one need only solve for the optimal density $n_0(\boldsymbol{r})$, which is a scalar quantity.

The practical implementation of the Hohenberg-Kohn theorems was, however, hindered by the difficulty in finding an explicit form of $E[n(\boldsymbol{r})]$. For instance, there is no known formula for obtaining the kinetic energy T in terms of $n(\boldsymbol{r})$. The widespread application of density functional theory today arises from an ansatz proposed by Kohn and Sham in 1965.[4] The Kohn-Sham approach is to replace the interacting many-electron system with a different auxiliary system of fictitious non-interacting particles for which an explicit expression for T can be written. This is accomplished by simultaneously replacing the original external potential with a new external potential felt by the fictitious

particles; this new potential in turn captures all the physics of inter-electron interactions. The many-electron interactions are included in a so-called exchange-correlation functional of the density $E_{xc}^{KS}[n(r)]$, and it is this functional which determines the accuracy of ground state densities and total energies obtained in the Kohn-Sham approach. Explicitly,

$$E_{xc}^{KS}[n] = \langle T \rangle - T^{KS}[n] + \langle V_{\text{int}} \rangle - E_H[n], \tag{2.3.1}$$

where $\langle T \rangle$ and $\langle V_{\text{int}} \rangle$ are the exact kinetic and potential energy terms respectively, $E_H[n]$ is the energy contribution from the mean-field Hartree potential $V_H(r)$:

$$E_H[n] = \frac{1}{2}\int dr V_H(r) n(r), \tag{2.3.2}$$

and

$$T^{KS}[n] = \sum_k \langle \phi_k | -\frac{\hbar^2}{2m}\nabla^2 | \phi_k \rangle, \tag{2.3.3}$$

where $\{\phi_k\}$ is the set of fictitious orbitals and $n = \sum_k |\phi_k|^2$.

In the density-functional Kohn-Sham approach, $E_{xc}^{KS}[n(r)]$ is implicitly assumed to be a local or nearly-local functional of the density, i.e.

$$E_{xc}^{KS}[n] = \int dr \varepsilon_{xc}([n(r)])n(r). \tag{2.3.4}$$

$\varepsilon_{xc}([n(r)])$ is in turn defined as a local or nearly-local functional of $n(r)$; the local density approximation (LDA) refers to the approximation of $\varepsilon_{xc}([n(r)])$ as a local functional of $n(r)$ alone, while the generalized gradient approximation (GGA) refers to that in which $\varepsilon_{xc}([n(r)])$ is defined as a functional of $n(r)$ and its gradients.

The resulting set of Kohn-Sham equations is given by:

$$(-\frac{\hbar^2}{2m}\nabla^2 + V_{ext} + V_H + V_{xc}^{KS}(n))\phi_k(r) = E_k\phi_k(r), \tag{2.3.5}$$

where

$$V_{xc}^{KS}[n] = \frac{\delta(\varepsilon_{xc}([n(r)]n(r))}{\delta n(r)}. \tag{2.3.6}$$

In comparison with the Hartree-Fock equations in (2.2.1), the Kohn-Sham equations (2.3.5) are much more tractable, since the integral term $\int dr' V_X^{HF}(r,r')\phi_k(r')$ involving the exact exchange is replaced by a simpler multiplicative exchange-correlation term $V_{xc}^{KS}[n]\phi_k(r)$.

The Kohn-Sham approach is designed to give accurate ground state densities and total energies, subject to the accuracy of $E_{xc}^{KS}[n(r)]$. Correlation effects typically constitute the weakest contribution to the total energy,[1] and it has been found that relative total energies can be determined reasonably well within density-functional Kohn-Sham theory using LDA or GGA. Since GGA takes into account gradients in $n(r)$, it is often preferred over LDA for finite systems where the spatial variation in $n(r)$ may be large. Empirical trends indicate that LDA (GGA) tends to result in equilibrium bond lengths that are shorter (longer) than experiment by a few %. The corresponding cohesive energies also tend to be slightly larger (smaller) than experiment. As the above trends are quite systematic, using a consistent exchange-correlation functional allows one to obtain insights into relative cohesive energies and atomic structures of systems with the same number and type of atoms. Of course, the Kohn-Sham approach cannot be used to study phenomena associated with correlations in strongly-correlated electron systems, such as superconductivity.

The eigenvalues of the Kohn-Sham *fictitious* single-particle orbitals have no physical meaning, but for one exception.[2] The highest eigenvalue E_{max} for an occupied orbital in a finite system is exact *if* $E_{xc}^{KS}[n(r)]$ is exact. This is because the asymptotic long-range density of a bound system is determined by the occupied state with the highest eigenvalue; since the density is assumed to be exact *if* $E_{xc}^{KS}[n(r)]$ is exact, so must E_{max}. Therefore, in principle, the ionization energies of molecules and the work functions of metal surfaces should be given correctly by exact Kohn-Sham theory, and the accuracy of these quantities in turn gives an indication of the accuracy of $E_{xc}^{KS}[n(r)]$. In practice, it has been found that LDA and GGA do not yield quantitative values of these properties. However, the *relative* values of ionization energies and work functions for similar compounds, calculated with the same functional for $E_{xc}^{KS}[n(r)]$, do compare reasonably well with experiment.[5, 6]

2.4 Electron self-energy: GW approximation

As discussed above, the density functional Kohn-Sham approach does not give quantitative information on the quasiparticle spectra in a system. Here, we review the GW approximation[7-9] to the electron self-energy. The quasiparticle excitations of the system are then given by the sum of electron self-energies and Kohn-Sham eigenvalues (excluding the local exchange and correlation contribution $E_{xc}^{KS}[n(r)]$). The implementation employed here has no adjustable parameters and has yielded quasiparticle spectra in excellent agreement with photoemission experiments, for bulk, surface and molecular systems involving semiconductors and simple metals.[10]

2.4.1 Electon self-energy

The electron self-energy $\Sigma(r,r',E_k)$ of a quasiparticle with energy E_k is defined as the energy the electron gains by interating with itself via the many-body system, changing its own energy. The quasiparticle energies and wavefunctions are solutions to

$$(T+V_{ext}+V_H)\psi_{nk}(r)+\int dr'\Sigma(r,r',E_{nk})\psi_{nk}(r')=E_{nk}\psi_{nk}(r) \qquad (2.4.1)$$

(2.4.1) is analogous to the Hartree-Fock and Kohn-Sham equations above; the self-energy term Σ is included in an approximate manner in Hartree-Fock as the exact exchange term $V_x^{HF}(r,r')$ (excluding correlations) and in the Kohn-Sham theory as the local exchange and correlation term, $V_{xc}^{KS}(r)$. However, the full many-body self-energy operator is distinct in that it is non-local and is a function of the quasiparticle energy E_k. In general, E_k is complex; the real part gives the excitation spectra and the imaginary part the inverse-lifetime of the quasiparticle. Notice that the band index n has been included explicitly in (2.4.1).

In the GW approximation, the self-energy operator is given by

$$\Sigma(r,t,r',t')=iG(r,t,r',t')W(r,t+\delta,r't'), \qquad (2.4.2)$$

where $\delta=0^+$, G is the dressed one-electron Green's function, and W is the dynamically screened Coulomb interaction between electrons. This is the first-order term in the expansion of Σ as a function of W. This approximation is equivalent to neglecting the influence on the self-energy of any variations in the average potential, or neglecting so-called "vertex corrections".[7] It can be shown that the expansion parameter involving W is strictly < 1 in the electron gas.[11] $\Sigma(r,r',E_k)$ is simply given by the Fourier Transform

of $\Sigma(r,t,r',t')$ relative to $(t-t')$. In the GW approximation, Σ is non-local and energy-dependent. Fourier transforming (2.4.2) to energy space gives:

$$\Sigma(r,r',E) = i\int\frac{dE'}{2\pi}\exp(-i\delta(E-E'))G(r,r',E')W(r,r',E-E') \tag{2.4.3}$$

It is instructive to compare the GW self-energy term with the corresponding term in Hartree-Fock. If Σ is expanded as a function of the bare electron-electron Coulomb interaction V, instead of the screened interaction W, the analogous first-order expansion term is in fact the exact exchange in Hartree-Fock.[7]

$$\Sigma^{HF}(r,t,r',t') = iG(r,t,r',t')V(r,r')\delta(t-t'+\delta) \tag{2.4.4}$$

where $\delta = 0^+$. The Fourier transform of (2.4.4) gives

$$\Sigma^{HF}(r,r',\varpi) = -V(r,r')\sum_{k'\neq k}\phi^*_{k'}(r')\phi_{k'}(r) = V_X^{HF}(r,r'). \tag{2.4.5}$$

In the context of the discussion on Landau's quasiparticles in Section 2.1, V represents the strong long-range interaction between electrons while W represents the weak interaction between dressed electrons (quasiparticles) in the system. It is therefore clear that the GW approximation is superior to Hartree-Fock, since the terms neglected in the respective first-order expansions are much smaller in the former. Computing Σ in the GW approximation amounts to finding the best approximations to G and W.

2.4.2 The one-electron Green's function

Given a system of N electrons in its ground state $|N\rangle$, the one-electron Green's function is defined[7] as

$$G(r,t,r',t') = -i\langle N|T[\psi(r,t)\psi^+(r',t')]|N\rangle, \tag{2.4.6}$$

where the time-dependent field operator $\psi(r,t)$, which acts to destroy an electron at (r, t) is given by

$$\psi(r,t) = e^{iHt}\psi(r)e^{-iHt}, \tag{2.4.7}$$

$$\psi(r) = \sum_k a_k \phi_k(r), \tag{2.4.8}$$

with a_k defined as the annihilation operator on the kth single-particle orbital $\phi_k(r)$. The subscript + denotes the corresponding creation operators (Hermitian conjugates) and the operator T, Wick's time-ordering operator, orders operators so that the smallest times are on the right. On the basis of time invariance, G depends on time through $\tau = t - t'$.

As an illustration, consider a gas of free non-interacting electrons labeled by momentum k. Here, translation invariance implies that G depends on space through $r - r'$. Then

$$G(k,\tau) = -i(1-n_k)\exp(-i\varepsilon_k\tau)\Theta(\tau) + in_k \exp(-i\varepsilon_k\tau)\Theta(-\tau), \tag{2.4.9}$$

where n_k is the occupation number of the state with energy ε_k and Θ is the Heaviside function. Fourier transforming from time to energy space yields

$$G(k,E) = \frac{1}{E - \varepsilon_k + i\,\mathrm{sgn}(\varepsilon_k - \mu)\delta}, \tag{2.4.10}$$

where $\delta = 0^+$. Excitations corresponding to injected electrons or holes in the free electron gas therefore appear as poles in the Green's function. The poles are in the upper half complex plane for injected holes, and in the lower half plane for injected electrons.

Moving on now to the interacting electron gas, the free electron Green's function above is generalized through the introduction of a spectral function $A(r,r',E)$, which

can be thought of as serving to mix the mean field states. The resulting dressed Green's function is given by[7]

$$G(r,r',E) = \int_C dE' \frac{A(r,r',E')}{E - E'}. \tag{2.4.11}$$

The contour C runs infinitesimally above the real axis for $E' < \mu$, and infinitesimally below the real axis for $E' > \mu$, with μ being the chemical potential. An equivalent expression[7] in the space spanned by a complete orthonormal set of single-particle states $\phi_k(r)$ is

$$G(k,k',E) = \int_C dE' \frac{A(k,k',E')}{E - E'}, \tag{2.4.12}$$

where

$$A(k,k',E) = \int \phi_k^*(r) A(r,r',E) \phi_{k'}(r') dr dr'. \tag{2.4.13}$$

It is immediately clear that in the free electron case, the spectral function is

$$A(k,E) = \delta(E - \varepsilon_k). \tag{2.4.14}$$

The key effects of many-electron interactions are to smear out and shift the delta functions in the spectral function. Since the spectral function typically remains sharply peaked in energy, the quasiparticle picture is a meaningful concept.[11] The poles in the Green's function give the quasiparticle energies E_k. The real part of E_k corresponds to the peak position in A, and the imaginary part the peak width (or inverse lifetime of the quasiparticle).

An iterative approach is used to calculate G.[11] First, the LDA Kohn-Sham eigenstates ϕ_{nk} and eigenvalues ε_{nk} are obtained (the exchange-correlation term is later substracted away and replaced by the GW self-energy, so that the final result is not

sensitive to the form of the exchange-correlation potential). Within this single-particle picture, the Green's function G is given by

$$G(r,r',E) = \sum_{nk} \frac{\phi_{nk}(r)\phi_{nk}^{*}(r')}{E - \varepsilon_{nk} - i\delta_{nk}}. \tag{2.4.15}$$

where $\delta_{nk} = 0^{+}$ for $\varepsilon_{nk} < \mu$ and $\delta_{nk} = 0^{-}$ for $\varepsilon_{nk} > \mu$. The corresponding spectral function is

$$A(r,r',E) = \sum_{nk} \phi_{nk}(r)\phi_{nk}^{*}(r')\delta(E - \varepsilon_{nk}). \tag{2.4.16}$$

The approximation here is thus that the quasiparticle excitation energies (peaks in A) are given by the Kohn-Sham eigenvalues ε_{nk}, and that the particle lifetime is infinite. To improve upon this approximation, ε_{nk} in (2.4.16) can be iteratively replaced with the quasiparticle energy E_{nk} calculated using the expression for G in (2.4.15). In practice, it is found that only a single additional iteration is required to give fairly converged results. The only remaining assumption is then that the quasiparticle lifetime is long enough to neglect the imaginary part of the quasiparticle energy E_{nk}.

2.4.3 The dynamically screened Coulomb interaction

The dynamically screened Coulomb interaction between electrons, W, is given by

$$W(r,r',t,t') = \int dr''dt''\varepsilon^{-1}(r,r'',t,t'')V(r,r''), \tag{2.4.18}$$

$$W_{GG'}(q,\omega) = \varepsilon^{-1}_{GG'}(q,\omega)V(q+G'), \tag{2.4.19}$$

where the Fourier transform is defined by

$$W(r,r',t,t') = \frac{1}{\Omega}\sum_{qGG'} e^{i(q+G).r} W_{GG'}(q,\omega) e^{-i(q+G').r'}. \tag{2.4.20}$$

and similarly for the inverse dielectric matrix ε^{-1}.

To calculate the full dynamical ε^{-1}, we adopt a generalized plasmon pole model,[11] which extends the static ε^{-1} to finite frequencies by assuming that

$$\mathbf{Im}\,\varepsilon^{-1}_{GG'}(q,\omega) = A_{GG'}(q)[\delta(\omega - \tilde{\omega}_{GG'}(q)) - \delta(\omega + \tilde{\omega}_{GG'}(q))] \tag{2.4.21}$$

and

$$\mathbf{Re}\,\varepsilon^{-1}_{GG'}(q,\omega) = 1 + \frac{\Omega^2_{GG'}(q)}{\omega^2 - \tilde{\omega}^2_{GG'}(q)}, \tag{2.4.22}$$

with Ω defined below. Realistic calculations indicate that $\mathbf{Im}\,\varepsilon^{-1}_{GG'}(q,\omega)$ is generally a peaked function of ω. The approximation in (2.4.21) is to replace these peaks by delta functions at plasmon pole frequencies $\tilde{\omega}$. This amounts to assuming that the spectral function for the screened interaction is a single narrow peak in frequency for each set of momentum components. It has been found that (2.4.22) approximates $\mathbf{Re}\,\varepsilon^{-1}_{GG'}(q,\omega)$ reasonably well for frequencies small compared to $\tilde{\omega}$, which is the important frequency range for the Σ calculations. Furthermore, the expression for Σ involves an average over $\mathbf{Re}\,\varepsilon^{-1}_{GG'}(q,\omega)$, so that only its average dependence on frequency is important.

The effective bare plasma frequency Ω, introduced in (2.4.22) and defined below, can be calculated from the charge density of the system while $\tilde{\omega}$ and A can be determined exactly from Ω and the static ε^{-1} with no adjustable parameters. Specifically, $\tilde{\omega}$ and A are obtained by solving two simultaneous equations:

$$\mathbf{Re}\,\varepsilon^{-1}_{GG'}(q,\omega = 0) = \delta_{GG'} + \frac{2}{\pi} P \int_0^\infty d\omega \frac{1}{\omega} \mathbf{Im}\,\varepsilon^{-1}_{GG'}(q,\omega) \tag{2.4.23}$$

and

$$\int_0^\infty d\omega\omega\, \mathbf{Im}\,\varepsilon^{-1}_{GG'}(q,\omega) = -\frac{\pi}{2}\omega_p^2 \frac{(q+G).(q+G')}{|q+G|^2} \frac{\rho(G-G')}{\rho(0)} \equiv -\frac{\pi}{2}\Omega^2_{GG'}(q) \tag{2.4.24}$$

(2.4.23) is the Kramers-Kronig relation and (2.4.24) is an exact sum rule, with ω_p and Ω being the plasma frequency and effective plasma frequency respectively. The resulting solutions for $\tilde{\omega}$ and A are:

$$\tilde{\omega}^2_{GG'}(q) = \frac{\Omega^2_{GG'}(q)}{1-\varepsilon^{-1}_{GG'}(q,\omega=0)}, \tag{2.4.25}$$

$$A_{GG'}(q) = -\frac{\pi}{2}\frac{\Omega^2_{GG'}(q)}{\tilde{\omega}_{GG'}(q)}. \tag{2.4.26}$$

The static ε^{-1}, which enters the final result for frequency-dependent ε^{-1} via (2.4.25), is calculated from first principles within the random phase approximation (RPA).[12] The procedure is first, to use first-order perturbation theory to calculate the charge density ρ induced by the total potential ϕ and next, to calculate the induced potential ϕ_{ind} ($\phi_{ind} = \phi - \phi_{ext}$) from ρ_{ind} ($\rho_{ind} = \rho - \rho_{ext}$) using Poisson's equation. The second step implicitly ignores the contribution to ϕ_{ind} of the exchange and correlation effects arising from the induced charge ρ_{ind}. It was found that explicitly including this exchange and correlation effect does not change the result for Σ significantly. The final RPA result for a free electron gas is

$$\varepsilon(q) = \frac{\phi_{ext}(q)}{\phi(q)} = 1 - \frac{4\pi e^2}{q^2}\sum_k \frac{f(k)-f(k+q)}{E(k)-E(k+q)}. \tag{2.4.27}$$

In a crystal, the RPA result for static ε is:[9]

$$\varepsilon_{GG'}(q) = \delta_{GG'} - V(q+G)\sum_{n,n'k}\langle n,k|e^{-i(q+G).r}|n',k+q\rangle\langle n',k+q|e^{i(q+G').r'}|n,k\rangle \times \frac{f(\varepsilon_{n',k+q})-f(\varepsilon_{n,k})}{\varepsilon_{n',k+q}-\varepsilon_{nk}}, \tag{2.4.28}$$

where a plane-wave basis set $\{\phi_{nk} = |nk\rangle\}$ is used.

2.4.4 GW self-energy content

The expression (2.4.3) for the GW self-energy allows the real part of Σ to be broken into two terms, each with a clear physical interpretation.[11] These are:

$$\Sigma_{SEX}(r,r',E) = -\int_{-\infty}^{\mu} dE' A(r,r',E') \mathrm{Re} W(r,r',E-E') \tag{2.4.29}$$

$$\Sigma_{COH}(r,r',E) = -\int_{-\infty}^{\infty} dE' A(r,r',E') P \int_{0}^{\infty} dE'' \frac{B(r,r',E'')}{E-E'-E''} \tag{2.4.30}$$

Here, A is the spectral function for the Green's function and B is related to the imaginary part of W by:

$$W(r,r',E) = V(r,r') + \int_{0}^{\infty} dE' \frac{2E' B(r,r',E')}{E^2 - (E'-i\eta)^2}, \tag{2.4.31}$$

where $\eta = 0^+$. Σ_{SEX} represents the screened exchange, and arises from the poles in the Green's function, while Σ_{COH} is the so-called Coulomb hole term, and arises from the poles in the imaginary part of W. Using the expression (2.4.16) for A, we obtain

$$\Sigma_{SEX}(r,r',E) = -\sum_{nk}^{occ} \phi_{nk}(r)\phi_{nk}^{*}(r') W(r,r',E-\varepsilon_{nk}) \tag{2.4.32}$$

$$\Sigma_{COH}(r,r',E) = \sum_{nk} \phi_{nk}(r)\phi_{nk}^{*}(r') P \int_{0}^{\infty} dE' \frac{B(r,r',E')}{E-\varepsilon_{nk}-E'} \tag{2.4.33}$$

In this form, the interpretation of Σ_{SEX} as the dynamically-screened exchange is clear. To understand the Coulomb hole term Σ_{COH}, it is helpful to consider the static limit of (2.4.33). In this case, it can be shown[11] that

$$\Sigma_{COH}(r,r') = \frac{1}{2}\delta(r-r')[W(r,r',E=0) - V(r,r')]. \tag{2.4.34}$$

In this form, it can be seen that Σ_{COH} is the interaction of the quasiparticle with the induced potential due to the rearrangement of the electrons around the quasiparticle. It is also worth noting that in this static limit (2.4.34), Σ_{COH} reduces to a local term.

In the plane wave basis, the matrix elements of Σ_{SEX} and Σ_{COH} as given in the GW approximation are:[11]

$$\langle nk|\Sigma_{SEX}(r,r',E)|n'k\rangle = -\sum_{n_1}^{occ}\sum_{qGG'}\langle nk|e^{-i(q+G).r}|n_1k+q\rangle\langle n_1k+q|e^{i(q+G').r'}|n'k\rangle \times\left[1+\frac{\Omega^2_{GG'}(q)}{(E-\varepsilon_{n_1k+q})^2-\tilde{\omega}^2_{GG'}(q)}\right]v(q+G') \tag{2.4.35}$$

$$\langle nk|\Sigma_{COH}(r,r',E)|n'k\rangle = \sum_{n_1}\sum_{qGG'}\langle nk|e^{-i(q+G).r}|n_1k+q\rangle\langle n_1k+q|e^{i(q+G').r'}|n'k\rangle \times\left[\frac{1}{2}\frac{\Omega^2_{GG'}(q)}{\tilde{\omega}_{GG'}(q)(E-\varepsilon_{n_1k+q}-\tilde{\omega}_{GG'}(q))}\right]v(q+G') \tag{2.4.36}$$

Evaluating $\Sigma = \Sigma_{SEX} + \Sigma_{COH}$ in principle requires a diagonalization of the the full matrix. In practice, it has been found that the resulting quasiparticle wavefunction is very close to the corresponding LDA wavefunction ϕ_{nk}, so that only the diagonal element $\langle nk|\Sigma|nk\rangle$ is required.[11] The quasiparticle energy E^{QP}_{nk} is then given by

$$E^{QP}_{nk} = \varepsilon^{LDA}_{nk} - \langle nk|V^{LDA}_{XC}|nk\rangle + \langle nk|\Sigma(E^{QP}_{nk})|nk\rangle. \tag{2.4.37}$$

To evaluate (2.4.37), the self-energy operator is expanded to first order in the energy around ε^{LDA}_{nk}. This gives:

$$E^{QP}_{nk} = E^{0}_{nk} + \frac{\Delta\Sigma_{nk}(\varepsilon_{nk})/\Delta E}{1-\Delta\Sigma_{nk}(\varepsilon_{nk})/\Delta E}(E^{0}_{nk}-\varepsilon_{nk}), \tag{2.4.38}$$

where

$$E^{0}_{nk} \equiv \varepsilon^{LDA}_{nk} - \langle nk|V^{LDA}_{XC}|nk\rangle + \langle nk|\Sigma(\varepsilon^{LDA}_{nk})|nk\rangle. \tag{2.4.38}$$

A second iteration has been found to be unnecessary in most cases.[11]

In practice, computing accurate quasiparticle energies within the GW framework above requires convergence with respect to the size of the static dielectric matrix ε (which enters through $\tilde{\omega}^2_{GG'}(q)$), as well as the number of unoccupied bands used in evaluating ε and the Coulomb-hole term. The size of ε is related to the importance of local field effects in screening, as these are captured by the off-diagonal elements of ε. These local field effects arise from the microscopic response of the inhomogeneous charge density to perturbations, and are more pronounced in ionic systems and insulators; in the extreme limit of a homogeneous free electron gas, ε is a scalar. The number of unoccupied bands required relates to the plasmon pole excitation energies in the system. Unoccupied bands are explicitly included in Σ_{COH} but not in Σ_{SEX}, because Σ_{COH} describes the self-energy contribution due to an electron interacting with excited electron-hole pairs around it, while Σ_{SEX} is the screened exchange. As the band index increases, so does the corresponding energy denominator in the terms in Σ_{COH} and ε, thus allowing convergence.

2.5 Wannier functions

In this section, we return to the density-functional Kohn-Sham framework. The Hohenberg-Kohn theorem states that the ground state energy of a system is completely determined by its charge density.[3] The spatial distribution of electronic charge can undoubtedly provide substantial information about the physics and chemistry of a system. However, quantifying charge transfer and charge assignments has been a long-standing difficulty in electronic structure calculations, because there is no obvious way to assign charge to any given atom or bond. The problem of charge assignment can be elegantly

treated using localized Wannier functions, as demonstrated in the application in Chapter 5.

Wannier functions[13] are Fourier transforms of Bloch functions, which are eigenfunctions of operators that are translationally invariant. Specifically, if $\boldsymbol{H}$ commutes with the translation operator $\boldsymbol{T_R}$, the eigenstates of $\boldsymbol{H}$ are Bloch functions

$$\psi_{nk}(\boldsymbol{r}) = e^{i\phi_n(k)} e^{-ik.r} u_{nk}(\boldsymbol{r}), \tag{2.5.1}$$

where $u_{nk}(\boldsymbol{r})$ has the periodicity of $\boldsymbol{H}$, and $\boldsymbol{k}$ is defined modulo any reciprocal lattice vector $\boldsymbol{G}$ ($e^{iG.R} = 1$). The phase $\phi_n(\boldsymbol{k})$ is arbitrary. The corresponding Wannier functions are given by

$$w_{nR}(\boldsymbol{r}) = \frac{V}{(2\pi)^3} \int_{BZ} dk \psi_{nk}(\boldsymbol{r}) e^{i\varphi_n(k)} e^{-ik.R}, \tag{2.5.2}$$

where V is the volume of the unit cell. $\varphi_n(\boldsymbol{k})$ has the periodicity of the Brillouin Zone (BZ), and is non-unique because $\phi_n(\boldsymbol{k})$ in (2.5.1) is arbitrary. The orthonormality of Bloch functions carries over to Wannier functions by construction. The formulation above is general: $\boldsymbol{H}$ can be any periodic operator; we shall focus on the case where $\boldsymbol{H}$ is the Kohn-Sham Hamiltonian, and $\psi_{nk}(\boldsymbol{r})$ are single-particle eigenstates.

For a group of N isolated bands (e.g. valence bands in an insulator), the definition of Wannier functions is generalized to

$$w_{nR}(\boldsymbol{r}) = \frac{V}{(2\pi)^3} \int_{BZ} dk \tilde{u}_{nk}(\boldsymbol{r}) e^{ik.(r-R)}, \tag{2.5.3}$$

where $\tilde{u}_{nk} = \sum_{m=1}^{N} U_{nm}^{(k)} u_{mk}$ for some unitary matrix $U^{(k)}$. Since $U^{(k)}$ is arbitrary and mixes Bloch states in different bands, Wannier functions can vary significantly in size and

shape. This severe non-uniqueness was, for a long time, regarded as an obstacle to practical applications of Wannier functions. The recent interest in the Wannier formalism stems from two key developments: (a) the identification of gauge-invariant properties of Wannier functions, such as the sums of all Wannier centers, $\langle w_{nR}|r|w_{mR}\rangle$, in a unit cell, which are relevant to dielectric properties,[2] and (b) the formulation of well-defined criteria for choosing $U^{(k)}$. It turns out that the gauge freedom can in fact be exploited to construct Wannier functions suited to the needs of specific problems. For example, $U^{(k)}$ can be chosen so that the Wannier functions are maximally localized, or maximally projected onto chosen real-space functions, which provide an elegant and intuitive formalism for many problems in condensed matter.

2.5.1 Wannier functions with desired symmetry properties

One of the most successful procedures for obtaining maximally localized wavefunctions (MLWFs) involves minimizing the spread of Wannier functions.[14, 15] Here, we focus instead on the approach recently developed by Bhattacharjee and Waghmare, which yields localized Wannier functions with desired symmetry properties without any variational procedures.[16, 17] The ability to incorporate desired symmetry properties makes the latter procedure well-suited to the analysis of bonding characteristics, as described in Chapter 5. Wannier functions obtained in this way can be proven to be maximally localized in 1D. In higher dimensions, these Wannier functions are typically not maximally localized, but they can be chosen to have particular symmetry properties, and can be transformed to MLWFs through a diagonalization procedure.

We shall focus first on the 1D case. It is possible to construct MLWFs in 1D without any variational calculation, by using the fact that parallel-transported Bloch

functions (PTBFs) in 1D are Fourier-transformed to give MLWFs. PTBFs $e^{ikx}u''_{nk}(x)$ obey the following property:

$$\left\langle u''_{mk} \left| \frac{\partial u''_{nk}}{\partial k} \right\rangle = 0. \right. \tag{2.5.4}$$

It is easy to understand the geometric meaning of (2.5.4) in the case of a single band where $m = n$. The vector $u''_{nk}(x)$ is transported along k in the BZ such that it is perpendicular to $\frac{\partial u''_{nk}}{\partial k}$, so that locally, $u''_{nk}(x)$ is parallel to $u''_{nk+b}(x)$ for small b. This amounts to eliminating random phases accompanying Bloch functions at different k in the BZ. Intuitively, PTBFs correspond to Bloch functions that are optimally smooth, and thus will Fourier transform to give Wannier functions that are maximally localized.

It is important to note that although random relative phases between neighboring k's are eliminated, the well-known Berry's geometric phase is immediately recovered once a closed loop is traversed. Berry's phase can be generalized in the case of multiple bands to yield a phase matrix Γ, defined by

$$\left[e^{i\Gamma}\right]_{mn} = \left\langle u''_{mk_0} \left| \exp\left(i\frac{2\pi x}{a} \right) \right| u''_{nk_0+2\pi/a} \right\rangle. \tag{2.5.5}$$

Non-diagonal elements of Γ are related to the mixing of different Bloch functions during parallel transport. Therefore, the problem of N composite bands (bands that cross) can be reduced to that of N simple bands (no band-crossing), simply by diagonalizing Γ to decouple the states.

MLWFs can thus be constructed in 1D as follows. First, PTBFs are obtained from calculated Bloch states by imposing the condition (2.5.4). This can be achieved using linear response within the gauge in (2.5.4), or through singular value

decomposition (SVD), as we describe below. Next, the geometric phase matrix Γ is computed for these PTBFs, and a unitary transformation is performed on the PTBFs so that the resulting Γ is diagonal. The resulting PTBFs $\tilde{u}_{nk}(x)$ are optimally smooth, but typically do not have the lattice periodicity in reciprocal space (because of non-trivial Berry's geometric phases in the diagonal elements γ_n of Γ). This can be fixed in the final step through a simple unitary transformation that gives smooth and periodic BFs $v_{nk}(x)$, given by

$$v_{nk}(x) = \exp\left[-ik\frac{\gamma_n a}{2\pi}\right]\tilde{u}_{nk}(x). \tag{2.5.6}$$

Wannier functions obtained by a Fourier transformation of $v_{nk}(x)$ are orthonormal.

Generalizing the above approach to higher dimensions (D > 1) is non-trivial because the geometric phase matrices Γ_α, generated for paths along different directions k_α, typically do not commute, corresponding to non-trivial phases for closed paths within the BZ. To circumvent this problem, an auxiliary subspace S_a is introduced, so that Bloch functions at a given k-point k_0 in the physical subspace S_p can be parallel-transported to another k-point k_1 in S_p through a path that connects k_0 to the corresponding point k_0 in S_a, continues to k_1 in S_a, and back to k_1 in S_p. The important difference between S_a and S_p is that we can construct, by Fourier transforming highly localized orthonormal real-space orbitals $\Psi_{\mu R}(r)$, smooth and periodic, non-degenerate Bloch functions $v_{\mu k}$ in S_a, that satisfy the parallel-transport criterion (2.5.4). In contrast to the complicated Bloch manifold S_p, where closed paths can have non-trivial geometric phases (e.g. due to degeneracy of Bloch states within the surface enclosed by the closed path), closed paths

in S_a have zero geometric phases by construction. Therefore, the geometric phase between two points in S_a is well-defined and independent of the path taken between them.

It now remains to understand the notion of parallel transport along constant k paths between S_a and S_p. It turns out that this is equivalent to making the overlap matrix between $\boldsymbol{u}_{nk}$ in S_p and $\boldsymbol{v}_{\mu k}$ in S_a,

$$\boldsymbol{S}^k_{\mu n} = \left\langle \boldsymbol{v}_{\mu k} \middle| \boldsymbol{u}_{nk} \right\rangle, \tag{2.5.7}$$

Hermitian, by a suitable unitary transformation $\boldsymbol{M}_k$ on $\boldsymbol{u}_{nk}$. A useful consequence of this condition is that the resulting Bloch functions,

$$\tilde{\boldsymbol{u}}_{\mu k} = \sum_j \boldsymbol{M}_{\mu j} \left| \boldsymbol{u}_{jk} \right\rangle, \tag{2.5.8}$$

are Fourier transformed to give Wannier functions $\Phi_{\mu R}(\boldsymbol{r})$ that are maximally aligned with the localized functions $\Psi_{\mu R}(\boldsymbol{r})$ originally constructed in S_a. Thus, one obtains maximally projected Wannier functions that can potentially provide much insight into the physics and chemistry of the system.

The proposed construction of Wannier functions thus proceeds as follows. First, we develop an auxiliary subspace of highly localized, orthnormal orbitals $\Psi_{\mu R}(\boldsymbol{r})$ with desired symmetry properties. The overlap matrix $\boldsymbol{S}^k$, as defined above, can be written as

$$\boldsymbol{S}^k = \boldsymbol{R}_k e^{i\Gamma_k}, \tag{2.5.9}$$

where $\boldsymbol{R}_k$ is a positive definite Hermitian matrix, and Γ_k the geometric phase matrix. Parallel transport is achieved when $\Gamma_k = \boldsymbol{0}$. Determination of $\boldsymbol{R}_k$ and Γ_k is achieved by singular value decomposition (SVD) of $\boldsymbol{S}^k$:

$$\boldsymbol{S}^k = \boldsymbol{U}_k \Sigma_k \boldsymbol{V}_k^\dagger, \tag{2.5.10}$$

where Σ_k is a diagonal matrix with non-negative singular values in its diagonal. Importantly, this scheme is self-corrective in the sense that a vanishing singular value suggests that the choice of symmetries in $\Psi_{\mu R}(\boldsymbol{r})$ is not optimal, and hints for correction. It can be shown that the desired transformation $\boldsymbol{M}_k$ in (2.5.8) is $\boldsymbol{M}_k = (\boldsymbol{U}_k \boldsymbol{V}_k^{\dagger})^*$.

Metallic systems can be treated by including occupation numbers f_{nk} in (2.5.8):

$$\tilde{\boldsymbol{u}}_{\mu k} = \sum_j \boldsymbol{M}_{\mu j} \left| \boldsymbol{u}_{jk} \right\rangle \boldsymbol{f}_{nk}^{1/2}. \tag{2.5.11}$$

It should be noted that (2.5.11) in fact results in Wannier orbitals that are no longer orthonormal. Inclusion of occupation numbers is, however, a key concept required for the bonding analysis in Chapter 5. The occupation numbers essentially weight the contribution of each Bloch state to the resulting Wannier orbital. Thus, the amount of charge in each orbital is physically meaningful (without the occupation numbers, each orbital would carry unit charge). For the application in Chapter 5, it was found that the resulting orbitals are still roughly orthogonal, and the amount of charge in each orbital was used for assigning formal oxidation states and relative bond strengths. Wannier functions obtained as described above are found to exhibit exponential decay in insulators, and power law decay in metals.

References

[1] E. Kaxiras, *Atomic and Electronic Structure of Solids* (Cambridge University Press, Cambridge, United Kingdom, 2003).

[2] R. M. Martin, *Electronic Structure: Basic Theory and Practical Methods* (Cambridge University Press, Cambridge, United Kingdom, 2004).

[3] P. Hohenberg and W. Kohn, Phys. Rev. B **136**, B864 (1964).

[4] W. Kohn and L. J. Sham, Phys. Rev. **140**, 1133 (1965).

[5] M. Gajdos, A. Eichler, and J. Hafner, J. Phys.-Condes. Matter **16**, 1141 (2004).

[6] J. P. Perdew, J. A. Chevary, S. H. Vosko, K. A. Jackson, M. R. Pederson, D. J. Singh, and C. Fiolhais, Phys. Rev. B **46**, 6671 (1992).

[7] L. Hedin and S. Lundqvist, Solid State Physics **23**, 1 (1969).

[8] M. S. Hybertsen and S. G. Louie, Phys. Rev. Lett. **55**, 1418 (1985).

[9] M. S. Hybertsen and S. G. Louie, Phys. Rev. B **34**, 5390 (1986).

[10] S. G. Louie and A. Rubio, in *Handbook of Materials Modeling, Volume I: Methods and Models*, edited by S. Yip (Springer, Netherlands, 2005), p. 1.

[11] M. S. Hybertsen, in *Exchange and Correlation in Semiconductors and Insulators (Ph.D. Thesis)* (University of California, Berkeley, Berkeley, 1986).

[12] N. W. Ashcroft and N. D. Mermin, *Solid State Physics* (Saunders College Publishing, New York, 1976).

[13] G. H. Wannier, Phys. Rev. **52**, 0191 (1937).

[14] N. Marzari and D. Vanderbilt, Phys. Rev. B **56**, 12847 (1997).

[15] I. Souza, N. Marzari, and D. Vanderbilt, Phys. Rev. B **65**, 035109 (2002).

[16] J. Bhattacharjee and U. V. Waghmare, Phys. Rev. B **73**, 121102 (2006).

[17] J. Bhattacharjee and U. V. Waghmare, Phys. Rev. B **71**, 045106 (2005).

Chapter 3

MoO_3 monolayers on Au(111)

3.1 Tuning electronic properties of novel metal oxide nanocrystals using interface interactions: MoO_3 monolayers on Au(111)

We report experimental and theoretical investigations of monolayer MoO_3 nanocrystals grown on Au(111), in contrast to the bilayered structure of the bulk oxide crystal. The Au surface acts as the other half of the bilayer by satisfying local bonding requirements through charge redistribution at the interface. Epitaxy with the Au lattice is achieved through the ability of the Mo-O bonds to rotate about one another. The oxide layer becomes semimetallic as it strains to enhance bonding with the Au substrate. This flexibility of the oxide lattice suggests the possibility of tuning electronic properties of transition metal oxides *via* interface interactions. The effects of electronic structure on the surface chemistry of oxides are in turn illustrated by H adsorption energetics on MoO_3.

This work has been published as a letter in Surface Science:

S. Y. Quek, M. M. Biener, J. Biener, C. M. Friend and E. Kaxiras, Surface Science **577**, L71-L77 (2005).

3.1.1 Introduction

Metal oxide nanocrystals on metal surfaces have novel electronic properties due to interface[1, 2] and nanoscale[3] effects. The ability to grow such structures in a controllable fashion can open exciting possibilities for practical applications. A case in point is molybdenum oxides, the properties of which depend sensitively on their atomic structure and composition. For example, their catalytic activity is determined by the type of

oxygen species exposed,[4] while some oxides exhibit charge density wave instabilities due to the quasi one- and two-dimensional arrangements of oxide octahedra in these systems.[5]

MoO_3 nanocrystals were grown on Au(111) surfaces by both chemical (CVD) and physical vapor deposition (PVD) of Mo, followed by oxidation using NO_2. In the CVD experiments, the surface was typically exposed to 1 L of $Mo(CO)_6$ and 10 L of NO_2 alternatively at 450 K, followed by annealing to 600 K for 1 min after every four cycles of dosing, for a total of 16 cycles. The PVD syntheses were performed at 450-600 K. Typically, 0.3 ML of Mo was deposited at a flux of ~ 0.25-0.75 ML/min, and oxidized by exposure to 20 L of NO_2. Further experimental details are described elsewhere.[6, 7]

High resolution scanning tunneling microscopy (STM) and low energy electron diffraction studies indicate that the MoO_3 islands grown by either technique have a $c(4 \times 2)$ unit cell. While bulk MoO_3 consists of weakly-interacting bilayers,[8] STM images reveal that the islands are one monolayer in height, i.e. half of the bilayer found in bulk MoO_3 (Fig. 1(b)). This interesting surface structure has another important ramification: although clean Au(111) has a herringbone reconstruction,[9] STM images indicate that the reconstruction is not continued under the islands (Fig. 1(a)), a feature we adopt in the theoretical model of the system.

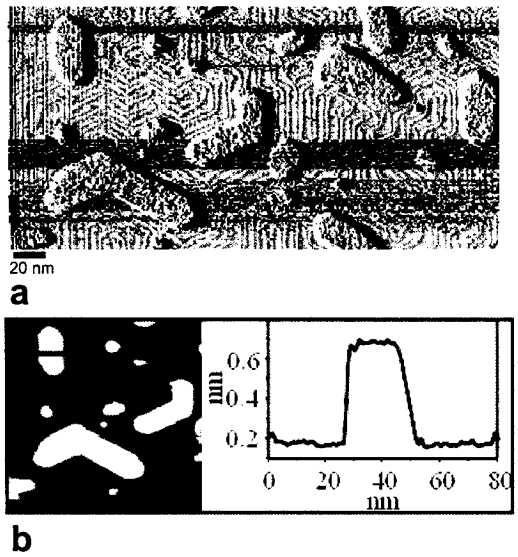

FIG. 1. STM images of MoO_3 islands on Au(111). The sample was prepared by PVD of 0.3 ML of Mo on Au(111) at 600 K, and subsequent oxidation by exposure to 20 L of NO_2 at 600 K. The images were collected at room temperature at a sample bias of +2.0 V and a tunneling current of 0.15 nA. (a) Constant height image. The Au herringbone reconstruction runs parallel to the straight island edges, and bends sharply at rough island edges. These bends indicate that the Au(111) reconstruction is lifted under the MoO_3 islands. (b) Corresponding constant current image of a portion of (a). The line scan on the right is taken along the blue line. It shows that the MoO_3 island has an apparent height of 0.5 nm, in contrast to the height of a bulk bilayer cell which is 1.39 nm,[8] thus suggesting that the island consists of a MoO_3 monolayer.

3.1.2 Computational details

The atomic and electronic structure of this system were studied using density functional theory, with the projected augmented wave method[10, 11] and Perdew-Wang 91 gradient correction,[12] as implemented in VASP.[13] We use a slab model with 6 Au layers in a $c(4 \times 2)$ supercell, separated by 16.5 Å of vacuum before the oxide is introduced. The

MoO_3 monolayer and the top 3 Au layers were relaxed until forces were less than 0.01 eV/Å. Geometry optimizations were performed using a plane-wave cutoff of 400 eV and a 3×3 *k*-point mesh. A 6×6 mesh did not change the optimized geometry significantly. Energies and charge densities were calculated using a plane-wave cutoff of 500 eV and a 12×12 *k*-point mesh. Such a mesh gave converged total energies in a bulk-terminated Au(111) surface.

3.1.3 Results and discussion

Our calculations reveal that the MoO_3 monolayer (Fig. 2(a)) distorts to fit the Au lattice and has distinct symmetry properties from its bulk analogue (Fig. 2(d)), which served as the guide for our initial oxide structure. In contrast to the bulk case, the MoO_3 monolayer has two non-equivalent planes of reflection and glide symmetry. The slab appears to be composed of MoO_3 units tilting alternately forwards and backwards relative to the surface normal, along the axes of reflection (Fig. 2(b)). Using the notation in Fig. 2, O_{b2} is situated directly above a Au atom, while O_{b1} is above a Au bridge site. Mo sits in a 3-fold site, off-centered away from the Au atoms below O_{b2}.

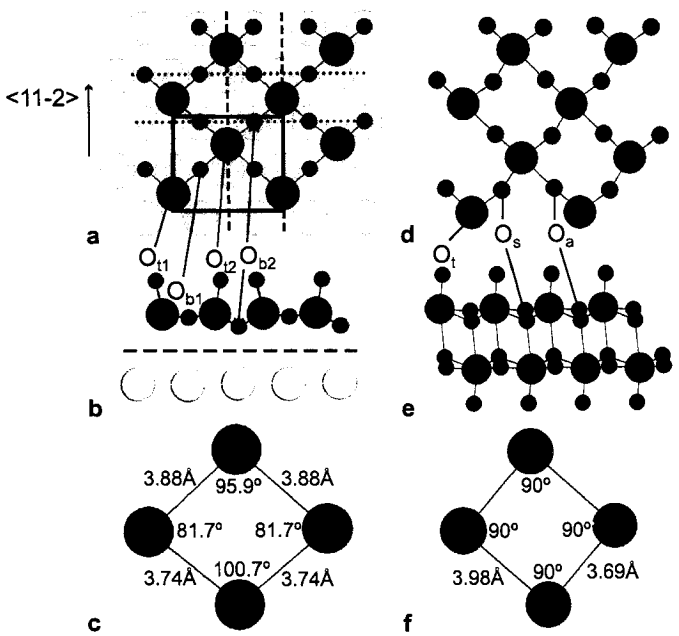

FIG. 2. Atomic structure of MoO_3 slabs. (a) Top view of MoO_3 monolayer on Au. (b) Side view of MoO_3 monolayer on Au. (c) Top view of Mo sublattice in MoO_3 monolayer on Au. (d) Top view showing half a bulk MoO_3 bilayer. (e) Side view of a bulk MoO_3 bilayer. (f) Top view of Mo sublattice in half a bulk MoO_3 bilayer. Blue, red and green circles represent Mo, O and Au atoms respectively. MoO_3 units are close-packed along the diagonal of the $c(4 \times 2)$ unit cell, indicated by the black box. Dashed and dotted lines in (a) respectively denote planes of reflection and glide symmetry in the oxide monolayer. The view in (b) is that down the glide planes, and shows MoO_3 units tilting backwards and forwards along the axes of reflection. O_{b1} and O_{b2} denote the two inequivalent bridging O atoms in the unit cell of MoO_3 on Au, with O_{b2} nearer to the Au surface than O_{b1}. The terminal O atoms in the MoO_3 monolayer on Au are labeled O_{t1} and O_{t2}. The dashed line in (b) denotes the plane relevant for the plot in Fig. 5. In bulk MoO_3, there are 3 distinct oxygen species, labeled O_t (terminal), O_s (symmetric bridging) and O_a

(asymmetric bridging). Calculated bond lengths in the bulk are within 1-3 % of experiment (Table 1).

Oxygen type	Number of Mo neighbors	Calculated Mo-O bond lengths in Å (experimental values in brackets)
Bulk MoO_3		
O_t	1	1.70 (1.67)
O_s	3	1.97 (1.95), 1.97 (1.95), 2.40 (2.33)
O_a	2	1.77 (1.73), 2.22 (2.25)
MoO_3 monolayer on Au		
O_{t1}	1	1.69
O_{t2}	1	1.69
O_{b1}	2	1.95, 1.95
O_{b2}	2	1.98, 1.98

TABLE 1. Bond lengths in bulk MoO_3 and in the MoO_3 monolayer on Au.

We performed simulations of the STM images expected for this system based on the Tersoff-Hamann theory.[14] The bright spots in the STM images are found to correspond to lateral positions of terminal O. Within the limits of experimental variance, the relative positions of these spots are the same in theory and experiment (Fig. 3), thus lending strong evidence to the predicted tilting of MoO_3 units.

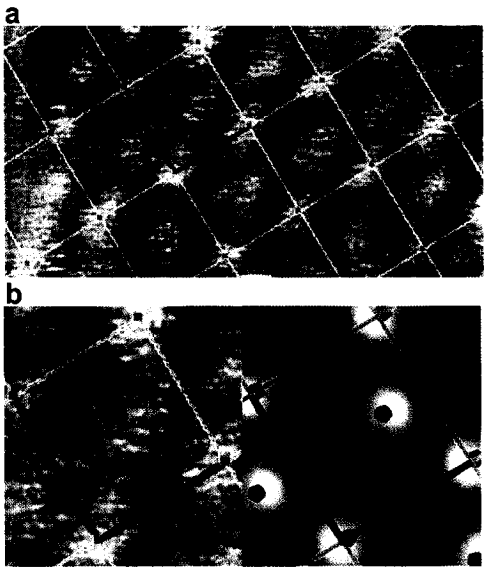

FIG. 3. STM images of the interior of the MoO_3 islands. (a) Experimental STM image, collected at room temperature. (b) Left: Close-up section of experimental STM image in (a). Right: STM simulation corresponding to a tip-sample separation of 1.4 Å. The bias voltages were –0.580 V in both the experiment and the simulation. The tunneling current in the experiment was 25.4 pA. A brighter color represents a more intense current. The green lines show the $c(4 \times 2)$ unit cells, which are 5.76 Å × 4.99 Å. The bright spots in the experimental images are related to lateral positions of terminal O atoms on the surface, which are marked by black pentagons in the simulation. In each cell, there is a bright spot slightly off-center. In polar coordinates with respect to the (x, y) axes (denoted as blue and red in the figure), the off-center spot is at $r = 4.3$ Å, $\theta = 42$ ° in the simulation, and $r = 4.1 \pm 0.4$ Å, $\theta = 43 \pm 4$ ° in the experiment.

Phonon frequencies of the MoO_3 monolayer were computed at the Brillouin zone center, using the harmonic approximation. We found only 6 Electron Energy Loss Spectroscopt (EELS)-active[15] phonon modes out of 24 possible ones. The calculated

frequencies, with corresponding experimental values in parentheses, are, in cm^{-1}: 1030, 1020 (990), 804 (850), 430 (480), 351 (280) and 160 (not observed). Noting that instrument resolution is about 80 cm^{-1}, and that 160 cm^{-1} is out of the detection range, theoretical and experimental frequencies correspond fairly well, providing further evidence for the predicted symmetry properties. The slight mismatch between calculated and experimental frequencies may be related to the fact that finite-size effects are neglected in the simulation. Bonds in finite-sized islands may be slightly stronger than in an infinite oxide layer, especially for atoms close to or at the island edges. We therefore expect the frequencies to be blue-shifted for a finite system. This may account for the higher experimental frequencies at 850 and 450 cm^{-1} (the % discrepancy for the mode corresponding to 990 cm^{-1} is small (3.5 %) while the soft mode at 280 cm^{-1} corresponds to small energy differences in the finite-difference approach employed in the calculation, and is therefore difficult to calculate accurately).

The preceding results confirm unequivocally that the optimized structure matches the experimental structure of the interior of the MoO_3 monolayer islands on Au(111), without including defects. It is remarkable that the Mo sublattice from the bulk monolayer distorts by as much as 11° to fit the Au lattice (Fig. 2(c)). Geometrical considerations indicate that the $c(4 \times 2)$ unit cell is in fact the smallest unit cell for which epitaxy can be achieved, if sufficient bonding between Mo atoms through the bridging O bonds is to be preserved. The symmetry properties of the monolayer are also dictated by the symmetries of the Au substrate – the reflection symmetry in the oxide is matched by a reflection symmetry in the Au lattice, and the glide plane symmetry in the oxide corresponds to a similar symmetry in the top Au layer, if its relation to underlying Au

layers is ignored. This flexibility of the oxide lattice is achieved by the ability of the Mo-O bonds to rotate about one another: the dihedral angles involving terminal oxygens in the bulk monolayer take the values 0° and 37°(angle O_t-Mo-O_s-Mo in Fig. 2(d)), whereas the corresponding dihedral angles in the relaxed MoO_3 monolayer on Au take values of 7-8°.

Unlike bulk MoO_3 which has a bilayer structure and is semiconducting, the MoO_3 monolayer on the Au surface is semimetallic, as deduced from the density of states (DOS) of the MoO_3/Au system, projected onto the oxide slab (Fig. 4(a)). The MoO_3 monolayer alone has a similar, semimetallic DOS. However, if this monolayer is allowed to relax in the same supercell without the Au substrate, rows of Mo atoms relax alternately towards rows of O_{b1} and O_{b2}, breaking the glide-plane symmetry and the monolayer becomes semiconducting. Analysis of the DOS of the semimetallic MoO_3 monolayer reveals that Fermi level states are localized in the plane of Mo and bridging O (Fig. 4(b)). These symmetry-degenerate states are split by a Jahn-Teller distortion which leads to a semimetal-to-insulator transition with Mo relaxing towards a pair of bridging O atoms to form stronger bonds.

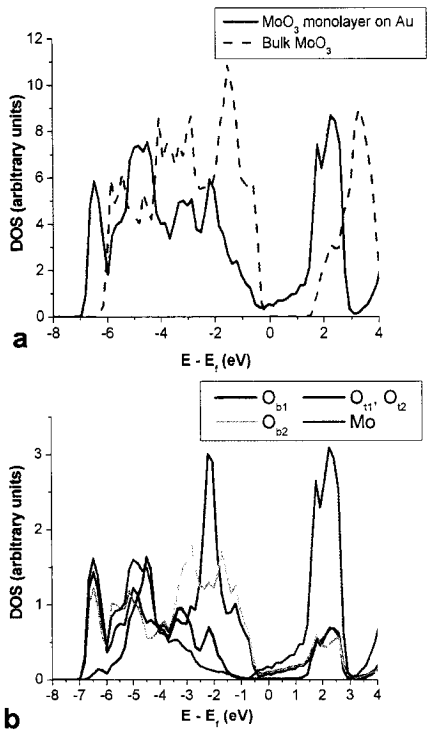

FIG. 4. Projected density of states (DOS) for (a) the MoO_3 monolayer on Au and (b) Mo and the distinct O species in the MoO_3 monolayer on Au. The DOS for bulk MoO_3 is given in the dashed blue line in (a). Unlike bulk MoO_3, the MoO_3 monolayer on Au is semimetallic, with Fermi level states localized in the plane of Mo and bridging O.

We expect this oxide monolayer to exhibit interesting surface chemistry because of the relative ease of promoting electrons across the Fermi level in a semimetal. Indeed, H is found to adsorb more strongly than on bulk MoO_3: the binding energies for H at saturation coverage are, in eV, –3.39, –2.77 and –3.13 on O_t, O_s and O_a respectively in bulk MoO_3,[16] and –3.55, –3.95 and –3.94 on the terminal O, O_{b1} and O_{b2} respectively in the MoO_3 monolayer on Au. In contrast to bulk MoO_3, the bridging oxygens are more stable binding sites for H than the terminal oxygens. This is consistent with the

localization of Fermi level states along the plane of bridging O. The adsorption of H on bridging O also provides greater strain relief by breaking up the strained lattice.

The above analysis suggests that the semimetallic character of the MoO_3 monolayer on Au can be attributed to the strained Mo-O bridging bonds. The difference in energy between the relaxed and strained MoO_3 monolayers was 0.15 eV/supercell. The cohesive energy for the MoO_3/Au system, with respect to a relaxed unreconstructed Au(111) surface and the strained MoO_3 monolayer, was –0.24 eV/supercell. The energy cost of straining the MoO_3 monolayer is therefore overcome by the increase in magnitude of the cohesive energy upon formation of the MoO_3/Au interface. To elucidate the nature of the MoO_3/Au interaction, we plot the difference between the charge density of the MoO_3/Au system, and the sum of charge densities of isolated MoO_3 and Au slabs, frozen in configuration from the joint system (Fig. 5).

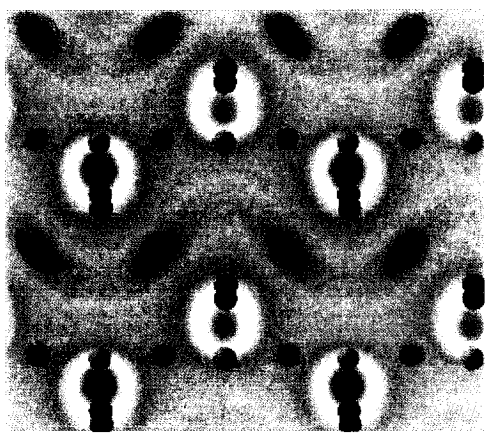

FIG. 5. Charge density difference between the MoO_3/Au system and the sum of charge densities of isolated MoO_3 and Au slabs, frozen in configuration from the joint system. The values are those on a plane mid-way between MoO_3 and Au, as indicated by the dashed line in Fig. 2(b). Blue, red and green spheres denote the lateral positions of Mo, O and Au atoms respectively. Half the Au atoms are hidden directly

under O_{b2}. Blue regions, corresponding to charge depletion, occur below O_{b2}, and red regions, corresponding to charge accumulation, are seen between Mo and the nearest Au atoms. Values of the charge density difference range from –0.0093 $e/Å^3$ to 0.0133 $e/Å^3$.

This reveals that the MoO_3 monolayer induces an electronic charge redistribution above the Au surface. The positively-charged Mo ions draw electron density to the region directly underneath them. Each of these electron clouds is in turn attracted by the nearest Au atom, since Au surface atoms are electron-deficient. In this way, Mo is drawn closer to the Au atom nearest to it. At the same time, the partial negative charges on O_{b2} cause them to be attracted to Au atoms directly beneath them. These interactions together cause the Mo-O_{b2} bridging bonds to strain resulting in semimetallic character. The electronic charge redistribution satisfies local bonding requirements, which allow the Au surface to act as the other half of the MoO_3 bilayer, thereby stabilizing the monolayer nanocrystals. Each Au surface atom is in turn bonded either to an O atom (O_{b2}) or a Mo atom, and as a result, the surface reconstruction under the MoO_3 islands is lifted.

3.1.4 Concluding remarks

In-situ STM studies suggest that the MoO_3 islands grow *via* aggregation of MoO_3 molecular species. Earlier theoretical work has shown that induced electrostatic interactions increase the cationic character of Mo as MoO_3 units build up to form bulk MoO_3.[17] Similarly, in our calculations, the local charge on Mo is larger in the MoO_3 slab on Au than in a single MoO_3 molecule. The increased ionic character upon aggregation of MoO_3 molecular species allows the oxide to polarize the electron gas at the MoO_3/Au interface. Charge redistribution at the interface allows the Au surface to serve as the other

half of the MoO_3 bilayer, thus stabilizing the monolayer structures, allowing nucleation and growth. The surface of these islands corresponds to the natural cleavage plane of bulk MoO_3 and has a free energy of only 0.05-0.07 J/m^2.[18] In contrast, Au has a surface free energy of 1.62 J/m^2.[19] Growth of the MoO_3 monolayer is thus driven by both an increase in magnitude of the cohesive energy and a reduction in surface free energy.

Interestingly, the long straight edges of the ensuing islands (Fig. 1) run along the ⟨11-2⟩ directions of Au, parallel to the herringbone pattern, and not the ⟨-312⟩ directions, diagonal to the $c(4 \times 2)$ unit cell, along which MoO_3 units are close-packed (Fig. 2(a)). The herringbone pattern is aligned parallel to straight island edges, but tends to form sharp bends at rough island edges. The herringbone pattern has the property of soliton-waves,[20] therefore, absence of Au reconstruction beneath the islands imposes hard-wall boundary conditions on these waves, causing the herringbone pattern to become locally parallel to the island edges. The distinct correlation between straight island edges and the herringbone direction points toward an interplay between the herringbone structure and the MoO_3 islands that affects the overall pattern developed on the surface. Further theoretical and experimental investigation of kinetic effects will substantially clarify the picture.

In this work, we have demonstrated that while MoO_3 exists as bilayers in the bulk crystal, MoO_3 monolayer nanocrystals can be grown on the Au(111) surface. These structures are also distinctly different from previously reported ramified MoO_3 islands grown on Au(111).[21] The observed flexibility of dihedral bond angles is likely to be common to many transition metal oxides, especially those with more than one structural phase in the bulk. In fact, it is likely that the growth mechanism proposed herein is

general enough so that novel structures of such oxides can be grown on metal surfaces by condensing molecular species, which become increasingly ionic, interacting with the substrate to create a wetting oxide layer. Thin films of some of these oxides have been grown on metal surfaces.[22, 23] For example, novel V_xO_y structures were recently grown on Pd(111) and understood by first principles energetic arguments.[23] Our analysis goes beyond previous studies by showing explicitly how the metallic substrate can induce strain in an oxide monolayer, resulting in changes in the electronic properties of the oxide thereby leading to interesting surface chemistry. These results suggest that the metallic substrate may be used as a handle to tune the electronic properties of interface-mediated oxide structures. The ability to grow crystalline oxide structures epitaxially on metal surfaces thus provides a first step towards synthesizing oxide systems with controllable properties.

3.2 Shear plane model for selectively reduced monolayer MoO_3 on Au(111)

Ordered two-dimensional (2D) MoO_3 monolayer nanostructures were prepared on Au(111) and annealed to 650 K. This resulted in selective reduction of Mo^{6+} to Mo^{5+} in the nanostructures. Prolonged annealing resulted in a final structure containing Mo^{6+} and Mo^{5+}, in the ratio of 1:1. In no case was there any detectable Mo^{4+} using X-ray photoelectron spectroscopy. Furthermore, no Mo^{4+} is detected upon annealing to higher temperatures, which results in a greater % of Mo^{5+} and the loss of Mo species. In this section, we present a possible theoretical model for the reduced oxide structure. The model is a generalization of 1D shear plane defects observed during reduction of bulk, bi-layered, MoO_3.

Material in this section will appear as part of an experimental paper to be published. The experimental work reported here was performed by X. Deng, M.M. Biener, J. Biener, R. Schalek, supervised by C.M. Friend.

3.2.1 Introduction

Metal oxides play an important role in several areas; one notable application is in heterogeneous catalysis.[24] For example, supported MoO_3 is known to promote the partial oxidation of methane to formaldehyde and is widely used as a catalyst in the petroleum and chemical industry.[25, 26] The properties of metal oxides depend sensitively on the presence and nature of defects. In the case of molybdenum oxides, the presence of vacancies plays an important role in enhancing chemical reactivity.[27, 28] The ability to control the quantity and type of defects present in the oxides is therefore important, both for fundamental studies and for applications.

In recent years, novel metal oxide nanocrystals have been grown on metal surfaces, as discussed in Section 3.1. This development adds another dimension of interest because these nanocrystals have structures that are distinct from the bulk, and can have interesting electronic properties arising from interface[1, 2] and nanoscale[3] effects. The ability to grow such structures in a controllable fashion thus suggests exciting possibilities for practical applications.

In this work, we demonstrate that it is possible to achieve selective reduction of ordered MoO_3 monolayer nanocrystals on Au(111) described in Section 3.1. The well-defined and novel structure of these nanocrystals provides an interesting starting point for the synthesis of reduced molybdenum oxide nanocrystals. Mo has three stable oxidation states: Mo^{6+}, Mo^{5+} and Mo^{4+}. Surprisingly, however, selective reduction of Mo^{6+} to Mo^{5+} was observed, even after prolonged annealing. The % of Mo^{5+} present increased with increasing annealing time, up to a maximum of 50% at 650 K. This provides a way to tailor the growth of reduced molybdenum oxide nanostructures with controllable oxidation states.

3.2.2 Experimental background

The MoO_3 nanostructures on Au(111), prepared as described in Section 3.1, are reduced by annealing to 650 K, as revealed by X-ray photoelectron spectra (XPS). Specifically, annealing the MoO_3 nanostructures to 650 K for 20 minutes results in a broadening of Mo 3d peaks, which can be fitted by 70% Mo^{6+} and 30% Mo^{5+} with binding energies of 232.5 and 231.4 eV for Mo $3d_{5/2}$, respectively. The fraction of Mo^{5+} increases upon heating at 650 K for longer time increments. 40 minutes annealing at 650 K yields 40% Mo^{5+}. Ultimately, a 1:1 mixture of Mo^{5+}:Mo^{6+} was observed after

annealing at 650 K for 1 hour. No further changes in the Mo^{5+}:Mo^{6+} ratio were observed upon heating for longer times, up to 120 minutes. No other oxidation states were detected after heating to 650 K in any of our experiments. Specifically, no Mo^{4+} is present based on the absence of intensity in the Mo $3d_{5/2}$ region at 229.1 eV.

Annealing also results in changes in the EELS vibrational spectrum. Before annealing, the most intense peak is found at 850 cm^{-1} with a shoulder at 990 cm^{-1}. In addition, two peaks with lower vibrational frequency are also present at 480 and 280 cm^{-1}. Based on DFT calculations on the MoO_3 structure, the peaks at 990 and 850 cm^{-1} can be assigned to stretches of the terminal O and bridging O bonds respectively, while the other modes involve the bending of bridging O bonds, and to a lesser extent, terminal O bonds. Annealing the MoO_3 nanostructures to 650K results in a decrease of the peak intensities. The peak intensity of the 850 cm^{-1} bridging O stretch deceases to about 80% after 20 minutes of annealing, and to about 20% after 60 minutes. The lower frequency peaks also decrease. Meanwhile, the terminal oxygen stretch peak resolves upon annealing. Although a decrease in peak intensity is also observed for the terminal O stretch, the ratio of peak intensities for the bridging and terminal O stretches changes from 4:1 to 2:1, indicating a structural change.

3.2.3 Shear plane defects

We propose that reduction of the MoO_3 monolayer structures results in the formation of shear defects (line defects along which oxygen vacancies accumulate). Preliminary STM images show that the oxide remains two-dimensional (2D) following thermal reduction, and line defects appear (Fig. 6).

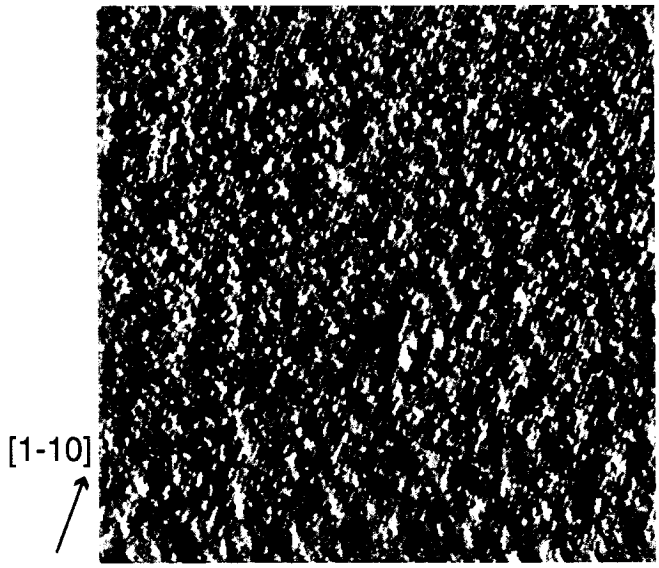

FIG. 6. STM image showing line defects following thermal reduction. The [1-10] direction of Au is indicated.

Similar shear structures are found in bulk MoO_3, resulting in the so-called Magneli phases, Mo_nO_{3n-1}.[29] In each phase of bulk Mo_nO_{3n-1}, the shear structures are regularly spaced and occur as planes. At the shear planes, MoO_6 octahedra share edges, instead of corners as in bulk MoO_3. It has been suggested that the shear planes form due to a dislocation mechanism, in which isolated oxygen vacancies stabilize by migrating towards one another, to form shear planes of edge-sharing octahedra. The shear planes can then expand by trapping more vacancies.[29] The regular spacing of these planes is likely to arise from mutual elastic repulsion. Similarly, it is possible that isolated bridging oxygen vacancies in the 2D MoO_3 monolayer can stabilize by agglomerating, with MoO_4 tetrahedra sharing edges instead of corners along a one-dimensional (1D) shear defect, as shown by the schematic in Fig. 7b.

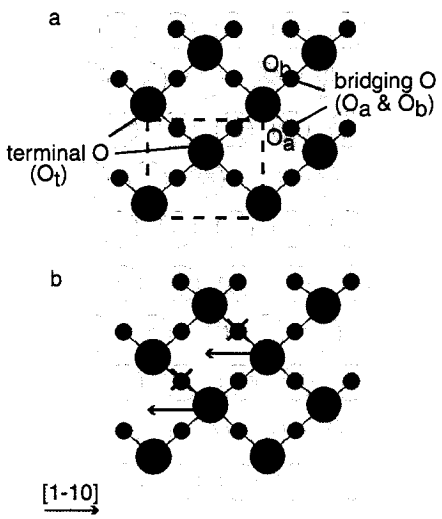

FIG. 7. (a) Atomic structure of MoO_3 monolayer on Au(111). (b) Schematic showing the formation of shear defects. The dotted black box in (a) denotes the *c*(4×2) unit cell. The structure is repeated periodically in the plane. Only the top Au layer is shown (out of a total of 6 layers, the bottom 3 of which are fixed in their bulk positions), as indicated by the hexagonal lattice of green circles. The [1-10] direction of Au is indicated. Mo and O are represented respectively by large blue and small red circles. Terminal (O_t) and bridging O's (O_a and O_b) are labeled in (a). The subscripts for O_a and O_b indicate if the bridging O is on an atop or bridging site of the Au(111) surface. The schematic in (b) shows how the oxide structure can 'shear' in the direction of the arrow, to accommodate the loss of a row of bridging O's as marked by black crosses.

3.2.4 Theoretical model

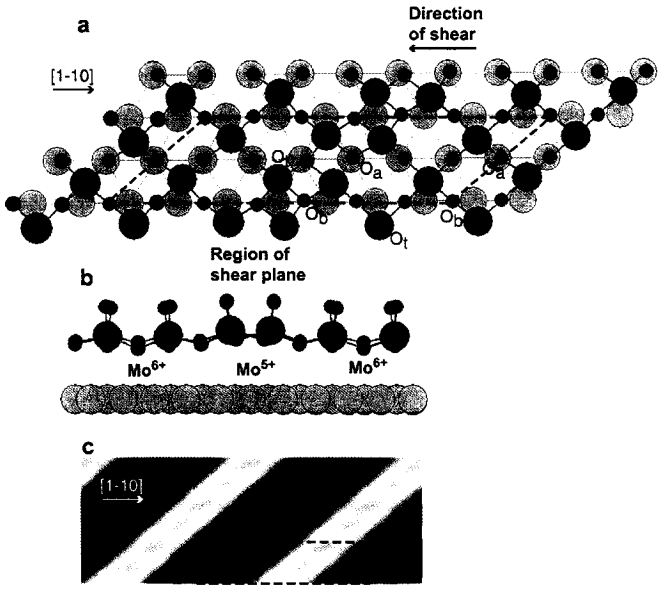

FIG. 8. Relaxed shear defect structure from (a) the top view and (b) the side view. (c) STM simulation. The unit cell used in this model is indicated by a dashed black box in (a) and a dashed black box in (c). The STM simulation corresponds to a sample bias of 1.5 V, with Gaussian smearing (standard deviation of 1.2 Å) to take into account tip convolution effects. The bright area in (c) corresponds to the shear plane defect. Mo atoms in the defect are raised by ~ 0.3 Å relative to Mo's away from the defect, which are in turn ~ 3.7 Å above the top Au layer (6 % more than corresponding height in the perfect oxide).

Fig. 8(a-b) shows a relaxed shear defect structure in which 1 bridging O is lost for every 4 Mo. The defect is characterized by more closely-spaced Mo rows connected by 3-fold coordinated O (3-fold coordinated O is also present in bulk MoO_3). The bond lengths of Mo-O_a and Mo-O_b in the defect structure are, respectively, in the range (-5.1, +5.1)% and (-4.6, +6.2)% of their corresponding values in the fully oxidized oxide, while

those for Mo-O_t remain unchanged. The longest Mo-O bonds (2.08 Å) are those joining Mo^{5+} to a 3-fold coordinated O atom across the defect line. The formal oxidation state of Mo is +6 and +5 between and along the shear defects respectively, and no Mo^{4+} is present. This is consistent with XPS data. The loss of bridging O in the shear structure is also consistent with EELS results, which indicate a sharper drop in the intensity for the bridging O stretch compared to that for the terminal O stretch. Finally, preliminary STM data also indicates that reduced structures are 2D, with 1D defects in approximately the same orientation as that in our model. Specifically, the 1D defects show up as bright spots in the STM images, oriented at an angle of about 42° relative to the <1-10> direction of Au (Fig. 6). Simulating STM images in the Tersoff-Hamann approximation results in a bright line representing the shear plane defect, which makes an angle of 41° relative to the <1-10> direction, in agreement with experiment (Fig. 8c).

From the projected density of states of the theoretical model (Fig. 9), it can be seen that atoms associated with the shear plane have a higher density of states at the Fermi level than those away from the defect or those in the fully-oxidized oxide, suggesting enhanced catalytic activity along shear planes. The predominant contribution to Fermi level states arises from d states of Mo^{5+} (Fig. 9a).

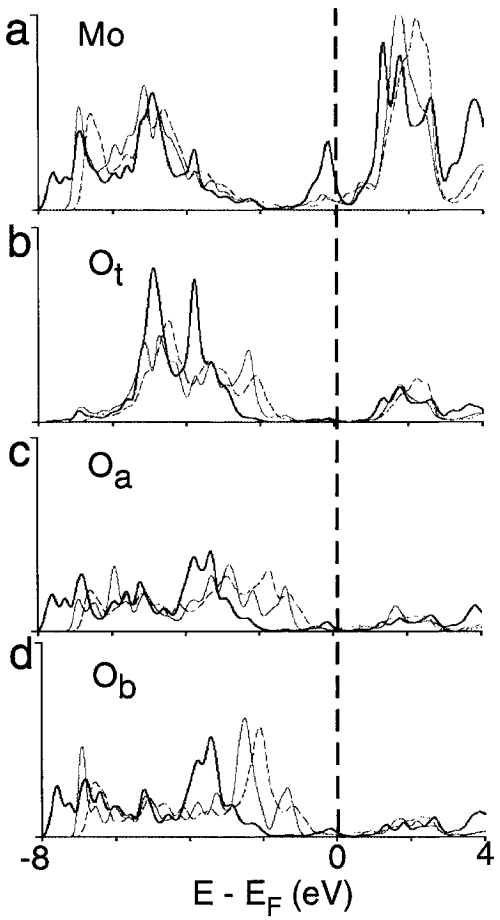

FIG. 9. Electronic densities of states projected onto (a) Mo, (b) O_t, (c) O_a and (d) O_b, summed over s, p and d contributions. Thick red and thin blue curves represent atoms at the shear defect and mid-way between the defects in the reduced oxide (Fig. 8). Dashed black curves represent atoms in the fully oxidized oxide monolayer on Au.

3.2.5 Limitations of model and discussion of other possible structures

It is important to note that the theoretical model proposed here may not accurately represent the experimental system, because the model assumes an infinitely long defect structure. This difference may account for discrepancies between the STM simulation and experimental image, such as the shorter length of defects and presence of black spots in

the experimental image, which also contains a smaller density of defects. Systems involving finite-length-defects or lower densities of defects are more complex and computationally demanding. However, the model represents a possible local atomic structure at the defects and is fairly consistent with experimental results.

The final composition of 1:1 for the ratio of Mo^{5+} to Mo^{6+}, obtained with prolonged annealing, corresponds to the well-defined stoichiometry, Mo_4O_{11}. As this highly reduced system has not been imaged in STM (Fig. 6 corresponds to a lower density of defects), its structure remains an open question. It is interesting that bulk Mo_4O_{11} is the Magneli phase with the highest known density of shear defects.[29] Bulk Mo_4O_{11} has a three-dimensional (3D) structure, with layers of Mo_6O_{22} linked by MoO_4 tetrahedra *via* covalent bonds.[30] It is possible that the final stable Mo_4O_{11} obtained in our system corresponds to bulk Mo_4O_{11}, as the latter does not contain Mo^{4+} and is a stable form of molybdenum oxide. This would present exciting opportunities for fundamental studies because bulk Mo_4O_{11} exhibits charge density wave transitions[30] and it would be interesting to determine how a metallic substrate would affect this phenomenon. Alternatively, it is also possible that the final Mo_4O_{11} retains its 2D structure, similar to that imaged in Fig. 6. This is likely because of possible kinetic barriers for transitioning from a 2D to 3D oxide structure in the presence of the Au substrate. In this case, the resulting stoichiometry could arise from difficulties in reducing the system further due to mutual elastic repulsion between shear defects. The perfectly periodic shear plane model in Fig. 8 in fact corresponds to a defect density of 50 %. However, the absence of a $c(4\times2)$ LEED pattern for this final structure indicates that there is insufficient long-range order for a clear LEED pattern (possibly due to smaller island sizes), in contrast to the

theoretical assumption. Further STM studies will help distinguish between the two possible structures discussed above.

References

[1] S. B. Sinnott and E. C. Dickey, Mater. Sci. Eng. R-Rep. **43**, 1 (2003).

[2] S. Altieri, L. H. Tjeng, and G. A. Sawatzky, Thin Solid Films **400**, 9 (2001).

[3] Z. L. Wang, Annu. Rev. Phys. Chem. **55**, 159 (2004).

[4] J. Haber and E. Lalik, Catal. Today **33**, 119 (1997).

[5] C. Schlenker, *Low-Dimensional Electronic Properties of Molybdenum Bronzes and Oxides* (Kluwer Academic Publishers, 1989).

[6] M. M. Biener and C. M. Friend, Surf. Sci. **559**, L173 (2004).

[7] M. M. Biener, Biener, J., Schalek, R., Friend, C.M., J. Chem. Phys. **121**, 12010 (2004).

[8] L. Kihlborg, Arkiv Kemi **21**, 357 (1963).

[9] J. V. Barth, Brune, H., Ertl, G., Behm, R.J., Phys. Rev. B **42**, 9307 (1990).

[10] G. Kresse and J. Joubert, Phys. Rev. B **59**, 1758 (1999).

[11] P. E. Blochl, Phys. Rev. B **50**, 17953 (1994).

[12] J. P. Perdew and Y. Wang, Phys. Rev. B **45**, 13244 (1992).

[13] G. Kresse and J. Furthmuller, Phys. Rev. B **54**, 11169 (1996).

[14] J. Tersoff and D. R. Hamann, Phys. Rev. Lett. **50**, 1998 (1983).

[15] H. Ibach and D. L. Mills, *Electron Energy Loss Spectroscopy and Surface Vibrations.* (Academic Press, New York, NY, 1982).

[16] M. Chen, Waghmare, U.V., Friend, C.M., Kaxiras, E., J. Chem. Phys. **109**, 6854 (1998).

[17] A. Papakondylis and P. Sautet, J. Phys. Chem. **100**, 10681 (1996).

[18] S. H. Overbury, P. A. Bertrand, and G. A. Somorjai, Chem. Rev. **75**, 547 (1975).

[19] L. Z. Mezey and J. Giber, Jpn. J. Appl. Phys. **21**, 1569 (1982).

[20] M. El-Batanouny, Burdick, S., Martini, K.M., Stancioff, P., Phys. Rev. Lett. **58**, 2762 (1987).

[21] T. C. Z. Song, Z. Chang, G. Liu, J.A. Rodriguez, J. Hrbek, J. Am. Chem. Soc. **125**, 8059 (2003).

[22] S. A. Chambers, Surf. Sci. Rep. **39**, 105 (2000).

[23] S. Surnev, Kresse, G., Ramsey, M.G., Netzer, F.P., Phys. Rev. Lett. **87**, 086102 (2001).

[24] V. E. Henrich and P. A. Cox, *The Surface Science of Metal Oxides* (Cambridge University Press, 1994).

[25] K. Queeney and C. M. Friend, Chemphyschem **1**, 116 (2000).

[26] M. A. Banares, J. L. G. Fierro, and J. B. Moffat, J. Catal. **142**, 406 (1993).

[27] M. Chen, C. M. Friend, and E. Kaxiras, J. Am. Chem. Soc. **123**, 2224 (2001).

[28] K. T. Queeney and C. M. Friend, J. Phys. Chem. B **102**, 5178 (1998).

[29] L. A. Bursill, Proceedings of the Royal Society of London Series a-Mathematical and Physical Sciences **311**, 267 (1969).

[30] E. Canadell, M. H. Whangbo, C. Schlenker, and C. Escribefilippini, Inorganic Chemistry **28**, 1466 (1989).

Chapter 4

Au(110) thin films on ultrathin titania

4.1 Active role of buried ultrathin oxide layers in adsorption of O_2 on Au films

Ultrathin oxide layers are thought to exhibit special behavior by enabling the coupling of structural distortions and charge transfer beyond that allowed in the bulk. In this work, we show from first-principles calculations that ultrathin layers of titania, a prototypical oxide, are active in stabilizing adsorption of O_2 on Au overlayers. The adsorbed O_2 molecules induce charge redistribution in Au that penetrates to the Au-titania interface, which responds through structural distortions that lower the total energy of the system. We suggest that this effect may be of more general nature and useful in catalysis.

This work has been accepted for publication as an article in Surface Science: S. Y. Quek, C. M. Friend, E. Kaxiras, Surface Science, *in press*.

4.1.1 Introduction

Ultrathin oxide films have attracted immense interest because of their numerous technological applications.[1] In parallel development, oxide-supported metal nanostructures have been shown to be useful as sensors[2] and catalysts.[3] In particular, the oxide support can enhance the catalytic activity of the metal nanostructure by altering its electronic properties prior to catalysis, via charge transfer[4, 5] and strain.[6, 7] In this work, we propose that when the support is an ultrathin reducible oxide film, atoms at the buried metal-oxide interface can rearrange in response to the presence of adsorbates on the metal film, provided the latter is sufficiently thin. This atomic relaxation at the interface lowers

the total energy of the system, thereby stabilizing adsorption. We call the ability of interfacial atoms to rearrange during adsorption 'dynamic interface fluxionality'. We demonstrate this effect on a model structure consisting of a thin Au film on an ultrathin titania layer supported on a molybdenum slab, and suggest that it will be of more general nature. Specifically, we expect that when the metal film forms strong covalent bonds with the reducible ultrathin oxide layer, while the latter does not interact strongly with its support to render it a rigid structure, dynamic interface fluxionality can take place. This effect may be exploited to design better catalysts and sensors by replacing traditional reducible oxide supports with ultrathin oxide films. Recent advances in the control of ultrathin film growth[8] indicate that this is a practical possibility.

An oxide/metal system that has attracted tremendous attention is that of oxide-supported Au nanoparticles and films, which act as excellent catalysts.[9] Theoretical studies indicate that the active sites include under-coordinated Au atoms[10, 11] with rough orbitals,[12] and sites at the Au-oxide interface.[13, 14] Experiments also suggest that the activity of titania-supported Au films increases markedly when the Au thickness is reduced to one nearest neighbor distance in bulk Au (so-called 'bilayers').[15] A key insight from theoretical studies was that the ability of Au atoms in a nanoparticle to rearrange in response to adsorbates is essential for O_2 adsorption;[16] this effect was called 'fluxionality' of the nanoparticle. Here, we show that the notion of fluxionality can be extended to the Au-oxide interface for ultrathin Au films on ultrathin reduced titania.

4.1.2 Motivation

The possibility of wetting an ultrathin titania support with Au films was recently demonstrated, with Mo(112) as a substrate on which the TiO_2 thin film was grown.[15] CO

oxidation activity in this system was > 45 times greater than that reported for other Au/titania catalysts. The atomic structure of this system is unknown. However, two salient features are the strong interaction between Au and titania through Au-Ti bond formation, and the presence of ultrathin reduced titania beneath the Au film. Both of these effects have precedent in other systems.[17, 18] Reducible oxides grown on a metal substrate have lower oxidation states than bulk phases due to the reducing character of the metal surface (in the present case, Mo).[17] On bulk TiO_2 surfaces, Au binds almost exclusively to reduced Ti sites.[18] The availability of such sites throughout the ultrathin titania film thus allows wetting by Au. What is not clear, however, is how a strong interaction with buried ultrathin titania, or a small Au thickness, can enhance the activity of Au/titania catalysts.[19]

Motivated by these questions, and knowledge that the CO oxidation rate is limited by the availability of O_2 or adsorbed O on the catalyst,[13, 20] we study O_2 and O adsorption in a model ultrathin Au/titania system.

4.1.3 Choice of model

We first explain our choice of a structural model for this system. While this model may not be an exact representation of the experimental system (the atomic structure of which remains undetermined) it has been constructed by taking into account information from various experiments as well as from extensive simulations. More specifically, our model is motivated by the following observations.

Firstly, the substrate consists of a Mo(112) surface, which has a row-and-trough structure that makes it a useful substrate for ultrathin oxide growth. It has been proposed

that the oxide grows along the troughs, forming O-Mo bonds.[21] Our simulations confirm that this is energetically preferred.

Secondly, assuming that the Ti and Mo have the same periodicity along the troughs (as suggested by LEED experiments) leads to an interface structure in which the Ti atom positions are compatible with a Au(110) lattice strained by 9.1 and –5.5% in the [001] and [1$\bar{1}$0] directions, respectively. Au(110) layers, with strains of 12.5 and –7.5% along these directions, have previously been grown on anatase TiO_2(110) up to length-scales of at least 4 nm and thicknesses of at least 4 layers, as shown by high resolution transmission electron microscopy.[22] Thus, with suitable growth procedures, it is plausible that the titania/Mo system can support 1 or 2 Au(110) layers over length-scales significantly greater than 4nm. We determined the most stable such structure, shown in Fig. 1, by exploring 37 distinct initial geometries.

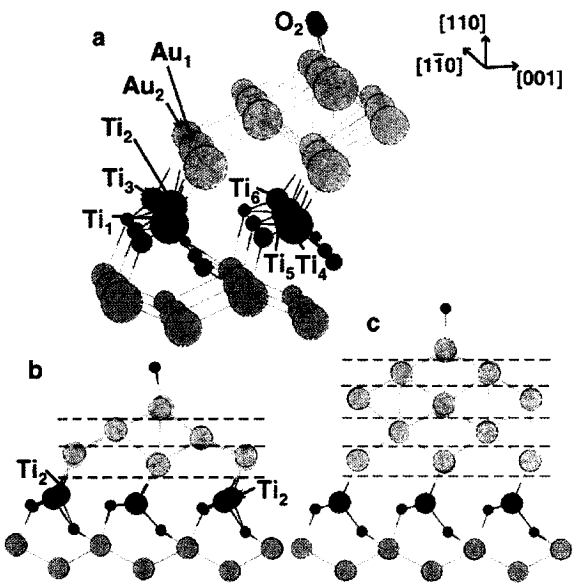

FIG. 1. (a) O_2 adsorbed on titania/Au_3. (b) View of (a) down the [1$\bar{1}$ 0]-direction. (c) O_2 adsorbed on titania/Au_5. Red, blue, gold and gray circles denote O, Ti, Au and Mo respectively. Only the top two layers of the Mo slab are shown. Crystallographic

directions corresponding to those of the Au layers are indicated. Dashed lines separate the Au(110) films into 3 Au planes in titania/Au_3, and 5 in titania/Au_5. On the clean Au surface, all atoms are equivalent by periodicity in the $[1\bar{1}0]$-direction; Ti rows directly beneath the troughs of the Au(110) layers are also equivalent by periodicity. Thus, calculations with the clean Au surface have two Ti atoms per unit cell. For calculations with adsorbates, the period in the $[1\bar{1}0]$-direction of Au(110) is tripled; inequivalent atoms at the interface after O_2 adsorption are labeled for reference in the text.

Thirdly, although the Ti:O stoichiometry in this favored structure is 1:2, the oxide is not fully oxidized since O is bonded to strongly-reducing Mo. The oxide atoms are arranged in a motif present on rutile TiO_2(110), the most stable crystal face of TiO_2.

Fourthly, each titania row corresponds to a row of bridging O vacancies on this surface. Such vacancies are common and can form complete rows.[23] Au can nucleate at these vacancies,[18] forming Au-Ti bonds in a similar geometry as in our model.[23]

We refer to the structures with 1 and 2 Au(110) layers, which consist of 3 and 5 distinct planes of Au atoms on the oxide layer, respectively, as titania/Au_3 (shown in Fig. 1(a)-(b)) and titania/Au_5 (shown in Fig. 1(c)).

4.1.4 Computational details

To investigate the adsorption process on this model system, we have performed first-principles calculations based on density functional theory (DFT) as implemented in VASP.[24] We used the projected augmented wave method[25] with the generalized gradient approximation for the exchange-correlation functional (PW-91)[26] and scalar relativistic pseudopotentials to represent the atomic cores. The Mo substrate was modeled by a 6-

layer slab. The bottom 3 Mo layers were held fixed at their bulk positions, and all other atoms were relaxed until the atomic forces were smaller in magnitude than 0.05eV/Å. The vacuum region separating slabs was taken to have thickness of $\geq$ 11Å, and reciprocal space sampling was performed on a *k*-point mesh of 6 × 12 per (1 × 1) Mo(112) surface unit cell; these computational parameters ensure adequate accuracy in the reported values, as determined by careful convergence studies. Spin-polarization was included in calculating the energies of structures involving O_2 molecules.

4.1.5 Results and discussion

Fig. 1 shows O_2 adsorbed at its most favorable site (involving under-coordinated Au atoms) in a 'top-bridge-top' geometry. This is consistent with other DFT studies of O_2 adsorption on Au surface steps[6] and Au clusters.[12, 27] Adsorption of O_2 is accompanied by a charge transfer from Au to the O_2 unoccupied anti-bonding orbitals. The adsorption energies are –0.18eV in titania/Au_3 and –0.03eV in titania/Au_5. At other sites, this energy is positive, indicating repulsive interactions. It is likely that O_2 adsorbs more strongly than predicted by these values, because the calculated bond enthalpy of isolated O_2 molecules is –6.65eV, while the experimentally measured value is –5.25eV;[28] in other words, the reference configuration for adsorption energies, with the O_2 molecule far from the surface, is disproportionally favored due to the overestimation of the molecular bond enthalpy, as is common in DFT calculations of the type reported here.[28] We note, however, that all subsequent discussion and conclusions are based entirely on *relative* adsorption energies, which are well-described by DFT and are not affected by this problem.

In titania/Au_3, O_2 adsorption causes the bonds between the pairs of atoms Au_2-Ti_2 and Au_1-Ti_2 to shorten by 2.2 and 2.5%, and those between the pairs Au_2-Ti_3 and Au_1-Ti_1 to lengthen by 5.8 and 6.2%. No such distortion is observed in titania/Au_5, where the Au-Ti bond lengths change by less than 1.1% upon O_2 adsorption. When the titania/Mo support and Au atoms in contact with it are held fixed, the adsorption energy in titania/Au_3 becomes –0.04eV, 0.14eV higher than the value with full relaxation. The corresponding energy change in titania/Au_5 is only 0.01eV. Thus, the interface distortion observed in titania/Au_3 plays a major role in stabilizing O_2 adsorption.

The different behavior of the two structures could be due to several factors. One possibility is the difference in densities of states (DOS) near the Fermi level, projected onto the Ti atoms. However, the Ti-projected DOS are similar in the two systems (Fig. 2).

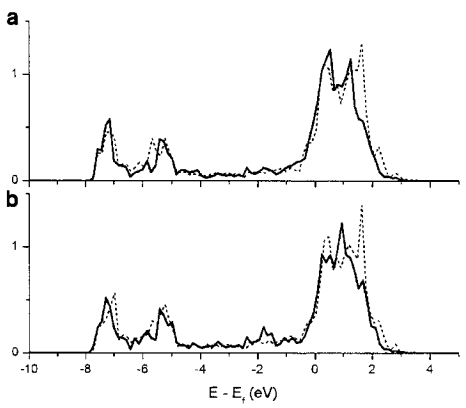

FIG. 2. Projected densities of states (DOS) on Ti atoms directly beneath the Au layers: (a) Ti atoms in Au troughs (labeled Ti_1, Ti_2, Ti_3 in Fig. 1a); (b) Ti atom in Au bridges (labeled Ti_4, Ti_5, Ti_6 in Fig. 1a), in titania/Au_3 (solid lines) and titania/Au_5 (dashed lines), for systems without adsorbates. DOS are in units of number of states per unit energy per unit cell, and are projected onto spherical harmonics

centered on the Ti atoms (within spheres of radii 1.323 Å), summed over *s*, *p* and *d* contributions. The DOS close to the Fermi levels (E_f) are very similar in the two systems.

The absence of interface distortions in titania/Au_5 is therefore likely to be due to the thicker Au film. This may be related to the relative stability of titania/Au_5 compared to titania/Au_3: the thicker Au film in titania/Au_5 results in a larger cohesive energy, although actual relative stabilities will have to be evaluated by including a chemical potential for Au that is appropriate for the growth conditions. Analysis of the charge density distribution also shows that the thicker Au film effectively screens the buried interface from the effect of O_2 adsorption. Specifically, charge density difference plots show that charge transfer to O_2 induces a charge redistribution between the Au planes that is inhomogeneous in the $[1\bar{1}0]$-direction, but the inhomogeneity disappears for $n \geq 3$ in titania/Au_5 (Fig. 3).

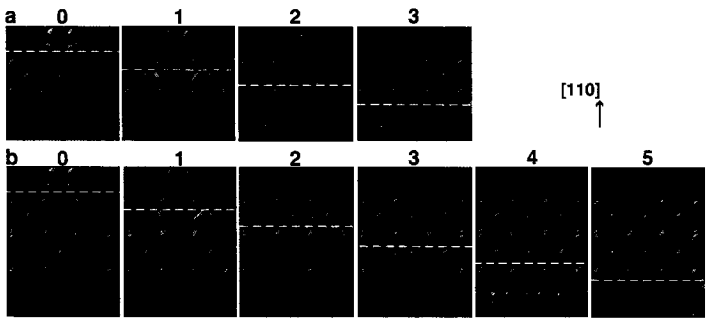

FIG. 3. Charge density difference isocontours (pale gray) for O_2 adsorbed on (a) titania/Au_3 and (b) titania/Au_5. Atoms are shown with the same symbols as in Fig 1 (the Mo substrate is not shown). The systems are viewed down the [001]-directions. The charge density difference is calculated by splitting the systems into two components: (i) the adsorbed O_2 on *n* Au planes, and (ii) the remaining Au planes and the titania/Mo

support; the charge difference is between superposition of the two components (separated by a dashed white line in each panel) each considered separately and the entire system. Each panel is labeled by *n*, the number of Au planes in the first component, which ranges from 0-3 for titania/Au_3 and from 0-5 for titania/Au_5. The isocontour plots (positive values) indicate how charge is redistributed due to interaction between the two parts of each system (schematically denoted by the dashed line). For example, the panels labeled '0' indicate that charge is transferred from the Au/titania/Mo system to O_2. Panel '3' in (a) shows that there is an inhomogeneous distribution of charge among the Ti-Au bonds in titania/Au_3, in contrast to the more homogeneous charge distribution in panel '5' for titania/Au_5 in (b).

O_2-induced charge inhomogeneity in Au is thus screened out beyond a depth of approximately 3Å (one nearest-neighbor distance in bulk Au) below O_2, which corresponds to about 3 Au planes in titania/Au_5. To quantify this effect, we use the Bader method[29, 30] to evaluate the charge contribution to O_2 from each Au plane in the films (Fig. 1). Unlike Mulliken charge assignments, the Bader method is independent of the choice of basis. The charge contribution from the *n*th Au plane beneath O_2 decreases exponentially with *n*, with zero contribution from the 5^{th} plane beneath O_2 in titania/Au_5 (Table 1). Titania beneath the thicker Au film is thus insensitive to the O_2 adsorption geometry, precluding O_2-induced structural distortions at the interface. In contrast, the Au-titania interface in titania/Au_3 can distort in response to charge inhomogeneity in the $[1\bar{1}0]$-direction.

	1	2	3	4	5	titania/Mo	**Total**
Titania/Au_3	0.31	0.12	0.03	-	-	0.05	0.51
Titania/Au_5	0.32	0.10	0.04	0.01	0.00	0.04	0.51

TABLE 1. Charge gained (in *e*) per O_2. Column *n* gives the charge gained by O_2 from the *n*th Au plane beneath O_2, calculated by subtracting the charge on O_2 when it is attached to *n* planes, from the corresponding charge with $(n - 1)$ planes. Values in column *n* are $\approx 3 \times$ those in column $n + 1$. The titania/Mo support contributes charge to O_2 by changing the overall Au charge.

Au interacts with titania by forming predominantly covalent bonds with Ti, as reported in previous studies.[23, 31] The interface distortion in titania/Au_3 is accompanied by a marked increase in covalency between the atom labeled Ti_2 and its nearest Au neighbors. Correspondingly, O_2 adsorption results in a 0.14e increase in charge on atom Ti_2 in titania/Au_3. In contrast, the Ti charges in titania/Au_5 do not change by more than 0.01e. The O_2-induced interface distortions in titania/Au_3 are therefore related to changes in the Au-Ti bonding.

This change in Au-Ti bonding is related to the reducibility of titania. In reducible oxides, the occupation of valence metal *d*-orbitals can change with little energy cost. As on bulk TiO_2 surfaces, vacancy-induced states in our models have Ti 3*d* character. In TiO_2(110), these states appear in the band-gap of the oxide.[32] In our models, the concentration of vacancies is so high that Ti 3*d* states occur at the Fermi level. The energy cost to alter the Au-Ti bonding by changing the occupation of Ti 3*d* orbitals is therefore negligible. This picture should be contrasted to that of Au interacting with vacancies on irreducible oxides

such as alumina. In the latter case, the simple metal Al easily loses all its valence electrons to its neighbors, forming a stable closed shell ion, Al^{3+}. It would be energetically unfavorable for Al^{3+} to change its electronic configuration during catalysis. To check this hypothesis, we have performed calculations using the same types of structures shown in Fig. 1, with Ti replaced by Al. As expected, we find no O_2-induced interface distortion in the alumina/Au structures.

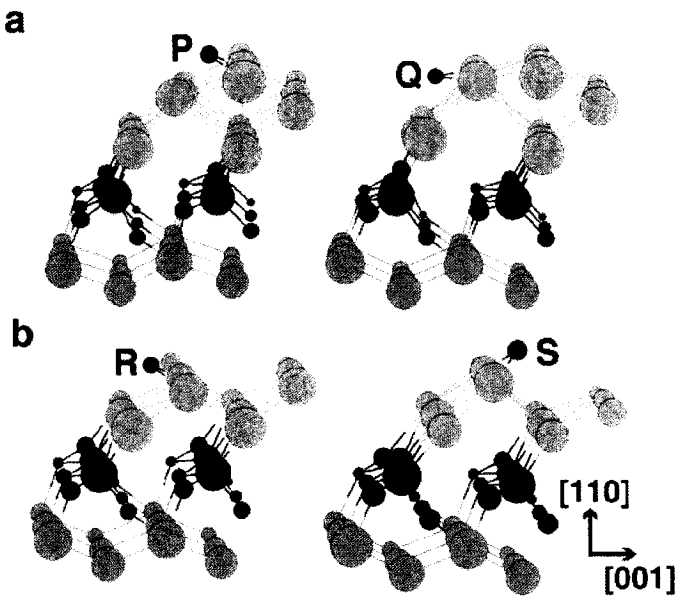

FIG. 4. O adsorbed in (a) titania/Au_3 and (b) titania/Au_2. We show adsorption at the 2 most stable sites in each case, out of a total of 6 sites considered in (a) and 4 in (b).

The adsorption of individual O atoms on titania/Au_3 also induces stabilizing interface distortions. Fig. 4(a) shows O adsorbed at the 2 most stable sites (out of a total 6 sites that we have considered). As in O_2 adsorption, the most favorable adsorption site (P) involves under-coordinated Au atoms. The adsorption of individual H on the Au film, relevant to hydrogenation reactions in Au catalysis,[33] also induces similar interface distortions. This shows that the ability to induce such distortions in titania/Au_3 is not

limited to O_2. These general observations are quantified by detailed analysis of the energetics and structural distortions of the relevant structures, given in Table 2.

a. titania/Au_5

	BE (eV)	dE_{relax} (eV)	$d\rho_{max}$ (e) [site]	$dl(Au\text{-}Ti)_{max}$ (%)	$dl(Au\text{-}Au)_{max}$ (%)
O_2	-0.03	0.01	–	1.2 (0.0)	7.7 (3.9)

b. titania/Au_3

	BE (eV)	dE_{relax} (eV)	$d\rho_{max}$ (e) [site]	$dl(Au\text{-}Ti)_{max}$ (%)	$dl(Au\text{-}Au)_{max}$ (%)
O_2	-0.18	0.14	0.14 [Ti_2]	6.2 (0.0)	-13.1 (-10.8)
O (P)	-3.56	0.19	0.15 [Ti_1]	6.2 (0.0)	-12.5 (13.1)
O (Q)	-3.43	0.13	0.09 [Ti_3]	5.7 (0.0)	19.8 (13.9)
H (P)	-2.26	0.10	0.11 [Ti_2]	5.1 (0.0)	-11.1 (6.7)

c. titania/Au_2

	BE (eV)	dE_{relax} (eV)	$d\rho_{max}$ (e) [site]	$dl(Au\text{-}Ti)_{max}$ (%)	$dl(Au\text{-}Au)_{max}$ (%)
O (R)	-3.40	0.07	-0.03 [Ti_3]	-1.5 (0.0)	8.9 (6.7)
O (S)	-3.34	0.25	0.12 [Ti_2]	11.0 (0.0)	6.8 (12.0)
H	-2.25	0.11	0.05 [Ti_2]	5.8 (0.0)	5.8 (5.8)

TABLE 2. Adsorption in (a) titania/Au_5, (b) titania/Au_3 and (c) titania/Au_2. *BE* is the adsorption energy with respect to the isolated adsorbate and clean surface. dE_{relax}, $d\rho_{max}$, $dl(Au\text{-}Ti)_{max}$ and $dl(Au\text{-}Au)_{max}$ are described in the text. Values in brackets in columns $dl(Au\text{-}Ti)_{max}$ and $dl(Au\text{-}Au)_{max}$ are the corresponding changes obtained when the Ti atoms and Au atoms in contact with them are held fixed during adsorption. As $d\rho_{max}$ is within 0.02e in all constrained relaxations, only values of $|d\rho_{max}| > 0.02$e are given, with the corresponding Ti sites in square brackets (using the labeling scheme of Fig. 1(a)).

When the titania/Mo support and Au atoms in contact with it are held fixed, the local adsorbate-Au geometry remains similar, but the adsorption energy diminishes in titania/Au_3. The differences dE_{relax} in energies between the fully relaxed and constrained systems are 0.19 and 0.13eV for O at the sites P and Q, and 0.10eV for H at site P; this

energy is 0.14eV for adsorption of O_2, as discussed earlier. As a point of comparison, DFT studies have shown that O adsorption is 0.16eV more stable on step defects than on a flat Au(111) surface.[7] The values of dE_{relax} are therefore significant in stabilizing adsorption. Table 2 also summarizes the adsorption-induced changes in bond lengths and Ti charges. In titania/Au_3, the maximum change in Ti charge, $d\rho_{max}$, varies from 0.09e to 0.15e and the maximum change in bond length, $dl(Au\text{-}Ti)_{max}$, from +5.1 to +6.2%. Values of $dl(Au\text{-}Au)_{max}$, the maximum change in Au-Au bond lengths, are significant, ranging from -13.1 to 19.8%. This is expected since the adsorbates are directly adsorbed onto the Au films, and similar changes in Au-Au bond lengths are also observed in the constrained relaxations (given in brackets in Table 2).

An important consideration is to what extent the Au film structure assumed in our model influences the results. In order to assess this, we considered a different model, referred to as titania/Au_2, in which the top row of Au atoms from the titania/Au_3 structure has been removed (shown in Fig. 4(b)). The resulting Au film is a (1 × 1) Au(110) monolayer, in contrast to the (2 × 1) Au(110) films in titania/Au_3 and titania/Au_5. The latter films have a surface reconstruction that is characteristic of bulk Au(110) but may be unnecessary for Au(110) monolayers. Overall, adsorption of single O atoms has similar effects on interface distortions and charge transfer in titania/Au_2 as in titania/Au_3 as seen from the relevant quantities in Table 2. In the case of H atom adsorption, interface distortions at the most favorable site in titania/Au_2 are significant and comparable to those in titania/Au_3.

4.1.6 Concluding remarks

While reaction barriers are important for catalytic applications, larger adsorption energies have implications for catalysis because the availability of adsorbed reactants is a major rate-limiting factor for Au-based catalysts.[7] We have shown that interface fluxionality is essential in promoting adsorption of O_2 on ultrathin Au layers supported on ultrathin titania, and that this effect is lost when the metal layers become thicker. Further studies, involving larger scale simulations that incorporate dynamical and kinetic effects, are required to access the stability of these films under reaction conditions. This stability has implications for the lifetime of catalysts and sensors, and is known to be a major problem for catalysts utilizing Au nanoparticles, which deactivate over time through agglomeration.[34]

Our results are promising in the context of recent experimental advancements in the growth of ultrathin nanostructures on surfaces. For example, metastable nanostructures of reducible oxides have been grown on metal surfaces,[17] and the reducing character of the metal substrate helps create active vacancy sites across the supported ultrathin oxide,[17] which can allow wetting by transition metal catalysts.[15] The oxidation state of supported oxide nanostructures can also be tailored, in two-dimensional titania nanostructures on Au(111), for example.[35] Such oxide nanostructures and ultrathin films are likely to have much more flexibility to distort in response to adsorbates, compared to bulk oxide supports. The control of the features of nanostructures on substrates that can exhibit interface-fluxionality suggests that improved catalysts and sensors can be designed by replacing traditional reducible oxide supports by ultrathin oxide films.

References

[1] M. Fernandez-Garcia, A. Martinez-Arias, J. C. Hanson, and J. A. Rodriguez, Chem. Rev. **104**, 4063 (2004).

[2] R. J. Wu, C. H. Hu, C. T. Yeh, and P. G. Su, Sensor Actuat. B-Chem. **96**, 596 (2003).

[3] P. L. Gai, R. Roper, and M. G. White, Curr. Opin. Solid. St. M. **6**, 401 (2002).

[4] B. Yoon, H. Hakkinen, U. Landman, A. S. Worz, J. M. Antonietti, S. Abbet, K. Judai, and U. Heiz, Science **307**, 403 (2005).

[5] Z. P. Liu, S. J. Jenkins, and D. A. King, Phys. Rev. Lett. **94**, 196102 (2005).

[6] Y. Xu and M. Mavrikakis, J. Phys. Chem. B **107**, 9298 (2003).

[7] M. Mavrikakis, P. Stoltze, and J. K. Nørskov, Catal. Lett. **64**, 101 (2000).

[8] S. A. Chambers, Surf. Sci. Rep. **39**, 105 (2000).

[9] M. Haruta, S. Tsubota, T. Kobayashi, H. Kageyama, M. J. Genet, and B. Delmon, J. Catal. **144**, 175 (1993).

[10] I. N. Remediakis, N. Lopez, and J. K. Nørskov, Angew. Chem. Int. Edit. **44**, 1824 (2005).

[11] N. Lopez, T. V. W. Janssens, B. S. Clausen, Y. Xu, M. Mavrikakis, T. Bligaard, and J. K. Nørskov, J. Catal. **223**, 232 (2004).

[12] G. Mills, M. S. Gordon, and H. Metiu, J. Chem. Phys. **118**, 4198 (2003).

[13] Z. P. Liu, X. Q. Gong, J. Kohanoff, C. Sanchez, and P. Hu, Phys. Rev. Lett. **91**, 266102 (2003).

[14] L. M. Molina, M. D. Rasmussen, and B. Hammer, J. Chem. Phys. **120**, 7673 (2004).

[15] M. S. Chen and D. W. Goodman, Science **306**, 252 (2004).

[16] H. Hakkinen, W. Abbet, A. Sanchez, U. Heiz, and U. Landman, Angew. Chem. Int. Edit. **42**, 1297 (2003).

[17] S. Surnev, G. Kresse, M. G. Ramsey, and F. P. Netzer, Phys. Rev. Lett. **87**, 086102 (2001).

[18] E. Wahlstrom, N. Lopez, R. Schaub, P. Thostrup, A. Ronnau, C. Africh, E. Laegsgaard, J. K. Nørskov, and F. Besenbacher, Phys. Rev. Lett. **90**, 026101 (2003).

[19] C. T. Campbell, Science **306**, 234 (2004).

[20] V. A. Bondzie, S. C. Parker, and C. T. Campbell, Catal. Lett. **63**, 143 (1999).

[21] M. S. Chen, W. T. Wallace, D. Kumar, Z. Yan, K. K. Gath, Y. Cai, Y. Kuroda, and D. W. Goodman, Surf. Sci. **581**, L115 (2005).

[22] S. Giorgio, C. R. Henry, B. Pauwels, and G. Van Tendeloo, Mat. Sci. Eng. A-Struct **297**, 197 (2001).

[23] N. Lopez, J. K. Nørskov, T. V. W. Janssens, A. Carlsson, A. Puig-Molina, B. S. Clausen, and J. D. Grunwaldt, J. Catal. **225**, 86 (2004).

[24] G. Kresse and J. Furthmuller, Phys. Rev. B **54**, 11169 (1996).

[25] P. E. Blochl, Phys. Rev. B **50**, 17953 (1994).

[26] J. P. Perdew and Y. Wang, Phys. Rev. B **45**, 13244 (1992).

[27] A. Sanchez, S. Abbet, U. Heiz, W. D. Schneider, H. Hakkinen, R. N. Barnett, and U. Landman, J. Phys. Chem. A **103**, 9573 (1999).

[28] J. P. Perdew, K. Burke, and M. Ernzerhof, Phys. Rev. Lett. **77**, 3865 (1996).

[29] R. F. W. Bader, *Atoms in Molecules - A Quantum Theory* (Oxford University Press, New York, 1990).

[30] G. Henkelman, A. Arnaldsson, and H. Jónsson, Comput. Mat. Sci. **36**, 254 (2006).

[31] J. A. Rodriguez, G. Liu, T. Jirsak, J. Hrbek, Z. P. Chang, J. Dvorak, and A. Maiti, J. Am. Chem. Soc. **124**, 5242 (2002).

[32] J. A. Rodriguez, J. Hrbek, Z. Chang, J. Dvorak, T. Jirsak, and A. Maiti, Phys. Rev. B **65**, 235414 (2002).

[33] G. C. Bond and D. T. Thompson, Catal. Rev.-Sci. Eng. **41**, 319 (1999).

[34] M. Valden, X. Lai, and D. W. Goodman, Science **281**, 1647 (1998).

[35] J. Biener, E. Farfan-Arribas, M. Biener, C. M. Friend, and R. J. Madix, J. Chem. Phys. **123**, 094705 (2005).

Chapter 5

Structure of incommensurate gold sulfide monolayer on Au(111)

5.1 Abstract

Two-dimensional confined systems, such as substrate-supported incommensurate layers, are of interest because of their unique structural and electronic properties that differ from those of bulk materials. While advances in experimental techniques have resulted in the growth of many such interesting systems, progress can often be hampered by the lack of an atomistic-scale understanding of the structure, especially for incommensurate systems. In this work, we develop an atomic-scale model for an ordered incommensurate gold-sulfide (AuS) adlayer that has been previously demonstrated to exist on the Au(111) surface, following sulfur deposition and annealing to 450 K. We introduce theoretical techniques within density functional theory to take into account charge transfer in an incommensurate system, and obtain scanning tunneling microscopy images in good agreement with experiment. Our simulations indicate that this model is remarkably robust. We analyze the nature of bonding in this structure using state-of-the-art Wannier-function based techniques. Our analysis provides a natural explanation for the extraordinary robustness and unusual stoichometry of this layer. This structure and its chemistry have implications for related S-Au interfaces, such as those in self-assembled monolayers of thiols on Au substrates.

This chapter describes work done with M.M. Biener, J. Biener, J. Bhattacharjee, U.V. Waghmare, under the supervision of Prof. Kaxiras and Prof. Friend. A summary of this work has been published as a letter in Journal of Physical Chemistry B:

S. Y. Quek, M. M. Biener, J. Biener, J. Bhattacharjee, U.V. Waghmare, C. M. Friend and E. Kaxiras, Journal of Physical Chemistry B **110** (32), 15663-15665 (2006).

5.1.1 Introduction

Nano-structured materials, such as two-dimensional confined systems, have attracted immense interest because of their unique structural and electronic properties that differ from those of bulk materials.[1, 2] These systems are promising candidates for many technological applications, including molecular electronic devices, sensors and catalysts.[2-4] Advances in nano-scale growth methods have produced a wealth of systems with interesting properties,[3-5] but progress is often hampered by the lack of an atomistic-scale understanding of their structure, which can be rather complex. In particular, incommensurate structures, which are not uncommon, defy theoretical analysis because the layer and substrate cannot both be treated exactly within a common unit cell.

In this work, we revisit the structure of an incommensurate nano-scale system which is particularly intriguing: a two-dimensional (2D) ordered layer of gold sulfide, formed on the Au(111) surface following sulfur deposition and annealing at 450K.[5, 6] What is interesting about this layer is that it provides fresh insights into the nature of possible precursor states for the bonding of organic molecules (such as alkylthiols) to Au via sulfur, systems that are of great interest in technological applications.[3] Both the incommensurate nature and the unusual stoichiometry of this layer required the development of new theoretical tools in the framework of first-principles calculations. These tools provide a comprehensive picture of the structure and chemistry of the sulfide monolayer that has important implications for a wider range of related applications.

5.1.2 Methods

The scanning tunneling microscopy (STM) experiments were performed in ultra-high vacuum with a base pressure of 4×10^{-10} Torr. The Au(111) surface was cleaned by Ar^+ sputtering at 300 K, followed by annealing to 700 K for 10 min and 600 K for 60 min. The characteristic herringbone reconstruction was observed following this procedure. SO_2 ("Matheson", anhydrous grade) was introduced by chamber backfilling. Only a small fraction of the SO_2 decomposes and deposits sulfur on the Au(111) surface, as monitored by Auger electron spectroscopy. Importantly, no oxygen-containing species was detected on the surface at any time, suggesting that the oxygen released during SO_2 decomposition is removed by an abstraction reaction with excess SO_2.[7] Further experimental details can be found in Reference 5.

All our calculations were performed in the framework of density functional theory with the generalized gradient approximation (PW-91 functional)[8] for the exchange-correlation functional. A plane-wave basis set was used, with scalar relativistic pseudopotentials to represent the atomic cores. Gamma-centered *k*-point meshes of 4×4 and 8×8 were used for calculations with and without the Au substrate respectively. The total energy of structure *A* was converged with a 3×3 *k*-point mesh. At least 10 Å of vacuum was used in each calculation, and convergence of relevant physical quantities was checked with respect to vacuum size. Within this framework, we introduced new theoretical approaches to obtain first, the atomic structure, and second, the bonding characteristics, of the incommensurate AuS layer on Au(111).

In calculations for the atomic structure, we used the projected augmented wave method[9] with an energy cutoff of 280 eV, as implemented in VASP. The Au substrate

was represented by a slab of 6 Au(111) layers, the bottom 3 of which are frozen in their bulk positions. Geometry optimization was performed with a force convergence criterion of 0.05 eV/Å. The resulting structures were used for analysis of bonding characteristics, by constructing localized Wannier functions from the Kohn-Sham wavefunctions. Further details of our theoretical approaches will be described below.

5.1.3 Experimental results

We have previously reported detailed scanning probe studies of the interaction of sulfur with Au(111).[5, 6] These studies established that sulfur interacts with Au(111) in a dynamic, rather than static, manner, with large scale mass transport and the dislodgement of Au terrace atoms to form a gold-sulfide phase.

In short, STM images[5] show that a sulfur coverage of as low as 0.1 ML completely lifts the herringbone surface reconstruction of Au(111) even at room temperature (300 K). At 0.3 ML, an ordered $(\sqrt{3} \times \sqrt{3})$R30° adlayer of adsorbed sulfur atoms is formed. Above this coverage, a dynamic rearrangement of the Au surface occurs, with small islands and monatomic etch pits nucleating on Au terraces, strongly suggesting that Au atoms are removed from terraces into a growing gold sulfide phase that is distinct from that of adsorbed sulfur observed at lower coverages. Similar incorporation of stoichiometric amounts of substrate atoms into adsorbate-induced surface adlayers has been observed in other systems, such as a 2D oxide layer on Pd(111)[10] and a 2D sulfide on Al(111).[11] At a saturation coverage of 0.6 ML, the surface takes on a sponge-like morphology that is completely covered by a 2D layer. Quasi-rectangular ring-like structures with some short-range order are formed when the system is subsequently annealed to 420 K. Similar features have been observed during the

electrochemical deposition of S on Au;[12-15] it was proposed that these rings correspond to strained S_8 molecules. Further annealing to 450 K leads to Ostwald ripening of the original etch pits, resulting in large vacancy islands of monatomic depth. The S coverage drops to approximately 0.5 ML and a 2D layer with long-range order completely covers the Au surface. High-resolution STM images[5] of this ordered 2D phase reveal that the system is incommensurate, with a $(8.8 \pm 0.4)\times(8.2 \pm 0.4)$ Å^2 unit cell and an angle of 82° ± 4° between the lattice vectors. Based on the areas of the vacancy islands, it was estimated that approximately 0.5 ML of Au is incorporated into the ordered 2D sulfide layer, suggesting a Au-S stoichiometry.[5] This stoichiometry is distinct from those of bulk gold sulfides, Au_2S and Au_2S_3.[16]

5.1.4 Atomic structure: Approach and model

The unusual stoichiometry and 2D nature of the gold sulfide layer suggest that it is a novel material distinct from 3D bulk gold sulfides. To understand this interesting material, we proceed to construct an atomic-scale model for this system. The incommensurate nature implies that the AuS layer does not interact strongly with the Au surface (this picture is later confirmed using Wannier orbital analysis of bonding). We therefore consider the system in two stages. First, we determine the atomic structure of an isolated AuS layer in a fixed unit cell consistent with experimental measurements, and in a fully relaxed cell. Next, we analyze how the substrate affects the atomic and electronic structure of this layer, the latter in a manner which takes into account the incommensurate nature of the interaction by averaging over several different configurations.

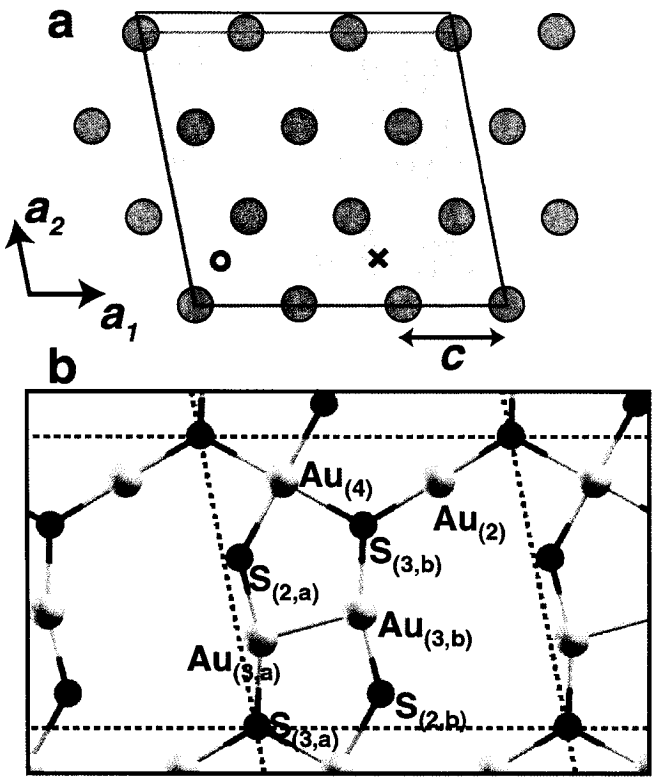

FIG. 1. (a) Proposed orientation of AuS unit cell (black box). (b) Atomic structure of *A*. Numerical subscripts denote the coordination of each atom and letter subscripts indicate inequivalent atoms of the same coordination. The cross and circle in (a) mark sites **X** and **O** respectively, relevant to structure *B* described in the text.

In the first step, given the Au(111) surface lattice, a natural choice for the fixed unit cell is given by the black box in Fig. 1(a): this cell has a lattice constant of 8.65 Å (3 times that of Au) in direction $\boldsymbol{a}_1$, and a lattice angle of 79°, both values within experimental error bars (8.65 Å is within the range of 8.4 Å to 9.2 Å for the 1st lattice constant). The lattice constant in direction $\boldsymbol{a}_2$ was fixed at the experimental value of 8.20 Å, which is not a simple multiple of the Au lattice constant. We considered several models with different numbers of atoms per unit cell, with stoichiometry Au:S = 1:1, and

different arrangements of these atoms, using for guidance information on the local coordination chemistry of Au and S in known compounds.[17, 18] Fully relaxing the positions of these atoms within the fixed unit cell resulted in only one stable structure (in all other structures, the atoms rearranged drastically and the atomic forces sometimes do not converge). The stable structure, which we call *A*, is planar with 4 Au and 4 S atoms per unit cell (Fig. 1(b)). Details of bond lengths are given in Table 1(a). The corresponding S coverage is 0.41 ML, assuming that a completely flat, unreconstructed Au(111) surface is entirely covered by the AuS layer. This coverage is close to the experimental estimate of 0.5 ML, taking into account the attachment of S atoms to the edges of Au vacancy islands present on the annealed, sulfide-covered Au(111) surface, and possible uncertainty in the experimental calibration.

(a)

Bonds	Structure *A*	Fully relaxed, neutral layer	Fully relaxed, charged layer
$Au_{(2)}$-$S_{(3)}$	2.41	2.29 (–5.0 %)	2.34 (–2.9 %)
$Au_{(3)}$-$S_{(2)}$	2.33	2.25 (–3.4 %)	2.30 (–1.3 %)
$Au_{(3)}$-$S_{(3)}$	2.41	2.28 (–5.4 %)	2.35 (–2.5 %)
$Au_{(4)}$-$S_{(2)}$	2.45	2.37 (–3.3 %)	2.42 (–1.2 %)
$Au_{(4)}$-$S_{(3)}$	2.58	2.37 (–8.1 %)	2.43 (–5.8 %)
$Au_{(3,a)}$-$Au_{(3,b)}$	2.87	2.88 (+0.3 %)	2.85 (–0.7 %)

(b)

Systems	Formal oxidation state of Au	Bonds (coordination)	Bond lengths
bulk Au_2S	I	Au-S (linear)	2.17[17]
Compounds with Au^{III}-S	III	Au-S (square-planar)	2.30-2.35[18]
Compounds with Au^{III}-S, with S bridging 2 Au^{III}	III	Au-S (square-planar)	2.40[18]
Compounds with covalent Au^{II}-Au^{II} bonds	II	Au-Au	2.60[18]
Compounds with weaker Au^{I}-Au^{I} aurophilic interaction	I	Au-Au	3.10[18]

TABLE 1. Bond lengths (in Å) in (a) structure *A*, and in the fully relaxed neutral and charged (3.3 *e*/cell) layers, and (b) in known compounds containing Au-S and Au-Au bonds. Values in brackets in (a) are the % changes in bond lengths relative to that in *A*.

We next allow the unit cell parameters to relax without any constraints: this resulted in an almost uniform shrinking of *A*. The lattice angle changed to 78° (which is within experimental error bars and close to the corresponding angle in *A* of 79°). The new lattice constants are 7.85 Å and 7.65 Å, which are respectively 9.3% and 6.7% smaller than the corresponding lattice constants in *A*. However, the ratio between lattice constants is 1.04, close to the corresponding ratio of 1.05 in *A*. The atomic geometry also remains very similar to that in *A* (Fig. 7(a) (please see section 5.1.6)). This shows that the atomic structure and unit cell *shape* in *A* are robust. The relaxed unit cell is too small to fit within experimental error bars (the lower bound in experiment being 8.4×7.8 Å^2). However, the shrinking of the unit cell is consistent with the shorter bond lengths found in bulk Au_2S[17] and other compounds with Au-S bonds[18] (Table 1). As discussed below, the larger unit cell observed in experiment is stabilized by charge transfer from the Au substrate.

We now consider the effects of the Au substrate. First, we examine this effect on important *structural* features of the AuS monolayer. Although the combined system is incommensurate, it is possible to fit the AuS unit cell in a supercell of the Au(111) surface by using the equilibrium Au lattice constant predicted from calculations on bulk Au (c_{theory} = 2.948 Å) instead of the experimental value (c_{expt} = 2.884 Å). In this arrangement, the gray area in Fig. 1(a), which is commensurate with the Au lattice, has dimensions of (8.84×7.80) Å^2, which are still within experimental error bars for the AuS unit cell (7.80 Å is within the range of 7.8 Å to 8.6 Å for the 2nd lattice constant). We can now perform geometry optimizations for a periodic system with a supercell containing a AuS layer on top of a 6-layered Au(111) slab. In the most stable structure, which we call *B*, the 2-fold coordinated Au atom ($Au_{(2)}$) in AuS is at site **X** and the 4-fold coordinated

Au atom ($Au_{(4)}$) at **O** (Fig. 1). Initial structures with $Au_{(2)}$ positioned at any of the three-fold sites of the surface layer, also relaxed to structure *B*. If $Au_{(4)}$ is placed initially at **X** and $Au_{(2)}$ at **O**, each of these Au atoms remains at its initial site during geometry optimization. However, the remaining atoms completely rearrange to eventually yield the same structure (*B*), with the Au atom at site **X** becoming 2-fold coordinated, and that at **O** becoming 4-fold coordinated. This indicates that the AuS structure is favored and remarkably robust even in the presence of the Au substrate.

The incommensurate arrangement and long-range order of the AuS layer imply that the layer should feel an average effect of the substrate. This average effect is not altered as the relative position of the overlayer is varied. The calculations mentioned above are not useful in describing this effect because the forced matching of lattice constants between the overlayer and substrate introduces artificial corrugations for some atomic positions. Therefore, in analyzing the electronic features of the AuS layer, it is necessary to introduce a different approach to take into account the average effects of the substrate in the incommensurate system.

As the overlayer and substrate interact weakly with each other, and are both metallic, charge transfer is expected to be the dominant electronic effect of the substrate. The weak interaction with the substrate also suggests that the AuS atomic geometry and band structure will remain largely unchanged by the Au substrate, allowing us to use the structural features of the stable isolated layer A, and model charge transfer by changing the occupancy of the AuS bands (so-called 'rigid band model'). We model the change in occupancy by shifting the Fermi level (E_F) of *A* by an amount ΔE_F to that expected for the combined system.

To estimate ΔE_F, we first construct a series of models that are representative of the different relative positions that the incommensurate AuS layer can take on the Au(111) substrate. Next, we compute the average of the substrate-induced shifts in Fermi level at each of these positions. The models were constructed as follows. First, we relax atoms in the top 3 Au(111) layers of the 6-layer Au(111) slab, and atoms in the AuS layer, with the additional constraints that the AuS layer be planar, with $Au_{(2)}$ at **X** and $Au_{(4)}$ at **O**. The optimal height of the AuS layer above the Au surface is 2.53 Å, which is the same as the average height of the layer above the Au surface is in structure *B*. We call the resulting system *B'*. Next, we shift this AuS layer in steps by $\lambda \boldsymbol{a_2}$ relative to the substrate ($\lambda = 0.0, 0.1, \ldots, 0.9$). At each step, only the top 3 Au(111) layers are allowed to relax, resulting in systems which we call B_λ'.

We calculate the substrate-induced shift in Fermi level ΔE_F by taking the average over λ of the differences in work functions $\Delta\Phi$ between the metallic systems *A* and B_λ'. The work function of the systems are calculated using symmetric slabs, obtained by taking mirror images about the 3 frozen Au(111) layers, to give 9-layered Au slabs covered on both sides by AuS. The work function Φ is computed as $V_{vac}^{(c)} - E_F^{(c)}$, where $E_F^{(c)}$ and $V_{vac}^{(c)}$ are the Fermi level and vacuum potential in the calculation. As described below, this approach allows us to estimate the effects of charge transfer remarkably well.

5.1.5 Atomic structure: Results

The estimated E_F of the incommensurate AuS layer on Au(111) is found to be (0.85 ± 0.03) eV closer to the vacuum potential than E_F of *A*, corresponding to electronic charge transfer from Au(111) to *A*. This is consistent with the larger work function of *A*

(6.18 eV) relative to Au(111), which we calculate to be 5.18 eV, in reasonable agreement with the experimental value[19] of 5.31 eV.

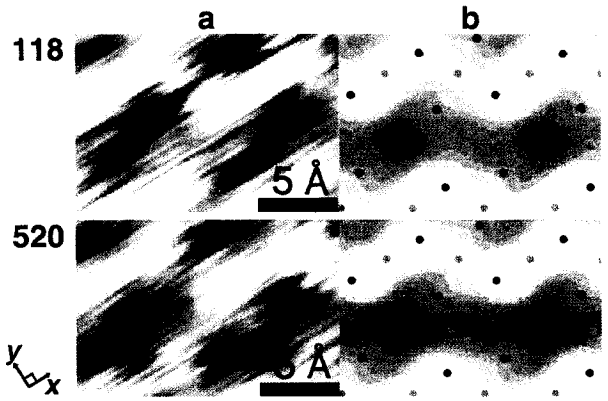

FIG. 2. (a) Constant height STM images collected at room temperature, (b) STM simulations. Orange and black circles mark lateral positions of Au and S atoms respectively. The numbers indicate sample bias voltages in mV, and the scan direction is given by ***x***.

We can now simulate STM images using *A* with $\Delta E_F = 0.85$eV, within the Tersoff-Hamann approximation.[20] To take into account the effect of convolution between sample and tip wave functions,[20] as well as the small amount of spot broadening in the scan direction ***x***, we use elliptical Gaussian broadening with standard deviations s_x of 1.2 Å and s_y of 0.8 Å (both less than half of the bond lengths in the structure). Our simulations reproduce convincingly the high-magnification experimental images at 2 different sample bias voltages (Fig. 2), and are insensitive to the exact values of s_x and s_y. The calculations indicate that the bright spots in the STM images in Fig. 2 are associated with positions of the $S_{(3,a)}$ and $S_{(3,b)}$ atoms. The angle between $S_{(3,b)}$–$Au_{(2)}$–$S_{(3,b)}$ and the a_1 axis (Fig. 1) is very robust in all the structures considered here (structure *A*: 31°, fully

relaxed neutral layer: 33°, fully relaxed charged layer: 29°, structure *B* (with substrate): 32°).

5.1.6 Nature of bonding: Approach

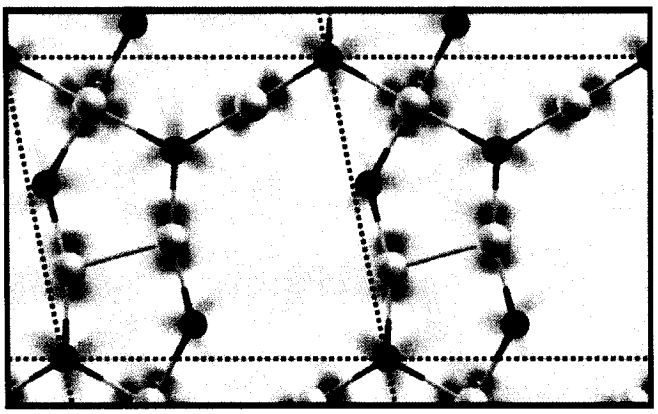

FIG. 3. Charge density difference plot. The charge density difference between structure *A* and the superposition of atomic densities, is plotted in the plane of the structure; the scale runs from -0.0005e (black) to +0.0002e (white).

The fact that Au atoms from terraces can be incorporated into a stable, incommensurate AuS layer is quite remarkable. This warrants a closer examination of bonding in the AuS layer. In Fig. 3, the charge density difference between structure *A* (Fig. 1(b)) and the superposition of atomic densities is plotted in the plane of the structure. From this plot, it is evident that charge accumulates between the Au and S atoms, seemingly closer to the S. A small amount of charge accumulation seems to be present between $Au_{(3,a)}$ and $Au_{(3,b)}$ as well. In order to obtain more detailed chemical insights than that provided by Fig. 3, we use a recently developed scheme[21] which provides an excellent description of bonding in well-characterized systems of both metallic and covalent nature. The analysis relies on the successive construction of two sets of localized Wannier orbitals with initially-specified centers and symmetries (e.g. atomic *s*,

p or *d* symmetries). The first set (I) consists of atom-centered orbitals (AOs), and the second (II) of both AOs and bond-centered orbitals (BOs).

The construction of Wannier orbitals suited for the current application is described in detail in Reference 21. Briefly, we make a choice of symmetry properties of Wannier functions specified with (a) the centre of the Wannier function and (b) the irreducible representation of its site symmetry group given in terms of its partner function, for example a spherical harmonic. Such a choice is typically guided by the symmetry properties of Bloch functions at high symmetry points in the Brillouin zone, and is self-corrective, as discussed below. Well-localized Wannier functions can be obtained if they are Fourier transformed from Bloch functions that are smooth and periodic in Bloch vector **k**. As described in Reference 21, these Bloch functions can in turn be obtained by introducing an *auxiliary subspace*. This *auxiliary subspace* is constructed from highly localized functions of the chosen symmetry (spherical harmonic for the angular part, and a Gaussian form for the radial part). These highly localized and orthonormal orbitals are Fourier transformed to obtain Bloch functions that span the auxiliary subspace. The key point is that these Bloch functions have the same symmetry properties as those of the Bloch functions in the *physical subspace* of occupied (and some of the unoccupied in metals) electronic states in the system. A unitary transformation is performed on the Bloch functions in the physical subspace such that the overlap matrix between Bloch states of the auxiliary and the physical subspace becomes hermitian, amounting to vanishing of open path non-abelian geometric phases. This gives the desired Bloch functions and corresponding well-localized Wannier functions. Determination of the unitary transformation is facilitated by singular value decomposition

of the overlap matrix. The scheme is self-corrective in the sense that some of the singular values vanish in the case where the choice of symmetry of the auxiliary subspace is not quite optimal and hints for correction.

5.1.6 Nature of bonding: Results

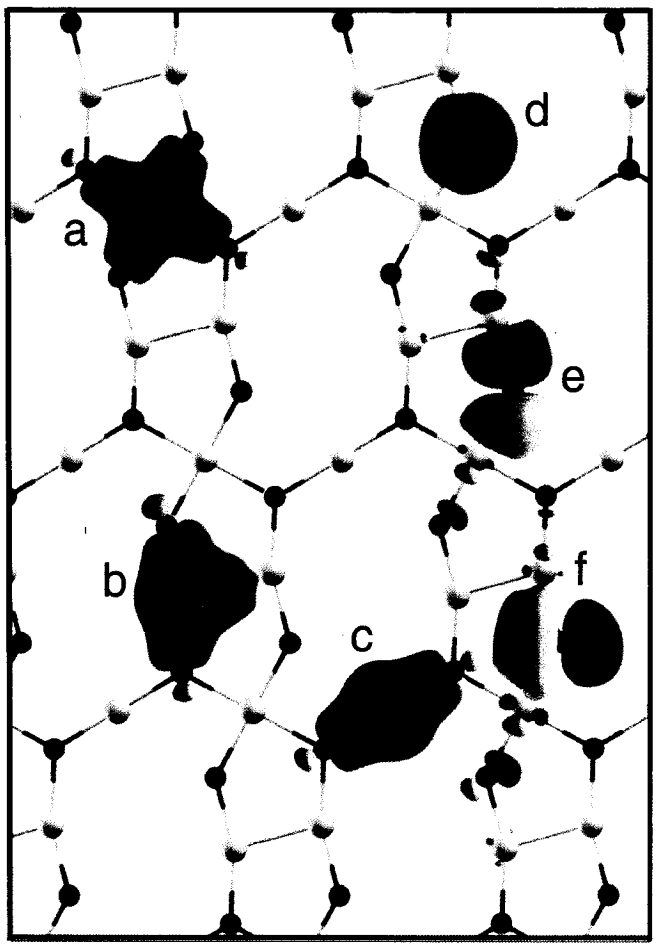

FIG. 4. AOs in *A*. 6*s* AOs for (a) $Au_{(4)}$, (b) $Au_{(3,a)}$ (similar to $Au_{(3,b)}$), (c) $Au_{(2)}$; and (d) 3*s*, (e) and (f) 3*p* AOs (in perpendicular directions) for $S_{(2,b)}$ (similar to other S atoms). Red and green surfaces represent positive and negative contour surfaces of the same absolute value.

We use here two choices of auxiliary subspaces: (I) one with only atom-centered orbitals (AOs), and (II) one with AOs and bond-centered orbitals (BOs), by including more unoccupied states in the physical subspace. We first illustrate the method by discussing results for the stable structure *A* (Fig. 1(b)). The AOs for Au 6*s* (Fig. 4(a-c)), S 3*s* (Fig. 4(d)) and S 3*p* (Fig. 4(e-f)) electrons are spatially extended, indicating that these electrons contribute substantially to bond covalency. In particular, the singular value for an Au-centered AO with *s*-symmetry vanishes, reflected in the distortion of these AOs from atomic-like *s* orbitals (Fig. 4(a-c)), in contrast to the S AOs that still resemble atomic-like *s* and *p* orbitals (Fig. 4(e-f)). This suggests an especially important role of Au 6*s* electrons in the covalency of bonds in the AuS layer. On the other hand, the Au 6*p* AOs are unoccupied and are especially localized, suggesting that the 6*p* orbitals of Au do not hybridize with 6*s* orbitals during bond formation. Au 5*d* AOs, although not spatially extended, are less localized that the 6*p* AOs, and as we discuss later, do contribute to bond formation. This is consistent with the general argument in the literature that electronegative ligands of Au support Au 5*d* participation in bond formation, while electropositive ligands support Au 6*p* participation:[22] the electronegativity of S (Au) is 2.58 (2.54). The lack of 6*s*-6*p* hybridization is also consistent with the relatively large energy separation between 6*s* and 6*p* levels compared to 6*s* and 5*d* levels in atomic Au.[23]

The amount of electron charge in Au AOs is largest for $Au_{(2)}$ and smallest for $Au_{(4)}$, consistent with formal oxidation states expected from the literature: Au^{III} and Au^{I} have square planar and linear coordination geometries respectively, while the $5d^9$ configuration in Au^{II} is typically accompanied by a Au-Au bond .[23] Indeed, the ring, $Au_{(4)}$-$S_{(3,b)}$-$Au_{(3,b)}$-$S_{(2,b)}$-$Au_{(4)}$-$S_{(3,a)}$-$Au_{(3,a)}$-$S_{(2,a)}$, is a motif found in Au^{2+} compounds.[18, 23]

S is known to form bonds with Au in all three oxidation states;[18] the 2- and 3-fold coordination for S is similar to that for O in Au_2O_3 [24] (the structure of Au_2S_3 is unknown). The 1:1 stoichiometry in structure *A* thus arises from having one $Au^{III}(Au_{(4)})$, one $Au^{I}(Au_{(2)})$ and two $Au^{II}(Au_{(3,a)}$ and $Au_{(3,b)})$ atoms per unit cell, in contrast to bulk gold sulfides (Au_2S and Au_2S_3)[16] which contain purely Au^{I} or Au^{III} respectively.

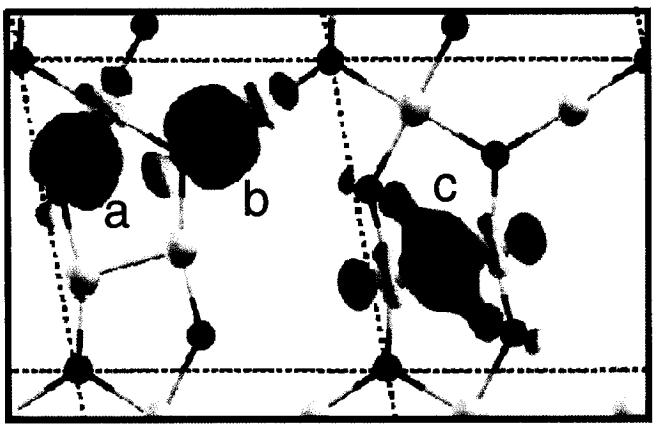

FIG. 5. BOs in *A*. (a) $Au_{(4)}$-S, (b) $Au_{(2)}$-S, (similar to $Au_{(3,a)}$-S and $Au_{(3,b)}$-S) and (c) $Au_{(3,a)}$-$Au_{(3,b)}$. Red and green surfaces represent positive and negative contour surfaces of the same absolute value.

Each Au (S) atom contributes 0.3-0.4 *e* (0.8-0.9 *e*) per bond. The Au-S bonds are partially polar, as indicated by their asymmetric BOs (Fig. 5). This is consistent with excess charge in S 3*p* AOs and shortage of charge in Au 6*s* (and some 5*d*) AOs. The origin of Au-Au interactions in Au^{II}-Au^{II} (and Au^{I}-Au^{I}) compounds has been the subject of considerable debate.[22] Previous ab initio studies have described the Au^{II}-Au^{II} interaction as a single covalent bond with considerable 6*s*-6*s* character.[22] Our calculations indicate that the 6s electrons indeed are key players in the Au-Au bond in the isolated AuS layer. We further predict that the Au-Au bond in isolated AuS is stabilized by

delocalization over $S_{(2,a)}$ and $S_{(2,b)}$, as indicated by the multi-centered $Au_{(3,a)}$-$Au_{(3,b)}$ BO in Fig. 5(c). In addition, the amount of charge in the $Au_{(3,a)}$-$Au_{(3,b)}$ BO is 20-27 % less than that in the Au-S BOs, indicating that the Au-Au bond strength in isolated AuS is weaker than other bonds in the layer.

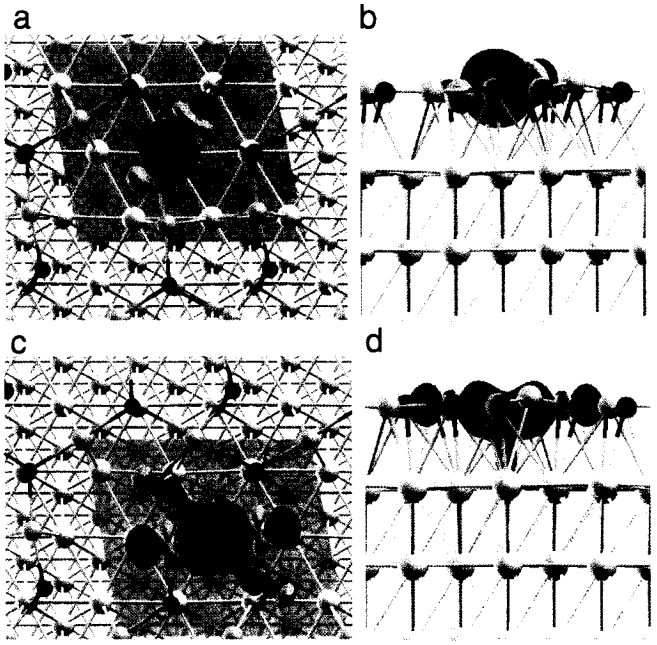

FIG. 6. BOs in *B*. $Au_{(2)}$-S in (a) top and (b) side views (similar for other Au-S bonds), and $Au_{(3,a)}$-$Au_{(3,b)}$ in (c) top and (d) side views. Red and green surfaces represent positive and negative contour surfaces of the same absolute value. The isocontour value in (c) is half that in (a), (b) and (d).

To understand the effects of the substrate, we perform a similar analysis on structure *B* ($Au_{(2)}$ at site **X** on Au(111) and $Au_{(4)}$ at **O** (Fig. 1)), with AOs centered on atoms in the AuS layer and the top Au(111) layer. The shapes of Au-S BOs are not affected by the substrate (Fig. 6(a-b)), while the multi-centered Au-Au BO, though slightly extended towards the substrate atoms, remains largely confined within the AuS

plane (Fig. 6(c-d)). The fact that BOs within the AuS layer largely retain their shapes even in the presence of the Au(111) layers suggests that the AuS layer does not interact strongly with the substrate, which is consistent with the experimentally observed incommensurability and our theoretical assumptions.

Compared to the isolated layer, the electronic charge in each BO increases by 54 % on average, except for the Au-Au BO, where the increase is 15 %. In contrast, the contribution of each AO to bonding either decreases, or increases by at most 9 %. This implies that bonds within the AuS layer are strengthened at the expense of substrate electrons, which may explain the robustness of the AuS structure. Using ΔE_F of 0.85 eV and the DOS of the isolated layer *A*, we estimate the quantity of charge transferred to the layer to be ~3.3 *e* per unit cell of *A*. Completely relaxing the isolated AuS layer in the presence of this extra charge does not change the atomic arrangements significantly (Fig. 7(b)). Importantly, however, the optimized lattice constants of the charged layer are 8.4 Å and 7.9 Å: these are near the low end but within the respective experimental ranges of [8.4 – 9.2] Å and [7.8 – 8.6] Å (see Table 1(a) for bond lengths). The lattice angle of 76° is also reasonably close to the experimental range of [78° – 86°]. These results are in contrast to what we found for the *neutral* AuS layer, where the optimized lattice constants were too small compared to experiment (Fig. 7(a)). This further confirms that charge transfer from the substrate stabilizes the stretched bonds in the supported layer, and that our estimated shift in E_F models the effect of charge transfer reasonably well.

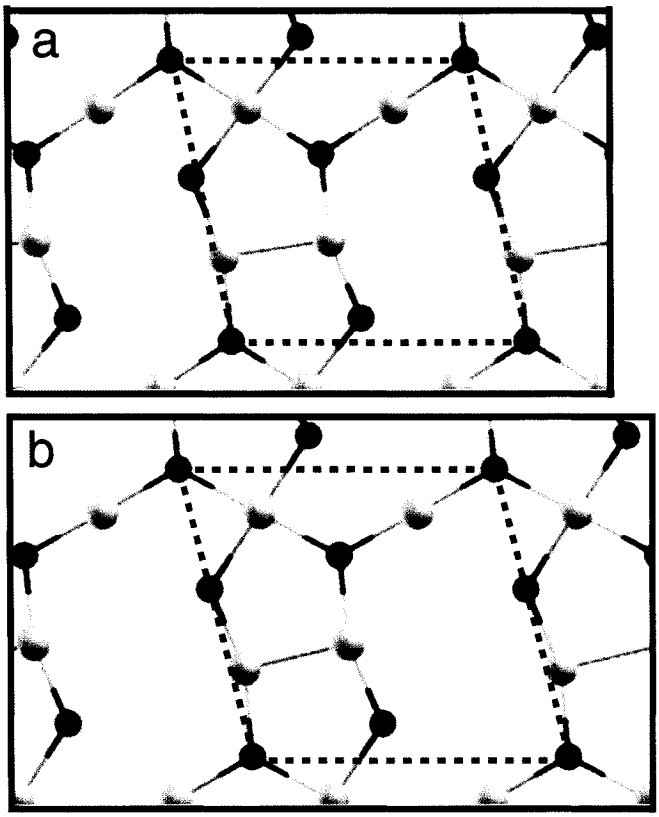

FIG. 7 Fully relaxed structures and unit cells (red boxes) for isolated, (a) neutral and (b) charged AuS layers. The structure in (b) has a charge of 3.3 *e*/cell.

5.1.7 Concluding remarks

As previously established in detailed scanning probe studies,[5, 6] the Au(111) surface interacts with deposited sulfur in a dynamic, rather than static, manner, eventually resulting in a 2D incommensurate Au-S phase upon annealing to 450 K. STM alone was insufficient to decipher the atomic structure of the Au-S phase, since STM images the electronic, rather than atomic, structure. In this work, we revisit the structure of this intriguing incommensurate phase, and propose an atomic-scale model for the system, which reproduces convincingly high-magnification STM images. What is striking about this model is that it is remarkably robust, even in the presence of the Au substrate.

Furthermore, the structure reflects the rich co-ordination chemistry of Au, which is also present in Au compounds synthesized from Au ions in solution or gas phase.[22, 23] We provide a natural explanation for the remarkable robustness of the model, in terms of charge transfer from the substrate, bond types and formal oxidation states of Au.

While we have not proven that the proposed model is the thermodynamically stable structure, the extraordinary robustness of the model and our bonding analysis indicate that it is strongly favored, and would therefore at least be an important precursor state. Together with STM studies, it is clear that the Au(111) surface is not simply an 'inert' surface, but can interact dynamically with deposited sulfur, with the incorporation of Au atoms from terrace sites into a sulfide adlayer at higher coverages. Our results suggest that the ring-like features reported in the literature[12-15] may not simply be S_8 molecules. Similar adsorbate-induced mobilization of Au atoms has been observed when oxygen atoms are deposited onto Au(111), resulting in a gold oxide adlayer.[6]

The dynamic nature of the Au(111) surface and the incorporation of Au terrace atoms into a sulfide adlayer in this system have important implications for the structure of the S-Au interface in self-assembled monolayers (SAMs) of thiols on Au(111),[3] which is crucial to determining their transport properties.[25-27] Similar etch pits and islands have been observed in these systems, suggesting that Au terrace atoms will have similar interaction chemistry with thiol chains. The interface structure in thiol/Au systems, however, has commonly been interpreted in terms of a flat Au(111) surface,[3] with only a few works[28, 29] proposing an interface structure involving Au vacancies. The latter involve *ab initio* calculations which indicate that the adsorption of methylthiolate on Au(111) is stabilized by the introduction of vacancies in the Au substrate, with the

increased adsorption energy more than compensating for the vacancy formation energy.[28, 29] Our observations are consistent with this picture and further highlight the importance of considering composite Au-thiol adlayer systems in contrast to conventionally assumed adsorption on flat Au(111).

Furthermore, we have introduced theoretical techniques to take into account charge transfer and thereby simulate STM images for an incommensurate system without requiring exceedingly large supercells. While more extensive tests of this approach using different incommensurate systems are, of course, required to truly prove its generality, we have also tested the approach on a known commensurate system, and suggest that in general, the shift in Fermi level can be obtained by comparing an experimentally determined work function of the combined incommensurate system with a quantitative theoretical estimate of the work function of the isolated adlayer (please see section 5.1.8). This suggests that it may be possible to perform computationally tractable first-principles studies of many incommensurate systems involving metallic adlayers on metal substrates. We have also employed state-of-the-art Wannier function-based methods to yield detailed chemical insights into the nature of bonding in the system, and this analysis is applicable to a wide range of complex systems.

5.1.8 Discussion of theoretical approach for simulating incommensurate system

We evaluate the generality of the 'rigid-band model' for modeling the effects of charge transfer in incommensurate systems with metallic (or semi-metallic) overlayers on metallic substrates, by testing the approach on a previously studied *commensurate* system, a semimetallic MoO_3 monolayer on Au(111).[30] Two key features that are of interest are: (i) whether the major peaks in the DOS for the isolated semimetallic oxide are shifted by

a fairly constant energy to corresponding major peaks in the PDOS of the oxide in the combined system, and (ii), whether this energy shift is given by the difference in work functions of the isolated oxide and that in the combined system. It is important to note that this approach does not apply for overlayers with a band gap, as their interaction with the substrate cannot be modeled by simple charge transfer effects.

We first compute the density of states (DOS) of the isolated oxide layer frozen in configuration from the combined system, which has no band gap (Fig. 8(a)). Next, we compute the projected density of states (PDOS) of the supported oxide layer, using a model of the oxide on the Au(111) substrate (represented by a 6-layered Au(111) slab), in a supercell corresponding to the repeat unit of the commensurate system (Fig. 8(b)). The major peaks in Fig. 8(b) can be obtained by shifting those in Fig. 8(a) by -0.5 to -0.8 eV (Table 2). These shifts in peak positions are within 0.1 to 0.2 eV of the calculated difference in work functions $\Delta\Phi$ between the combined system and the isolated oxide (-0.6 eV), thus showing that $\Delta\Phi$ captures the effects of charge transfer reasonably well. As we expect for commensurate systems, some hybridization occurs between orbitals of the overlayer and the substrate. Shifting the Fermi level in Fig. 8(a) by $\Delta\Phi$ therefore does not give the exact PDOS in Fig. 8(b). However, this is unlikely to be the case in *incommensurate* systems, where interactions between the overlayer and substrate are dominated by charge transfer, and bonding within the overlayer is much stronger than bonding with the substrate.

Therefore, it is likely that for incommensurate systems with metallic layers on metallic substrates, the PDOS of the supported layer can be obtained approximately by

shifting the Fermi level of the DOS of the isolated layer, by an amount given by the difference in work functions $\Delta\Phi$.

In the general case, $\Delta\Phi$ can be obtained by comparing an experimentally determined work function of the combined incommensurate system (eg. with photoemission) with a calculated work function of the isolated adlayer determined quantitatively using many-body perturbation techniques such as the G-W approximation.[31] In principle, DFT can give exact values of the work function of metal surfaces, but only if the exchange-correlation functional is exact.[32] On the other hand, the quality of the exchange-correlation functional can be assessed by comparing the computed work function with experiment. The PW-91 functional[8] used in this work resulted in theoretical work function values within 2.5 % of experiment for the Au(111) surface (Experiment: 5.31 eV,[19] Calculated: 5.18 eV). The use of DFT (PW-91) for calculating $\Delta\Phi$ for the AuS system is further justified by the fact that *relative* values of calculated work functions generally compare well with experiment when the same exchange-correlation functional is used.[19]

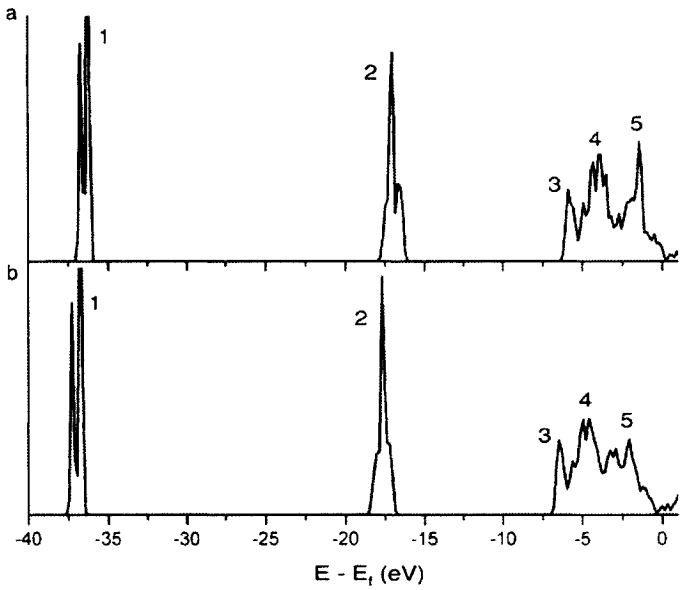

FIG 8. (a) DOS of MoO_3 alone (frozen in geometry from combined system), (b) PDOS of MOO_3 in combined system, MoO_3 on Au(111). Energies for the labeled peaks are given in Table 2.

Peak number	MoO_3 alone	MoO_3 in combined system
1	-36.25	-36.76 (-0.5)
2	-17.02	-17.71 (-0.7)
3	-5.90	-6.48 (-0.6)
4	-3.83	-4.61 (-0.8)
5	-1.44	-2.06 (-0.6)

TABLE 2. Energies of peaks in eV, relative to the Fermi level E_f in Fig. 8(a) (MoO_3 alone) and 8(b) (MoO_3 in combined system).

References

[1] G. Kresse, M. Schmid, E. Napetschnig, M. Shishkin, L. Kohler, and P. Varga, Science **308**, 1440 (2005).

[2] C. H. Ahn, K. M. Rabe, and J. M. Triscone, Science **303**, 488 (2004).

[3] J. C. Love, L. A. Estroff, J. K. Kriebel, R. G. Nuzzo, and G. M. Whitesides, Chem. Rev. **105**, 1103 (2005).

[4] C. T. Campbell, Surf. Sci. Rep. **27**, 1 (1997).

[5] M. M. Biener, J. Biener, and C. M. Friend, Langmuir **21**, 1668 (2005).

[6] B. K. Min, A. R. Alemozafar, M. M. Biener, J. Biener, and C. M. Friend, Topics in Catalysis **36**, 77 (2005).

[7] M. M. Biener, J. Biener, and C. M. Friend, Surf. Sci. **590**, L259 (2005).

[8] J. P. Perdew and Y. Wang, Phys. Rev. B **45**, 13244 (1992).

[9] P. E. Blochl, Phys. Rev. B **50**, 17953 (1994).

[10] E. Lundgren, G. Kresse, C. Klein, M. Borg, J. N. Andersen, M. De Santis, Y. Gauthier, C. Konvicka, M. Schmid, and P. Varga, Phys. Rev. Lett. **88**, 246103 (2002).

[11] T. Wiederholt, H. Brune, J. Wintterlin, R. J. Behm, and G. Ertl, Surf. Sci. **324**, 91 (1995).

[12] X. P. Gao, Y. Zhang, and M. J. Weaver, J. Phys. Chem. **96**, 4156 (1992).

[13] C. Vericat, G. Andreasen, M. E. Vela, and R. C. Salvarezza, J. Phys. Chem. B **104**, 302 (2000).

[14] C. Vericat, M. E. Vela, G. Andreasen, R. C. Salvarezza, L. Vazquez, and J. A. Martin-Gago, Langmuir **17**, 4919 (2001).

[15] C. Vericat, M. E. Vela, G. A. Andreasen, R. C. Salvarezza, F. Borgatti, R. Felici, T. L. Lee, F. Renner, J. Zegenhagen, and J. A. Martin-Gago, Phys. Rev. Lett. **90**, 075506 (2003).

[16] J. C. Bailar, H. J. Emeleus, R. Nyholm, and A. F. Trotman-Dickenson, *Comprehensive inorganic chemistry* (Pergamon Press, 1973).

[17] K. Ishikawa, T. Isonaga, S. Wakita, and Y. Suzuki, Solid State Ionics **79**, 60 (1995).

[18] H. Schmidbaur, *Gold: progress in chemistry, biochemistry and technology* (John Wiley & Sons, 1999).

[19] S. Hufner, *Photoelectron Spectroscopy: Principles and Applications* (Springer-Verlag, Berlin Hiedelberg, 2003).

[20] J. Tersoff and D. R. Hamann, Phys. Rev. Lett. **50**, 1998 (1983).

[21] J. Bhattacharjee and U. V. Waghmare, Phys. Rev. B **73**, 121102 (R) (2006).

[22] P. Pyykko, Angew. Chem. Int. Edit. **43**, 4412 (2004).

[23] R. J. Puddephatt, *The Chemistry of Gold* (Elsevier, 1978).

[24] P. G. Jones, H. Rumpel, E. Schwarzmann, G. M. Sheldrick, and H. Paulus, Acta Crystallogr. B **35**, 1435 (1979).

[25] G. K. Ramachandran, T. J. Hopson, A. M. Rawlett, L. A. Nagahara, A. Primak, and S. M. Lindsay, Science **300**, 1413 (2003).

[26] E. G. Emberly and G. Kirczenow, Phys. Rev. Lett. **91**, 188301 (2003).

[27] Z. Hens, D. V. Tallapin, H. Weller, and D. Vanmaekelbergh, Appl. Phys. Lett. **81**, 4245 (2002).

[28] L. M. Molina and B. Hammer, Chem. Phys. Lett. **360**, 264 (2002).

[29] Y. Morikawa, C. C. Liew, and H. Nozoye, Surf. Sci. **514**, 389 (2002).

[30] S. Y. Quek, M. M. Biener, J. Biener, C. M. Friend, and E. Kaxiras, Surf. Sci. **577**, L71 (2005).

[31] M. S. Hybertsen and S. G. Louie, Phys. Rev. B **34**, 5390 (1986).

[32] R. M. Martin, *Electronic Structure: Basic Theory and Practical Methods* (Cambridge University Press, Cambridge, United Kingdom, 2004).

Chapter 6

Organic molecules on Si(001):

Implications for negative differential resistance

6.1 First-principles studies of the electronic structure of cyclopentene on Si(001): Density functional theory and GW calculations

The electronic structure and ground-state geometry of cyclopentene monolayers on Si(001) are studied using ab initio pseudopotential density-functional theory (DFT). Quasiparticle excitation spectra are calculated within the GW approximation. Both cis and trans cyclopentene monolayers are considered. In both geometries, a strong electronic coupling between the monolayer and Si substrate is found; substantial inter-molecular interactions are present, as indicated by broadening in molecular levels that are decoupled from the substrate. It is argued that the cis structure is kinetically favored, and we evaluate self-energy corrections to the eigenstates of this configuration near the band edges within the GW approximation. The calculated self-energy corrections are large, exceeding those of bulk Si, and increase the energy gap between occupied and unoccupied frontier adsorbate states by 1.3 eV.

This work has been published as an article in Physica Status Solidi (b):
S. Y. Quek, J. B. Neaton, M. S. Hybertsen, E. Kaxiras and S. G. Louie Physica Status Solidi (b) **243**, 2048-2053 (2006).

6.1.1 Introduction

Hybrid organic/silicon devices have attracted considerable attention of late because of their potential use in a variety of electronic applications.[1-4] Several recent

experimental studies have reported the fabrication and characterization of ordered, self-assembled monolayers of organics on Si(001).[5-7] The homogeneous structure of these monolayer-thin organic films, as well as their ability to form strong covalent bonds with the underlying Si substrate, make them extremely promising for integration with silicon microelectronics technology. Central to the ultimate realization of organic/silicon devices, of course, is the ability to understand and control the nature of electronic coupling between the organic layer and silicon substrate. Of particular importance is the impact of the substrate on electronic states in the organic layer, as governed, for example, by the local surface chemistry associated with the system. In this work, we perform first-principles calculations to explore the atomic and electronic structure of cyclopentene monolayers on Si(001), prototypical ordered organic/silicon systems.

The clean Si(001) surface is characterized by ordered rows of Si dimers, which provide an ideal template for the growth of ordered molecular layers. Scanning tunneling microscopy and infrared vibrational spectroscopy have shown that cyclopentene (C_5H_8) can form monolayers on Si(001), with each molecule oriented along a single Si dimer. This orientation is consistent with a so-called [2+2] cycloaddition mechanism for alkenes on Si(001), where the alkene π electrons and Si(001) dimer lone pair of electrons rearrange, resulting in the breaking the π bond breaks in exchange for two new σ C-Si bonds. The atomic structure of an ordered cyclopentene monolayer (ML) on Si(001) has also been thoroughly examined with density functional theory (DFT).[8-10] The structural geometries reported in these previous DFT studies are consistent with experimental observations.[6] The so-called *cis* structure, with H atoms closest to Si residing on the same side of C_5H_8, is most commonly studied,[6, 8-10] although an alternative *trans* structure (H

atoms on opposite sides of C_5H_8) has also been proposed theoretically.[10] In the following, we shall discuss the atomic and electronic structure of these two geometries, with specific focus on the local surface electronic structure in a range of energies near the Si band edges.

6.1.2 Methods

To examine the geometry and electronic structure of cyclopentene monolayers on Si(001), we perform calculations within two levels of theory. First, DFT calculations are used to optimize the geometry and provide some qualitative insight into the surface electronic structure. Next, we compute quasiparticle excitation energies, using the DFT Kohn-Sham eigenstates to construct the self-energy operator within the GW approximation.[11, 12] Here G is the electron Green's function and W is the dynamically screened Coulomb interaction. This many-body approach allows treatment of the molecule and substrate at the same level of theory. Previous work involving an ethylene monolayer on Si(001) obtained an electronic spectrum within the GW approximation in quantitative agreement with photoemission experiments.[13]

The ground-state DFT calculations are performed using two different plane-wave pseudopotential implementations, the VASP[14] and PARATEC[15, 16] codes; excellent agreement is obtained between the two codes. In VASP, we use the projected augmented wave method[17] with an energy cutoff of 29 Ry. Norm-conserving Troullier-Martins pseudopotentials[18] are employed in PARATEC, with an energy cutoff of 50 Ry. Reciprocal space is sampled with a Monkhorst-Pack k-point mesh of $2 \times 4 \times 1$ per unit supercell. The local density approximation (LDA) for the exchange-correlation functional is employed. We find that LDA gave comparable results with the generalized gradient

approximation (GGA), as parametrized by Perdew-Burke-Ernzerhof, for atomic structures and relative energetics between the *cis* and *trans* structures (Table 1). We simulate the Si(001) surface using a slab of 6 Si layers terminated by H atoms on the bottom side, and Si surface dimers on the top. Doubling the slab thickness to 12 Si layers does not change the atomic structure or binding energies significantly (Table 1). In each case, the theoretical lattice constant for Si (VASP LDA: 5.40 Å, PARATEC LDA: 5.39 Å) is used, and the bottom 2 Si layers are fixed to their bulk positions. All other atoms are allowed to relax until their forces are < 0.01 eV/Å. At least 13 Å of vacuum is used between Si slabs.

The details of our GW calculations are described elsewhere.[11, 12] An energy cutoff of 50 Ry and a *k*-point mesh of 2 × 4 × 1 are used to obtain the DFT-LDA wavefunctions and energies. A vacuum region of 19.4 Å is kept between Si slabs, corresponding to a closest distance of 13.4 Å between the H atoms terminating the bottom of the Si slabs and molecular atoms on adjacent slabs. A total of 770 conduction bands (with energies of up to ~51 eV above the Si valence band maximum) are included in the evaluation of the self-energy. The dielectric matrices are expanded in reciprocal space up to an energy cutoff of 9 Ry. Increasing the energy cutoffs or number of conduction bands does not change the quasiparticle energies by more than 0.1 eV. The GW parameters for bulk Si are converged to a level of accuracy consistent with the slab calculations.

6.1.3 Results and Discussion

As shown in Table 1, the binding energies we obtain compare well with those from other plane-wave calculations,[8, 9] although they differ from Ref. 10, possibly due to

a difference in basis set. The LDA binding energies are significantly larger than the GGA values (in agreement with Ref. 10), due to the tendency of the LDA to overbind.

		cis	*trans*
PARATEC	**LDA**	**2.07**	-
VASP	**LDA**	**2.14** **(2.11)**	**2.13** **(2.10)**
Ref. 10	LDA	1.4	1.6
VASP	**GGA**	**1.22** **(1.19)**	**1.22** **(1.20)**
Ref. 8	GGA	1.17	-
Ref. 9	GGA	1.05	0.94
Ref. 10	GGA	0.6	0.8

TAB LE 1. Binding energy (eV/molecule) of 1ML C_5H_8 on Si(001). Our results, in bold, are obtained using Si slabs with 6 Si layers, except for values in brackets which use 12 Si layers.

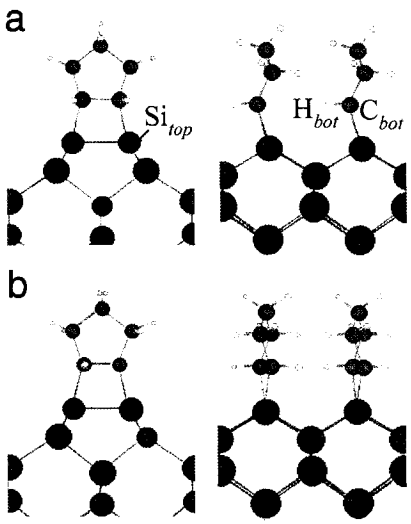

FIG. 1. Atomic structure of 1ML C_5H_8 on Si(001) in (a) *cis* and (b) *trans* configurations. The left and right panels provide two different views, down and perpendicular to the Si(001) dimer rows respectively. In each case, only 4 Si layers are shown.

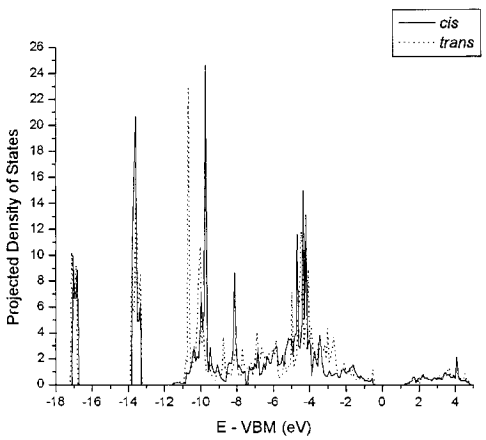

FIG. 2. LDA DOS projected onto spherical harmonics in spheres centered on C (radii 0.86 Å) and H (radii 0.37 Å) in the molecule, summed over *s*, *p* and *d*.

In Fig. 1, we show views of relaxed geometries for full (1ML) coverage with C_5H_8 in (a) *cis* and (b) *trans* configurations. These structures have very similar total energies (Table 1). Fig. 2 shows a comparison of the partial densities of states (DOS) of the two structures, computed from LDA Kohn-Sham eigenvalues and projected onto spherical harmonics in spheres centered on C (radii 0.86 Å) and H (radii 0.37 Å). The partial DOS plots are obtained using the tetrahedron method with a Brillouin Zone *k*-point sampling of $4 \times 8 \times 1$ (16 irreducible *k*-points). Energies are referenced relative to the bulk Si valence band maximum (VBM), obtained by aligning the average local potential in the middle of the Si slabs with that of bulk Si. The partial DOS indicate that the electronic spectra of the molecular layers in both structures are far from discrete, with significant dispersion for energies above -12 eV. This is consistent with a strong electronic coupling of the molecule to the substrate, which we expect from the covalent C-Si bonds and strained interface geometry. (The angle between bonds, C_{bot}-Si_{top} and Si_{top}-Si_{top}, is 78°, in contrast to bond angles of ~109° in unstrained tetrahedral sp^3 coordination for the Si atom.) The Si valence bandwidth is 12 eV, suggesting that the molecular states with energies above -12 eV are resonant with the propagating states in the Si substrate. Examination of the surface projected band structure confirms this picture, indicating very few gaps and strong electronic coupling to the substrate for most states. However, the relatively sharp peaks in the DOS at -13.6 and -16.9 eV are molecular states essentially decoupled from Si; the dispersion of 0.4-0.6 eV observed for these states is owing to significant intermolecular interactions within the monolayer. Although the DOS for these decoupled molecular states are similar for both *cis* and *trans* structures, detailed differences are visible between both geometries above -12 eV,

indicating that the electronic structure closer to the VBM is more sensitive to the details of atomic structure.

Although the *cis* and *trans* structures have similar total energies, the *cis* configuration is kinetically favored because of the symmetry of the frontier orbitals and the ring shape of the molecule.[9] Furthermore, the *cis* arrangement is computed to be about 0.4 eV more stable than *trans* at 0.5 ML coverage. This suggests that a 1ML *trans* structure can form only if *cis* transforms to *trans* with increasing coverage, a process that involves breaking of C-Si bonds and thus is likely to be kinetically hindered. For these reasons, we shall focus the remainder of our discussion on the *cis* structure. In particular, we shall examine results of quasiparticle calculations within the GW approximation for this geometry. We focus on states with energies within 3 eV of the VBM, as states outside this energy window are less important for transport and optical spectroscopic properties. Unlike the DFT Kohn-Sham eigenvalues, our calculated quasiparticle energies take electron correlation into account directly through the self-energy operator and provide quantitative spectral information within this energy window.

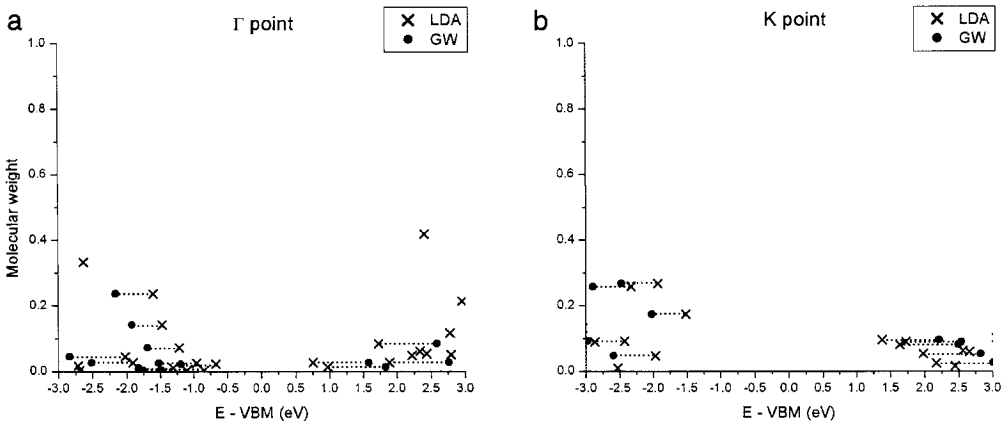

FIG. 3. Calculated molecular weights of eigenstates as a function of LDA and GW energy levels, at high symmetry points (a) Γ and (b) K in the Brillouin Zone. The zero of energy, 'VBM', corresponds to the LDA value of the Si VBM for the LDA plots, and the GW value for the GW plots. As a guide, dotted lines are used to join GW (dots) and LDA (crosses) data-points that correspond to the same eigenstates.

Fig. 3 shows the molecular weights of eigenstates near the band edges, as a function of their LDA Kohn-Sham energies and GW quasiparticle energies, for two high symmetry points in the Brillouin Zone, Γ and K. The LDA energies are referenced relative to the LDA value of the Si VBM, and the GW energies relative to the GW values of the Si VBM. The molecular weight is defined here as the integral of the square of the wavefunction over a spatial region containing the molecular layer; unity weight indicates the wavefunction is completely localized within the chosen region. The spatial region considered here is parallel to the Si surface plane, and extends from 1 Å above the molecule down to a height mid-way between the plane of C_{bot}'s and Si_{top}'s (following the nomenclature defined in Fig. 1). Importantly, the molecular weights in Fig. 3 are all < 0.5; in contrast, molecular weights of > 0.9 were computed for some eigenstates that lie

outside this energy window. This reflects the fact that the states within this energy window ([-3, 3] eV relative to the Si VBM) extend into the bulk and are not well localized on the molecular layer; their small molecular weights are associated with the C_{bot}-Si_{top} bonds, and in some cases with C_{bot}-H_{bot} as well. We shall refer to these states as frontier adsorbate states.

The energy levels of the adsorbate states relative to the Si band edges are experimentally relevant quantities, since the Fermi level of degenerately-doped Si can be aligned with either the VBM or CBM depending on whether the dopants are *p*- or *n*-type, respectively. Our calculations show that, in contrast to the clean (2 × 1)-reconstructed Si(001) surface,[19] the 1ML C_5H_8/Si(001) system has no surface or adsorbate states in the band gap of bulk Si. This is consistent with the saturation of dangling bonds associated with the bare Si(001) surface dimers, resulting from cyclopentene adsorption.

The self-energy corrections we compute near the band edges are significant. The occupied adsorbate states are shifted -0.5 to -0.6 eV away from the Si VBM (accounting for the self-energy correction for VBM in bulk Si, as in Fig. 3). Similarly, unoccupied adsorbate states are shifted +0.8 to +0.9 eV further above the Si VBM. The self-energy correction in 1ML C_5H_8/Si(001) thus increases the energy gap between the occupied and unoccupied frontier adsorbate states substantially, by about 1.3 eV. These corrections we compute here are larger than those calculated for the surface dimer states on clean (2 × 1)-reconstructed Si(001), which were reported to be between -0.10 eV to +0.15 eV for the occupied dimer state, and between +0.35 eV to +0.50 eV for the unoccupied dimer state.[19] We also obtain energy shifts relative to the Si CBM, which requires computation of the self-energy correction for the Si CBM as well. We find that corrections to the Si

VBM and CBM cause the fundamental gap of bulk Si to increase by 0.7 eV, from its LDA value of 0.5 eV to 1.2 eV, the latter being in excellent agreement with experiment.[12] As a result, the frontier unoccupied adsorbate states are shifted by +0.1 to +0.2 eV away from the Si CBM.

Because of the strong electronic coupling between the molecular monolayer and Si substrate, it is difficult to associate specific energies with the frontier adsorbate states. For simplicity, we define the highest-occupied frontier adsorbate state as the highest-occupied state with a molecular weight of more than 0.2 (first peak below the Si VBM in Fig. 3). This has a quasiparticle energy of -2.2 eV at the Γ point (Fig. 3(a)) and -2.5 eV at the K point (Fig. 3(b)) (relative to the Si VBM). Although there are no evident peaks above the CBM for the quasiparticle states in Fig. 3, we find that those unoccupied states with molecular weights of ~0.1 are partially localized on H_{bot}-C_{bot}-Si_{top}. The lowest-unoccupied state of this nature has a quasiparticle energy that is 1.4 eV above the CBM at the Γ point, and 1.0 eV above the CBM at the K point.

6.1.4 Conclusion

In conclusion, we have studied the atomic and electronic structure of ordered monolayers of cyclopentene on Si(001). Our results show that the cyclopentene monolayers exhibit strong electronic coupling to the Si substrate, and the projected densities of states close to the Si VBM are sensitive to the details of atomic structure. We argue that cyclopentene binds to Si dimers in a *cis* configuration. We have further analyzed the electronic structure of the *cis* structure by calculating its quasiparticle energy spectrum within the GW approximation. The resulting self-energy corrections enhance the gap between occupied and unoccupied frontier adsorbate states by about 1.3

eV. The GW calculations reported here allow a quantitative description of the energies of the frontier adsorbate states, which can be compared directly with experiments.

6.2 First-principles studies of level alignment in organic molecules on Si(001): Implications for negative differential resistance

Recent studies have proposed that negative differential resistance (NDR) can arise in silicon-based molecular systems due to field-induced movement of molecular levels into the Si band gap. We examine the electronic structure of cyclopentene on Si(001) as a function of electric field, using both density functional theory and a many-electron GW approach. The cyclopentene levels within 2.5 eV of the Si valence band maximum are found to be largely independent of field, suggesting that recent reports of NDR from cyclopentene on p-type Si cannot be explained by the above mechanism, as previously proposed. However, modifying the molecule to include N lone pairs, in the form of amino-cyclopentene or pyrroline, results in levels that may give rise to NDR for sufficiently strong fields.

6.2.1 Introduction

Organic molecular systems have recently emerged as especially promising alternatives for active elements in electronic, optoelectronic, and electromechanical devices.[1-4] In particular, nanostructured hybrid organic/silicon interfaces are now attracting considerable attention, and several recent experimental studies have reported the fabrication and characterization of ordered, self-assembled monolayers of organics on Si(001).[5-7] The homogeneous structure of these monolayer-thin organic films, as well as their ability to form strong covalent bonds with the underlying Si substrate, make them extremely promising for both fundamental studies and device applications. Moreover, remarkable progress has been made of late in achieving atomic-scale control and characterization of organic molecules on silicon substrates with scanning-probe

techniques,[2, 4-7, 20, 21] and this capability has provided the means for some of the most detailed studies of electronic transport and finite-bias single-molecule conduction to date. Recent scanning tunneling microscopy (STM) studies of individual cyclopentene molecules on p-type Si(001), a prototypical organic-silicon system, reported negative differential resistance (NDR) above a critical applied field of about 0.37 V/Å,[22] observations strikingly consistent with a resonant tunneling model[23] proposed prior to the experiments. The existence of a critical field, and also the absence of hysteresis in the reported measurements, suggest that the sharp peaks in the I-V characteristics originate from intrinsic molecular states and that molecular desorption, which has been observed at room temperature on n-type substrates,[24] is unlikely to be responsible for NDR in these low temperature experiments.

Prior to these experiments, Rakshit *et al* [23] suggested that a semiconductor-molecule-metal junction could behave as a resonant tunneling diode. In this seminal work, it was argued that with increasing bias voltage, a molecular orbital energy level could be driven across a p-type semiconductor band edge by a positive semiconductor bias, provided there is a non-negligible voltage drop across the molecule that modifies its orbital energy relative to the semiconductor valence band. Initially, the molecular energy level, positioned ΔE below the Fermi energy E_F, does not contribute to the current (Fig. 4a). (For degenerately p-doped Si, E_F is aligned with the impurity band which forms close to the VBM: the impurity level of B in Si(001) is 0.046 eV above the Si VBM.)[25, 26] However, as the bias increases, the level moves upward, relative to the silicon band edge, and eventually becomes resonant with E_F, resulting in a sharp increase in current associated with the opening of an elastic channel in the bias window (Fig. 4b). For even

larger biases, the level is lifted up into the band gap and a reduction in current will occur, resulting in NDR (Fig. 4c). A particularly appealing feature of this mechanism is that it is tied to the intrinsic levels of the molecule, suggesting the potential to tailor transport device properties at the molecular level and to obtain spectroscopic information from current-voltage measurements.

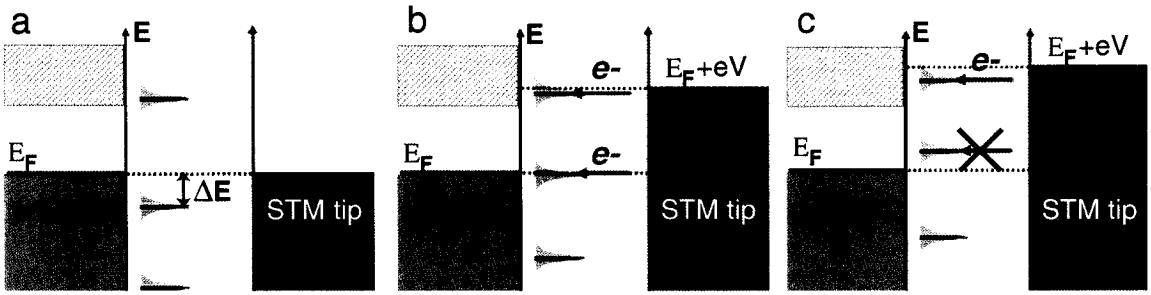

FIG 4. Schematic depiction of resonant tunneling mechanism for NDR. (a) zero bias level alignment, (b) molecular level at resonance with Fermi level E_F of p-type Si(001) (V ↑, I ↑), (c) molecular level driven into Si band gap (V ↑, I ↓).

To assess whether a resonant tunneling mechanism is appropriate to explain the NDR observed in cyclopentene on p-type Si(001), it is necessary to determine whether the molecular levels aligned near the VBM can be driven into the band gap. Previous work examined this concept for an adsorbed molecule on Si(001) using a nonequilibrium Green's function approach in which the Si was treated semi-empirically and the molecule with density functional theory (DFT).[27] Both ΔE and its evolution as a function of applied field were treated as adjustable parameters.[27] However, a quantitative assessment of these parameters is hampered by the inherent inaccuracies of Kohn-Sham eigenstates in DFT[28] and computational difficulties associated with treating the leads and molecule at the same level of theory.[27] Furthermore, substrate-induced polarization effects (not captured in

DFT) can reduce the molecular HOMO-LUMO gaps from their gas phase values by several eVs,[29] so that level alignments of molecules on substrates *cannot* be estimated from gas phase molecular levels. Experimental access to these properties has also been limited. For example, photoemission spectroscopy of cyclopentene monolayers on Si(001) were unable to resolve the states near the Fermi level or provide information on the nature of electronic coupling in the system.[30]

In this work, we use a parameter-free first-principles approach to compute the level alignment and electronic coupling of frontier orbitals in cyclopentene and related molecules on Si(001). The position of cyclopentene molecular levels, relative to the Si VBM, is computed as a function of electric field applied normal to the silicon surface, treating the molecule and substrate at the same level of theory. The equilibrium alignment is also computed with many-electron perturbation theory in the GW approximation. The results of our calculations are used to assess the impact of these factors on nanoscale transport properties. In particular, through a quantitative study of the level alignment of frontier molecular orbitals and their response to electric fields, we elucidate the conditions under which molecular levels can be driven across the band gap of Si, a necessary condition for the occurrence of NDR via the resonant tunneling mechanism.[23]

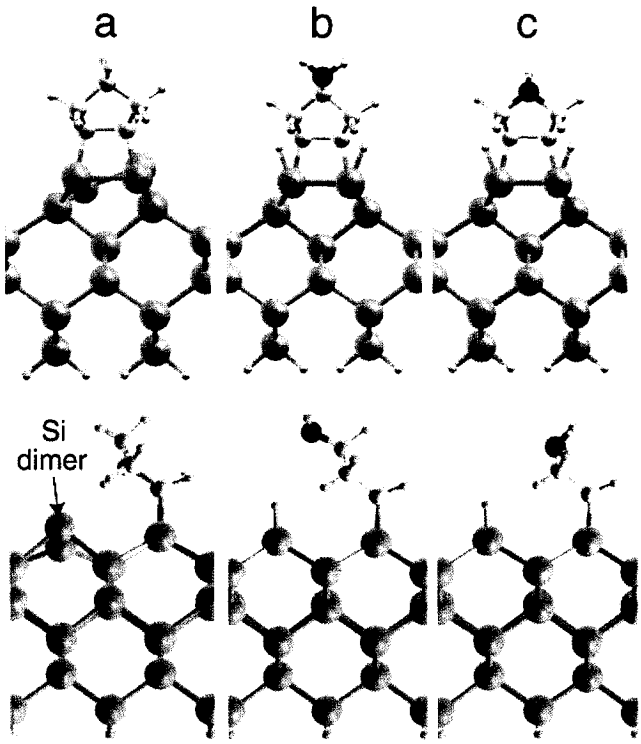

FIG 5. Atomic structure of 0.5 ML (a) C_5H_8 on clean Si(001), (b) amino-C_5H_8 on H-terminated Si(001), and (c) pyrroline on H-terminated Si(001). Top and bottom panels give views along and perpendicular to the Si(001) dimer rows. Orange, green, light blue and dark blue circles represent Si, C, H and N respectively. The bottoms of the Si slabs are terminated by H atoms.

Three systems are considered in this work: (a) cyclopentene on clean Si(001) (Fig. 5a); (b) amino-cyclopentene (Fig. 5b); and (c) pyrroline on H-terminated Si(001) (Fig. 5c). We find that the NDR reported in cyclopentene on p-type Si(001) is unlikely to result from resonant tunneling through intrinsic molecular states as previously proposed;[22] the frontier states in the system are too strongly coupled to the substrate. However, by introducing N lone pairs, as in amino-cyclopentene and pyrroline, this coupling is weakened, allowing the frontier molecular states to be driven into the Si band gap by

applied electric fields. The choice of clean (hydrogen-free) or H-terminated Si substrates is made to best relate to experiment; we find that this choice has no effect on our conclusions.

6.2.2 Summary of Methods

Our DFT calculations are performed in the plane-wave pseudopotential framework within the local density approximation (LDA), as implemented in VASP.[14] All geometries are optimized to a force convergence criterion of < 0.01 eV/Å. Quasiparticle excitation energies are computed perturbatively, using the DFT Kohn-Sham eigenstates to construct the self-energy operator within the GW approximation.[11, 12] For reference, we compute a value of 1.2 eV for the fundamental (indirect) gap of bulk Si with GW, in excellent agreement with experiment; in contrast, the corresponding LDA value is 0.5 eV, which is consistent with previous work.[12] In addition, we note that the GW approximation has already been applied to a related system, a single ethylene monolayer (ML) on Si(001),[13] where calculated quasiparticle spectra were in excellent agreement with photoemission experiments. Further details of the GW calculations can be found in Section 6.1.2.

The Si substrate is modeled using a 6-layer slab with lateral translational symmetry, passivated by H at the bottom and separated from adjacent slabs by at least 13 Å of vacuum. All energy levels are referenced relative to the Si VBM, which is obtained by aligning the average potential in the Si slab with that in bulk Si. To simulate finite bias conditions, we neglect the small potential drop across the Si slab, which would be absent for the doped substrate within a screening length of the surface (the experimental carrier density[27] of 4×10^{19}cm^{-3} corresponds to a Thomas-Fermi screening length of 2 Å or 1.5

Si(001) layers). By direct calculation, we find that increasing the slab thickness to 12 layers does not change the atomic and electronic structure of the adsorbed molecule.

An explicit calculation of I-V characteristics is beyond the scope of the present work, an acceptable approximation given that the experiments are in the tunneling regime (currents of a few nA and conductances of $\sim 10^{-5}$ G_0)[22]. Further details of our computational approach are provided in Section 6.3.2.

6.2.3 Cyclopentene on clean Si(001)

The clean Si(001) surface, which exhibits a reconstruction involving ordered rows of Si dimers, provides an ideal template for the growth of ordered monolayers and submonolayers of organic molecules. A prototypical organic-Si system is that of cyclopentene (C_5H_8) on Si(001), which has been well-characterized by STM and infrared vibrational spectroscopy.[2, 5-7, 21] Together with DFT studies,[8-10] it has been established that the π bond in C_5H_8 breaks to form two σ C-Si bonds with the Si dimer atoms (Fig. 5a), a geometry consistent with a cycloaddition mechanism. The so-called *cis* structure, with H atoms closest to Si residing on the same side of the molecule, is both kinetically and thermodynamically favored for coverages ≤ 0.5 ML (Section 6.1).

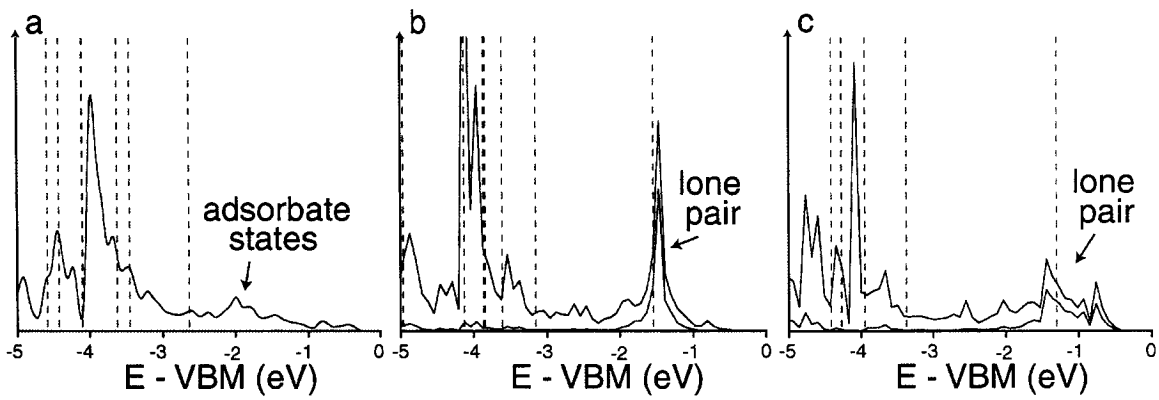

FIG 6. LDA PDOS for 0.5 ML (a) C_5H_8 on clean Si(001), (b) amino-C_5H_8 on H-terminated Si(001), and (c) pyrroline on H-terminated Si(001). Black curves denote DOS projected onto spherical harmonics in spheres centered on C (radii 0.86 Å), H (radii 0.37 Å) and (for (b) and (c)) N (radii 0.74 Å) atoms in the molecule, summed over *s*, *p* and *d*. Red curves denote DOS projected onto the spheres centered at N. Dotted blue lines mark the levels for the molecule with two extra H atoms, placed 1.1 Å from C along the C-Si bond, and frozen in geometry from the combined system. Further details can be found in Fig. 7 below.

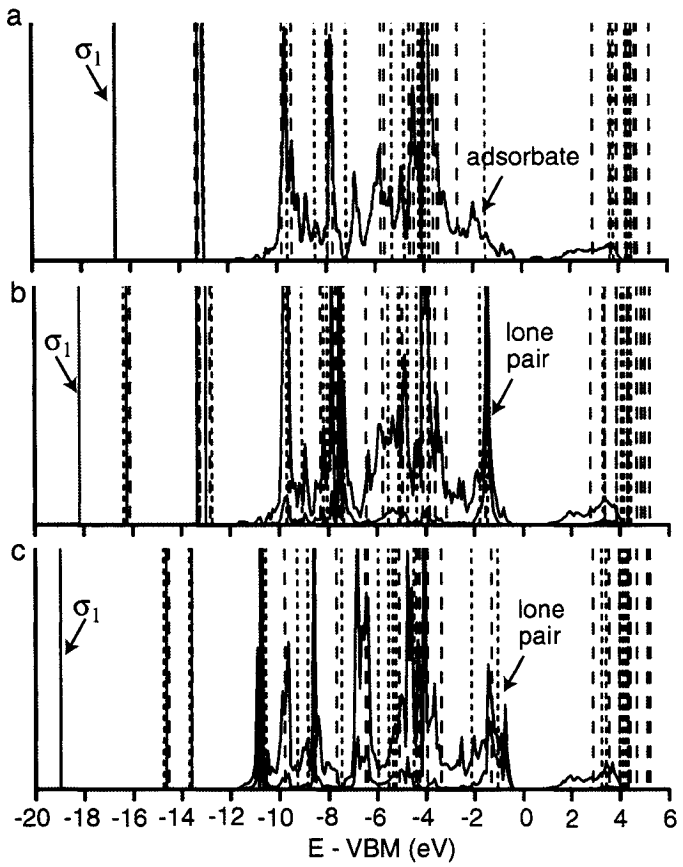

FIG 7. LDA PDOS for 0.5 ML (a) C_5H_8 on clean Si(001), (b) amino-C_5H_8 on H-terminated Si(001), and (c) pyrroline on H-terminated Si(001) (details). Black and red solid curves denote molecular and N PDOS as in Fig. 6. Dotted blue lines mark the same levels as in Fig. 6, while dotted brown lines mark the Kohn-Sham eigenlevels of the isolated, relaxed molecule in each case, aligned using the σ_1 state.

We first examine the electronic structure of the Si-adsorbate system, as reflected by the Kohn-Sham eigenvalues, at 0.5 ML coverage. Importantly, there are no occupied surface states above the VBM, indicating that band bending is negligible at zero bias in the p-type Si. Furthermore, tip-induced band bending is also negligible (< ~0.2 eV) in p-type Si(001) at positive sample bias: E_F is shifted downward from mid-gap by doping,

quite close to the top of the Si VBM, and a positive substrate bias can only bend the bands until the VBM at the surface coincides with E_F.[31] The projected density of states (PDOS) on the molecule calculated from the LDA Kohn-Sham eigenvalues exhibits significant dispersion for energies above –12 eV (Figs. 6a, 7a), but is discrete below this value. Examination of the band structure close to the VBM further reveals that molecular states here are strongly coupled with the substrate, with significant band crossing and mixing of states. The highest occupied state with molecular character involves an isolated adsorbate band that is associated mainly with the bare Si dimers. In what follows, we refer to this as the 'dimer + molecule' state (Fig. 8a).

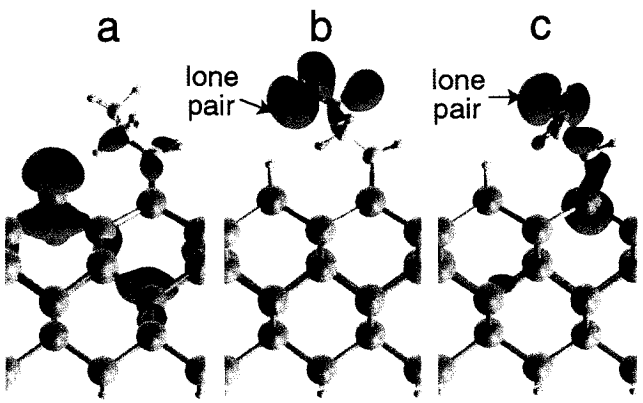

FIG 8. Charge density isocontours (pink) of Γ point Kohn-Sham wavefunctions, associated with (a) 'dimer + molecule' state in C_5H_8 on clean Si(001), and lone pair states in (b) amino-C_5H_8 and (c) pyrroline on H-terminated Si(001). The isocontours are taken at the same value. Decreasing this value yields tails into the Si substrate for (b) as well, reflecting the fact that the wavefunction is not completely localized on the molecule.

To help identify molecule-derived states, we overlay the Kohn-Sham levels of isolated C_5H_{10} on the molecular adsorbate PDOS. C_5H_{10} has the same geometry as the adsorbed C_5H_8 molecule, but with two additional H atoms 1.1 Å from C, along the original C-Si bond. The overlay is performed by aligning the deepest occupied states, the σ_1 levels; clear correspondence is obtained for molecular levels below –12 eV (Fig. 7a). Moreover, prominent PDOS peaks below –3 eV can also be approximately identified with the superimposed levels. In contrast, direct identification is not possible for the PDOS peak at ~ –2 eV and the 'dimer + molecule' state (Fig. 7a). Examination of the wavefunctions indicates that the peak at ~ –2 eV is associated with C-Si bonds. This is consistent with a similar analysis performed with a fully relaxed gas-phase C_5H_8 molecule, where we find that the C-C π bond in C_5H_8, which breaks to form the C-Si bonds, is expected to lie above –2 eV (Fig. 7a).

We now simulate the effect of a positive substrate bias by applying an electric field normal to the substrate. Relaxing the system in the presence of electric fields does not change the atomic structure, with the relaxed system being at most 0.01 eV more stable than the unrelaxed system. The *cis* structure also remains thermodynamically favored over the alternative *trans* structure, which has been previously considered.[10] Analysis of the local potential profile, averaged along the plane of the surface indicates that the external field induces a voltage drop across the molecule that is significantly larger than that across the Si slab. However, no molecular states are driven across the Si VBM up to STM fields of 1.3 V/Å. (STM fields are defined with a tip-sample distance of 10 Å; see Section 6.3.2) For all fields considered, the 'molecular state' closest to the VBM is the 'dimer + molecule' state: the energy of this state is independent of field (Fig.

9a). In contrast, molecular peaks at ~ –4 eV and below do move significantly closer to the VBM with increasing fields, but do not cross the VBM at the fields considered. The broad C-Si peak at ~–2 eV becomes sharper and moves closer to the VBM with increasing field, but the peak maximum remains much smaller compared to the other molecular states at all fields, and level movement is relatively less evident (Fig. 10(a-d)). As a reference, the energy of the sharply-localized σ_1 state increases linearly with field, at a rate of 1.0 eV per 1.0 V/Å. (Reducing the coverage to 0.125 ML does not change the results.) Our calculations show that field-induced changes in level alignment of molecular states relative to the Si VBM are correlated with the degree of localization of the state on the molecule, which is larger for weaker coupling to the substrate. Indeed, we find that Kohn-Sham eigenstates associated with σ_1 have a molecular weight of 1.0. The corresponding values for the molecule-derived peak at –4.0 eV (LDA) are 0.9-1.0, in contrast to 0.2-0.4 for the C-Si peak. (Molecular weights are defined here as the integral of the square of the wavefunction over a spatial region parallel to the Si plane, extending from 1 Å above the molecule to midway between the molecule and surface.)

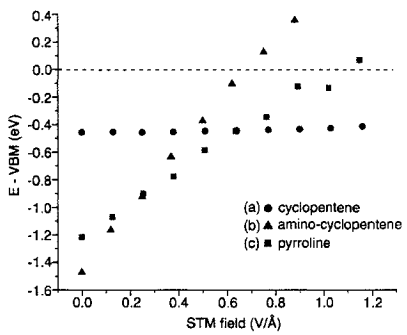

FIG 9. Kohn-Sham eigenvalues versus STM field, for (a) 'dimer + molecule' state in C_5H_8/Si, (b) lone pair state in amino-C_5H_8/Si, and (c) lone pair peak level in pyrroline/Si.

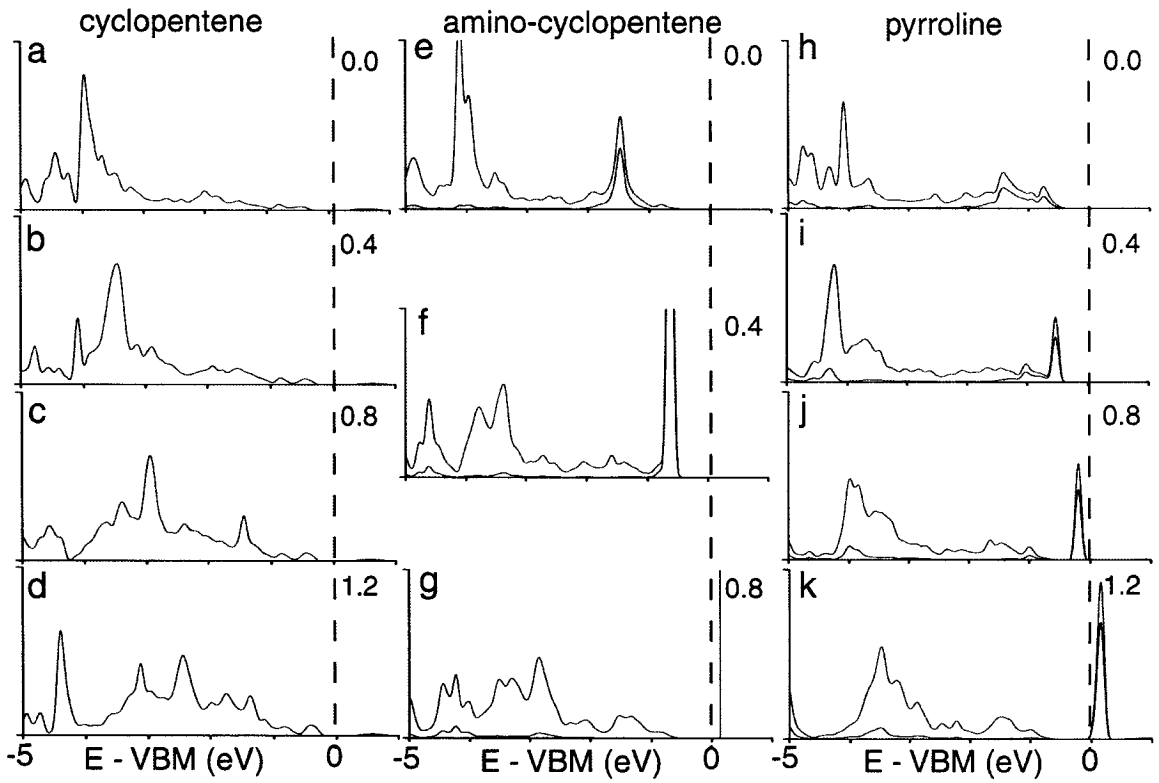

FIG 10. Molecular (blue) and N (red) PDOS as a function of electric field for (a)-(d) cyclopentene/Si, (e)-(f) amino-cyclopentene/Si, and (h)-(k) pyrroline/Si. Values in the top right hand corner of each panel indicates the corresponding STM field in eV/Å.

The NDR reported in Ref. 22 was observed at tip-substrate voltage differences of as small as ~2.5 V. This indicates that the proposed resonant tunneling mechanism is possible only if the molecular state that crosses the VBM is *at most* 2.5 eV below the VBM at zero bias. Since the Kohn-Sham levels cannot provide quantitative spectra, we go one step further and compute the quasiparticle excitation energies within the GW approximation. The self-energy correction to the Si VBM is –0.4 eV, while that for occupied molecular states are > –0.4 eV, resulting in a net shift away from the VBM. The 'dimer + molecule' state has a net self-energy correction of about –0.5 eV (Table 2a);

preliminary calculations indicate that this correction is independent of coverage to within 0.1 eV. Depending on the position in k-space, the corresponding correction is –0.6 to –0.7 eV for states associated with the C-Si peak and –1.0 to –1.1 eV for states associated with the molecular peak at –4.0 eV. In general, we observe a larger self-energy correction for states that are more localized on the molecule. This is consistent with the fact that exchange interaction plays a greater role in stabilizing localized occupied states, while screening, which destabilizes occupied states, is weaker for localized states. Furthermore, the spurious self-interaction terms arising from LDA are larger for localized states. These results show quantitatively that there are no molecular states above –2.5 eV which can be driven into the Si band gap by external electric fields.

	GW energies in eV (LDA values in brackets)	
	Γ point	K point
(a)	-1.1 (-0.6)	-1.1 (-0.5)
(b)	-2.8 (-1.6)	-2.9 (-1.5)
(c)	-1.9 (-1.1)	-2.3 (-1.4)

TABLE 2. Quasiparticle and LDA energies referenced relative to the GW and LDA values of the VBM respectively, of Kohn-Sham wavefunctions associated with (a) 'dimer + molecule' state in cyclopentene on clean Si(001), and lone pair states in (b) amino-cyclopentene and (c) pyrroline on H-terminated Si(001).

The above discussion indicates that the NDR observed in Ref. 22 is not likely to be due to resonant tunneling through intrinsic molecular states. We have also examined

PDOS computed from alternative molecular geometries, including the *trans* configuration as well as structures with extra H atoms (Fig. 11). While additional H atoms reduce the strain at the molecule-Si interface, none of the systems considered here have molecular states that move into the Si band gap with applied fields. In particular, all intrinsic molecular states in the molecule/Si system are associated with strong σ C-C or σ C-H bonds, and are therefore stabilized several eV below the VBM. On the other hand, states closer to the VBM that have molecular character are adsorbate states too strongly coupled to the substrate to respond to applied fields.

As a check, we have also considered geometries involving molecules with C=C double bond character (Fig. 12). The geometries in Fig. 12(a-b) are unlikely to represent the experimental structure because the weaker C-C π bond remains intact in these geometries, while the stronger σ C–H bonds are broken. The geometry in Fig. 12c, however, resembles the proposed three-atom intermediate[8] for the cycloaddition process, and may represent a metastable intermediate for a desorbing molecule. Our results indicate that none of these structures have molecular states which cross the VBM at the critical field; furthermore, the π states in Fig. 12(b-c) are too strongly coupled to the substrate to move significantly relative to applied fields.

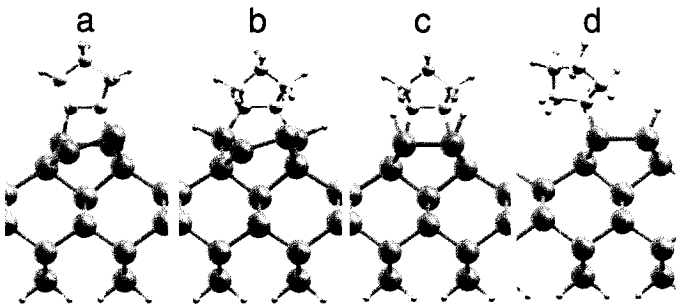

FIG 11. Alternative geometries considered for cyclopentene/Si (no double bond character). (a) trans configuration, (b) H bonded to Si that is attached to C, (c) bare Si dimers passivated with H, (d) single Si-C bond, with H added to passivate dangling bonds.

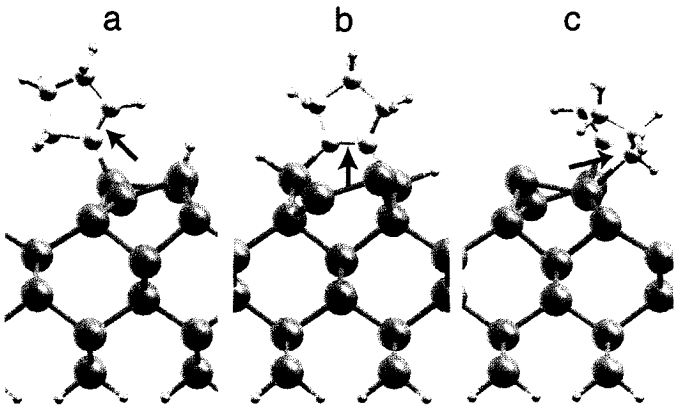

FIG 12. Alternative geometries considered for cyclopentene/Si (with double bond character, indicated by black arrows). These are 1.3 Å in (a-b), and 1.4 Å in (c), in contrast to single C-C bonds with lengths of 1.5 Å.

Similarly, we find that neither B addimers nor substitutional B dopants (immediately beneath the molecule, in subsurface layers, or away from the molecule in an 8-layered slab) lead to molecular states which can cross the VBM. (See Section 6.3.1) Both B-derived states and additional adsorbate states involving B are strongly coupled to the Si substrate; in particular, there is no significant voltage drop across B substituents in

the Si substrate, so that association with B dopants does not decouple the adsorbate states. Furthermore, B addimers as well as surface and subsurface B impurities are three-fold coordinated and therefore are only slightly charged. Our results are also unchanged when a zero external field is imposed in the Si slab to simulate enhanced screening due to B dopants.

Thus, while isolated cyclopentene on B-doped Si(001) exhibits NDR at 80 K,[22] our calculations indicate that the observed NDR is not a result of resonant tunneling through intrinsic molecular states. The reversibility of NDR and existence of a critical field suggest that mechanisms involving molecular desorption or localized tip states are also unlikely to be applicable in this particular experiment, and the origin of the observed NDR remains an open question.

6.2.4 Amino-cyclopentene on H-terminated Si(001)

Since the resonant tunneling mechanism for NDR can potentially provide a direct link between interesting nanoscale transport phenomena and intrinsic molecular states, we now proceed to explore functionalizations generating molecular states that can be driven into the band gap by STM fields. For C_5H_8/Si, we find that only weakly coupled states well-localized on the molecule can move closer to the VBM when a positive substrate bias is applied, but these involve strong σ bonds and lie several eV below the VBM. In contrast, molecular states involving lone pairs, which should be well-localized on the molecule and positioned closer to the VBM, are more likely to be driven into the band gap by applied fields. We explore this effect by functionalizing the molecule with an amine group.

Experimental techniques have been developed to control and characterize the binding of amino-cyclopentene onto exposed Si dimers on a Si(001) substrate that is H-terminated elsewhere, so that the resulting bonding geometry (Fig. 5b for 0.5 ML coverage) is similar to that for C_5H_8/Si.[32] In short, by adding a protective group to the amine and subsequently removing it, it is possible to bind amino-cyclopentene onto the Si(001) surface through cycloaddition of the C=C bond across the Si dimer, instead of through the amine group. The Si(001) substrate used for this process is H-terminated, with H atoms removed at specific positions for binding to the molecule. H passivation of the exposed Si dimers prevents reactions between the unprotected amine group with the bare dimers. Our results and conclusions are unchanged when the clean Si(001) surface is used instead. The adsorption energy for 0.5 ML amino-cyclopentene on H-terminated Si(001) is very similar to that of cyclopentene on clean and H-terminated Si(001) (Table 3).

System	**Adsorption energy (eV)**
0.5 ML cyclopentene/Si	-2.56 (-2.45)
0.5 ML amino-cyclopentene/Si	-2.49
0.5 ML pyrroline/Si	-2.37

TABLE 3. Adsorption energies for different systems at 0.5 ML coverage. For 0.5 ML amino-cyclopentene and pyrroline (where the remaining Si dimer is H-passivated), the adsorption energy is given relative to the gas-phase molecule and a Si(001) surface in the same supercell with half the dimers H-passivated. This adsorption energy is also calculated for cyclopentene on H-terminated Si(001), given in brackets in the 1st row. The adsorption energy for 0.5 ML cyclopentene on clean Si(001) (relative to gas phase C_5H_8 and a clean p(2×1) Si(001) surface) is given without brackets.

The LDA PDOS on the molecule and on N (Fig. 6b) exhibits a sharp peak at –1.5 eV. The wavefunctions associated with this peak are primarily localized on the N lone pair, and we refer to this as the lone pair state (Fig. 8b). States associated with this peak have molecular weights of 0.7-0.9, and have a narrow dispersion of 0.1 eV. By overlaying the levels of amino-C_5H_8 and amino-C_5H_{10} as for C_5H_8/Si, we find that this lone pair state is associated with the molecular HOMO in both cases, with remarkable agreement between the PDOS peak position and the aligned HOMO levels (Figs. 6b, 7b). Application of a positive substrate bias has negligible effect on the atomic geometry. However, in contrast to the adsorbate states in C_5H_8/Si, the energy of the molecule-derived lone pair state increases linearly with applied field, eventually crossing the Si VBM into the band gap at 0.69 V/Å (Figs. 9b, 10(e-g)).

6.2.5 Pyrroline on H-terminated Si(001)

To further explore the effect of N lone pairs, we consider 0.5 ML pyrroline on H-terminated Si(001) (Fig. 5c). Pyrroline is similar to cyclopentene, but with an NH group replacing a CH_2 group in the 5-membered closed ring. X-ray photoelectron spectroscopy (XPS) experiments have shown that pyrroline deposited on clean Si(001) binds to Si dimers either through a N-Si bond, or through cycloaddition (similar to cyclopentene).[5] Heating the sample to 500°C preferentially reduces the XPS signal from the N-Si bonds.[5] The results presented here involve a H-terminated Si(001) surface (similar to amino-cyclopentene/Si) as the experimental technique used to prepare amino-cyclopentene on H-terminated Si(001) results in a more controllable binding geometry and can potentially be applied to pyrroline/Si as well. (Using a clean Si(001) surface instead does not change

our theoretical results.) The adsorption energy for pyrroline on Si(001) is similar to that of amino-cyclopentene and cyclopentene (Table 3).

In contrast to amino-cyclopentene, where N is not part of the closed ring, the state associated with the C-C π bond in pyrroline also has some weight on the N lone pair. Similarly, unlike the sharp lone pair peak in the PDOS for amino-cyclopentene/Si, the highest occupied peak in the N PDOS for pyrroline/Si is broadened, extending from approximately –2.0 to –0.5 eV (Fig. 6c). Overlaying the energy levels of isolated, relaxed pyrroline indicates that the broadened peak can be associated with two molecular levels: the molecular HOMO localized on the N lone pair, and the HOMO–1 state associated with both the C-C π bond and N lone pair (Fig. 7c). Analysis of the wavefunctions also shows that more than one eigenstate at each high symmetry point in the Brillouin Zone has a > 0.5 weight on N in this energy range. These wavefunctions are not completely localized on the N atom but also have substantial weight on the rest of the molecule (Fig. 8c).

The association of C-Si states with the N lone pair is likely to explain the breadth of the lone pair peak. However, in contast to the more strongly coupled adsorbate states in C_5H_8/Si, a positive substrate bias can decouple the lone pair states almost completely. States with energies closer to the VBM become more heavily weighted on the lone pair with increasing bias, resulting in an increasingly narrow lone pair peak (Fig. 10(h-k)). For fields stronger than 0.38 V/Å, an isolated highest occupied band associated with the N lone pair is formed and its energy increases linearly with the applied field, eventually crossing the VBM at ~1.0 V/Å. If we assign a peak level to be the weighted average energy of N-projected states contributing to the lone pair peak, we obtain an

approximately linear relation between this peak level and the STM field strength, starting from zero bias (Fig. 9c). The lone pair peak here moves towards the VBM at a slower rate than in amino-C_5H_8/Si (Fig. 9). This is consistent with the fact that the lone pair state in amino-C_5H_8/Si is more localized on the N lone pair, which is in turn further from the Si substrate than in pyrroline/Si, thus giving rise to a larger field-induced voltage drop across the molecule for driving the state into the VBM.

Finally, we note that in contrast to C_5H_8/Si and amino-C_5H_8/Si, adsorbed pyrroline distorts from its zero bias equilibrium geometry in the presence of an electric field. Specifically, the angle between the N-H bond and the surface normal decreases approximately linearly from 42° at zero bias to 22° at a field of ~1.0 V/Å. The energy stabilization due to relaxation in the fields are fairly small: 0.07 eV at ~1.0 V/Å and smaller for weaker fields. This structural distortion also has negligible effect on the lone pair peak levels at all fields considered. However, the field-induced distortion does decrease the energy of the σ_1 state, by 0.15 eV at a field of ~1.0 V/Å.

6.2.6 Self-energy corrections for amino-C_5H_8/Si and pyrroline/Si

We now proceed to make a more quantitative estimate of the zero bias level alignments in amino-C_5H_8/Si and pyrroline/Si using the GW approximation. For amino-C_5H_8/Si, the GW (LDA) energy of the lone pair state is –2.8 (–1.6) eV at the Γ point and –2.9 (–1.5) eV at the K point of the Brillouin Zone (Table 2b). For pyrroline/Si, eigenstates with the largest molecular weight associated with the lone pair peak have GW (LDA) energies of –1.9 (–1.1) eV at Γ and –2.3 (–1.4) eV at K (Table 2c). The net self-energy corrections reported here are larger for lone pair states in amino-C_5H_8/Si than in

pyrroline/Si. This is consistent with the larger molecular weights of 0.7 and 0.9 in amino-C_5H_8/Si compared to 0.6 and 0.5 in pyrroline/Si.

6.2.7 Concluding remarks

We have performed first principles calculations of cyclopentene, amino-cyclopentene, and pyrroline on Si(001) to explore the possibility of molecular states being driven into the band gap by external fields, a necessary condition for a previously proposed resonant tunneling mechanism[23] for NDR. Our results indicate that this is only possible for states that are sufficiently localized on the molecule and weakly coupled to the substrate. The frontier molecular orbitals in cyclopentene/Si system are adsorbate states that are strongly coupled to the substrate, while weakly coupled molecular states, associated with σ bonds in the molecule, have energies several eV below the VBM. Thus, the NDR observed in low-temperature STM experiments[22] on cyclopentene cannot be explained by resonant tunneling through intrinsic molecular states as previously suggested; its origin remains an open question. In contrast, the addition of N lone pairs to the molecule, either in the form of an amine group or by incorporating N into the closed ring, results in lone pair states near the VBM that can be driven into the band gap with positive substrate biases.

It is important to note that very large fields are required to drive the lone pair states into the VBM in the systems considered here. Therefore, further work is required to optimize the conditions for resonant-tunneling based NDR. Our results allow us to outline some considerations that may be important for this process. Firstly, we have observed that the *rate* at which molecular states move towards the VBM can be enhanced if they are predominantly localized in regions that experience a larger field-induced

voltage drop from the substrate. Molecules with fused rings can be designed to position the N lone pair further from the surface, for example. However, such localization may also reduce the coupling between the orbitals and electrode, resulting in a reduction in current and less pronounced NDR. Secondly, our calculations indicate that N lone pair states have *zero bias alignments* that are closer to the Si VBM compared with intrinsic molecular states associated with σ bonds. This is related to the shallower energy levels of N lone pair states in the gas phase molecules compared with σ states. By choosing molecules with shallow levels and tuning the Fermi level of the substrates (e.g. choosing substrates with larger work functions or taking advantage of quantum confinement in nanowires), it may be possible to fabricate systems with intrinsic molecular states aligned closer to the lead Fermi level.

The resonant tunneling mechanism[23] for NDR is attractive because it potentially relates nanoscale transport characteristics with intrinsic molecular levels of the system. The realization of systems that can exhibit resonant-tunneling based NDR at lower fields will undoubtedly require further experimental efforts to control and characterize the atomic geometry of such systems, and theoretical efforts to understand the electronic coupling, wavefunction character and level alignments in these systems. In this context, a many-electron treatment is essential to determine accurate level alignments, taking into account substrate-induced polarization effects[29] and correcting the Kohn-Sham eigenvalues by as much as ~90% for localized molecular states that are relevant to this problem.

6.3 Additional details

In this section, I provide further details of the work described in Section 6.2; these details were omitted to improve the flow of arguments.

6.3.1 Cyclopentene on B-doped Si(001)

The Si(001) sample in the NDR experiment on cyclopentene/Si (Ref. 22) was degenerately doped with B (resistivity < 0.005 Ω·cm). Based on previously published work,[27] the dopant concentration is about 10^{19} cm^{-3}, or one B dopant for every 5000 Si atoms. The high activation energy for B diffusion in bulk Si (3.40 eV)[33] and the absence of prolonged annealing, as described in Ref. 22, suggest that surface segregation of B dopants is unlikely. Nevertheless, since our results for cyclopentene on undoped Si(001) do not seem to support the resonant tunneling mechanism for NDR, we proceed to explore the influence of B dopants by investigating the effects of electric fields on structures A-D given in Fig. 13. Due to computational limitations, the B concentrations in these structures are about 100 times greater than expected in experiment. However, any effect of B in the experiment is likely to be present also in systems with higher B concentrations.

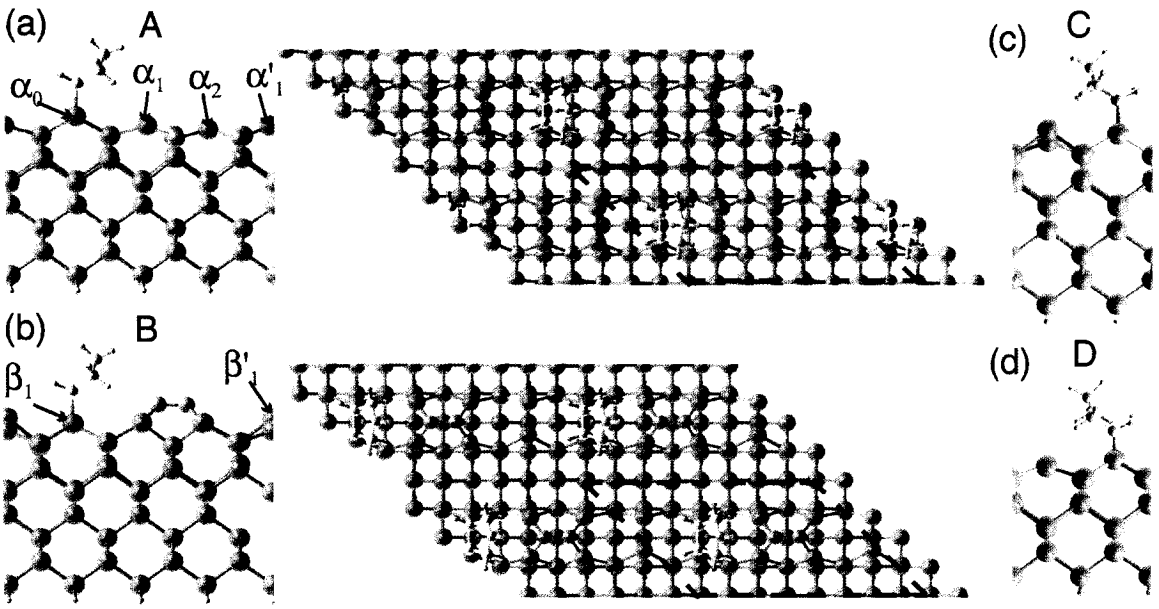

FIG 13. Structures (a) A, (b) B, (c) C and (d) D with B dopants. A and B have a c(4 × 4) unit cell (dashed black boxes in (a) and (b) (top view)), while C and D represent 0.5 ML coverage ((1 × 2) unit cell). Labels in A and B denote adsorption sites considered for the respective B-doped Si(001) surfaces. The numerical subscript denotes the relative number of B neighbors on the Si site. The most favorable adsorption sites, as shown here, are (a) α_0 for Si(001) with subsurface B dimers and (b) β_1 for Si(001) with B addimers.

Structures A and B represent the most favorable adsorption geometries for cyclopentene on a c(4 × 4) Si(001) surface with subsurface B dimers and B addimers respectively. These arrangements of B atoms are the energetically most stable structures reported by Bernholc et. al.[34] for delta-doped B/Si(001) surfaces where a c(4 × 4) reconstruction has been experimentally observed.[35] B dopants are known to prefer subsurface sites while a model of B addimers has also been proposed.[35] These B arrangements correspond to distinct physical regimes: B in the substitutional subsurface

site is 4-fold coordinated while B in the addimer site is 3-fold coordinated. A subsurface B atom forms 4 bonds with Si. On the molecule-free surface, the B-Si bond lengths are 2.17 and 2.06 Å (for bonds involving Si atoms in the 3rd layer), and 1.99 and 1.98 Å (for bonds involving Si surface atoms). On the other hand, a B addimer atom forms 2 bonds with Si and 1 bond with its partner B atom, with a B-Si bond length of 1.94 Å and a B-B distance of 1.65 Å on molecule-free Si(001). The difference in coordination number suggests that the subsurface B atoms are likely to be electrically active (consistent with experiments on delta-doped B/Si(001)) while the B addimer atoms are likely to be more neutral.[35] Indeed, a Bader charge analysis indicates that a subsurface B atom has about 1 *e*/atom more than a B addimer atom. The larger charge transfer for subsurface B is also manifested in changes in buckling angles of the Si(001) surface dimers. On clean B-free Si(001), the dimer buckling angle is calculated to be 18°, in agreement with literature values.[36] This buckling angle is related to the transfer of electrons from the so-called D_{down} atom to the D_{up} atom, resulting in the presence (absence) of an electron lone pair on the D_{up} (D_{down}) atom. D_{up} therefore prefers sp^3 coordination and buckles up, while D_{down} prefers sp^2 coordination and buckles down.[26] The dangling lone pair on D_{up}, being associated with the highest occupied band in Si(001), donates electrons to the B dopants if the B atoms are electrically active. As a result, D_{up} loses its preference for sp^3 coordination, leading to a reduction in the buckling angle for the Si dimer. We find that the buckling angle for the bare Si dimers remains 18° for the surface with B addimers. However, with subsurface B dopants, the buckling angles are 0°, 1° and 14° for α_2, α_1 (and α'_1) and α_0 respectively. The Si atoms attached directly to B (α_1, α'_1 and α_0) are also

lowered in height relative to Si atoms away from B (α_2), in agreement with the literature.[34]

c(4 × 4) structures	Adsorption energy (eV)	d(Si-Si) (Å)
Subsurface B		
α_0 (Structure A)	-2.37	2.35
α_1	-2.07	2.40
α'_1	-2.02	2.40
α_2	-1.71	2.51
B addimers		
β_1 (Structure B)	-2.51	2.35
β'_1	-2.48	2.35
no Boron	-2.55	2.35

TABLE 4. Adsorption energies and d(Si-Si) for c(4 × 4) structures. d(Si-Si) refers to the Si-Si bond lengths for the Si atoms bonded to the molecule. For comparison, the adsorption energy and d(Si-Si) value for 0.5 ML C_5H_8 on a 6-layered Si slab are -2.56 eV and 2.35 Å, very similar to the values in the last row for the undoped c(4 × 4) system with 8 Si layers.

Table 4 gives the adsorption energies for cyclopentene on different adsorption sites on the c(4 × 4) B-doped surfaces. The B addimer does not change the molecular adsorption energy or geometry significantly. The most favorable adsorption site for the system with subsurface B is α_0, the Si dimer farthest from the B dopants. Notice that the corresponding binding energy is 0.18 eV smaller than for the undoped surface, indicating that cyclopentene is more likely to bind far away from B dopants than near the subsurface B. The binding energy decreases successively by 0.3 eV as the molecule is moved closer to the B dopants to sites α_1 (and α'_1) and α_2 respectively. This is consistent with the

partial depletion of charge in Si atoms bonded directly to subsurface B. As cyclopentene binds to Si via covalent C-Si bonds and C is more electronegative than Si, the molecule is expected to prefer electron-rich binding sites. Our calculations indicate that the trend in adsorption energies is related to the strain induced when Si atoms bonded to B also have to share charge with the molecule. Cyclopentene adsorption at α_1, α'_1 and α_2 result in charge depletion from the Si dimer at α_0, with the corresponding buckling angle decreasing from 14° to 0°. This indicates that Si atoms bonded to the molecule contribute less charge to the B dopants, with charge from the Si dimer at α_0 compensating for this effect. Furthermore, the Si-Si bonds in α_1, α'_1 and α_2 weaken when the molecule binds to each of these sites respectively. As shown in Table 4, the corresponding increase in Si-Si bond lengths (d(Si-Si) defined in Table 4) at different adsorption sites appears to be correlated with the trend in adsorption energies. Other geometrical features do not change significantly upon adsorption, and the C atoms directly attached to Si share a C-C bond that is 1.55-1.56 Å for all systems. The molecular PDOS for the different adsorption sites are also similar, with shifts in the σ_1 level being at most 0.2 eV (Table 5).

Adsorption site	$E - E_F$ (eV)
α_0	-16.7
α_1	-16.5
α'_1	-16.6
α_2	-16.5

TABLE 5. Kohn-Sham energies of the low-lying σ_1 state in cyclopentene on B-doped Si(001) at different adsorption sites. Notice that there is no clear correlation between the σ_1 levels and the adsorption energies.

Apart from the above systems, we also consider two other B-doped systems that represent extreme possibilities. In structure C (Fig. 13c), the B atoms are frozen in the bottom half of an 8-layered Si slab, and in structure D (Fig. 13d), the B atom is placed just beneath the cyclopentene molecule.

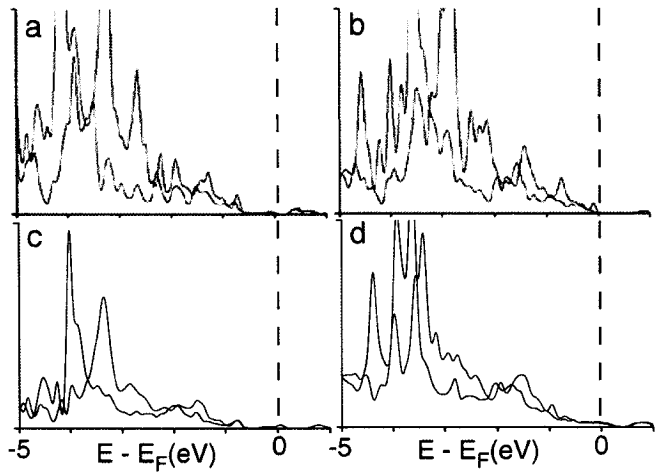

FIG 14. Molecular PDOS at zero bias (black) and in the presence of an electric field (red) in structures (a) A, (b) B, (c) C and (d) D. The electric fields for the red curves are, in eV/Å, 0.48, 0.48, 0.45, 0.35, for (a)-(d) respectively.

Figure 14 shows the molecular PDOS in Structures A-D at zero bias, and at an STM field that is close to (or greater than) the critical field[22] of 0.37 eV/Å in the experiment. The energies are referenced relative to E_F here since the B dopants have been explicitly included in the calculation. Comparison to Fig. 10(a-b) reveals that the presence of B does not change the molecular PDOS significantly. In contrast to amino-cyclopentene and pyrroline on undoped Si (Figs. 10(e-k)), there are no increasingly sharp peaks in the molecular PDOS within 1 eV of E_F. As discussed in Section 6.2.3, there is no significant voltage drop across B substituents in the Si substrate, so that association with B dopants does not decouple the adsorbate states. This is further illustrated in Fig. 15 below, where the B PDOS is approximately independent of applied field, even for the localized B-derived state in Structure C (Fig. 15c). Relaxing the structures in the presence

of the electric field results in negligible changes in atomic and electronic structure (with relaxation energies of at most 0.02 eV). Similar results are found for cyclopentene at other adsorption sites (α_2, α_1, α'_1 and β'_1).

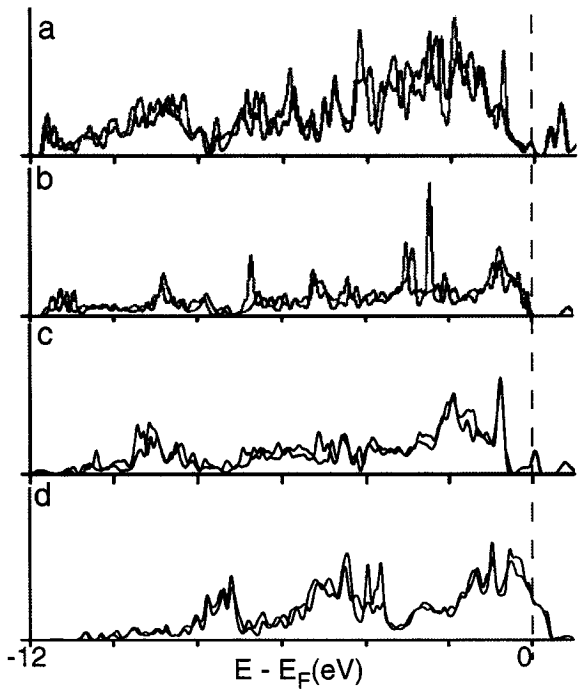

FIG 15. Boron PDOS at zero bias (black) and in the presence of an electric field (red) in structures (a) A, (b) B, (c) C and (d) D. The electric fields for the red curves are given in the caption of Fig. 14.

6.3.2 Further details of methods

The density-functional calculations are performed using the projected augmented wave method[17](energy cutoff 400 eV) using LDA as implemented in VASP.[14] We find that LDA gives comparable results with GGA for atomic structures and relative energies (Section 6.1). Geometry optimization is performed using a force convergence criterion of 0.01 eV/Å. For 0.5 ML coverage, geometry optimization is performed with a Monkhorst-

Pack *k*-point mesh of 2 × 2 except for the metallic B-doped systems (Structures C and D), where a 4 × 4 mesh is used; total energies and densities of states are computed with a denser, Γ–centered mesh of 4 × 4. For the larger c(4 × 4) unit cell, geometry optimization is performed with a Monkhorst-Pack mesh of 2 × 1 while total energies and densities of states are computed with a Γ–centered mesh of 4 × 2.

The Si(001) substrate is modeled by a slab of 6 or 8 Si layers, the bottom layer being passivated by H atoms. The theoretical lattice constant for Si is used (theory: 5.40 Å, experiment: 5.43 Å) and the slab thickness is chosen based on the arrangement of B atoms. The undoped slabs and the slab in Structure D are 6 layer thick: the bottom 2 layers are kept frozen in their bulk positions and the top 4 are relaxed. The c(4 × 4) systems have 8 layer slabs, the top 5 of which are relaxed. In Structure C, there are 8 Si layers, the bottom 4 of which are frozen in their bulk positions (the B atoms are in the 6^{th} Si layer). As mentioned in Section 6.2, the atomic and electronic structure of 0.5 ML cyclopentene on Si is the same whether 6 or 12 Si layers are used to represent the substrate.

Electric fields are applied normal to the slabs. The applied field is linear in the region of the slab and molecule, and drops in the vacuum to maintain periodic boundary conditions. Care is taken to get rid of artificial potential wells in the vacuum that may trap charge. Fig. 16 shows the difference in local potential between a cyclopentene/Si system in the presence of an external applied field, and that of the same system at zero bias, averaged in the plane of the surface. The Si slab is much more effective in screening the field than the molecule. Similar plots are obtained for other fields. We define the 'STM field' as the voltage drop, ΔV, divided by distance Δz, in the region extending from

the top plane of Si atoms to 10 Å above it (10 Å is a typical upper bound to the tip-sample distance in STM). The Si VBM in the presence of applied fields is obtained by adding to the Si VBM at zero bias, an energy difference equal to the change in local potential at the top plane of Si atoms (averaged across the plane). The Si VBM obtained thus is an estimate of that expected for doped Si, with no voltage drop within the Si slab.

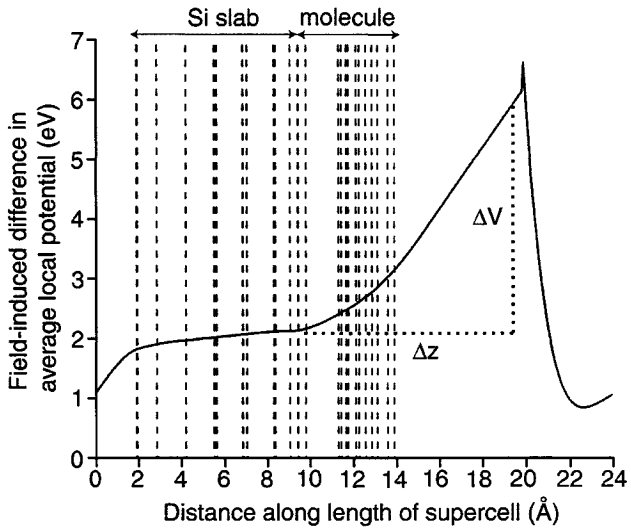

FIG 16. Difference in local potential between a cyclopentene/Si system with an applied external field of 0.30 V/Å, and the same system at zero bias. The local potential is averaged in the plane of the Si surface, and dashed vertical lines mark the atomic planes. Screening is much more pronounced within the Si slab than in the molecule. The STM field, defined by $\Delta V/\Delta z$, is 0.38 V/Å.

References

[1] J. T. Yates, Science **279**, 335 (1998).

[2] R. J. Hamers, J. Hovis, and H. Liu, Acta Phys. Pol. A **93**, 289 (1998).

[3] R. J. Hamers, J. S. Hovis, C. M. Greenlief, and D. F. Padowitz, Jpn. J. Appl. Phys. **38**, 3879 (1999).

[4] G. P. Lopinski, D. D. M. Wayner, and R. A. Wolkow, Nature **406**, 48 (2000).

[5] J. S. Hovis, S. Lee, H. B. Liu, and R. J. Hamers, J. Vac. Sci. Technol. B **15**, 1153 (1997).

[6] J. S. Hovis, H. Liu, and R. J. Hamers, Surf. Sci. **404**, 1 (1998).

[7] J. S. Hovis, H. Liu, and R. J. Hamers, Appl. Phys. A-Mat. **66**, S553 (1998).

[8] J. H. Cho and L. Kleinman, Phys. Rev. B **64**, 235420 (2001).

[9] K. Akagi, S. Tsuneyuki, Y. Yamashita, K. Hamaguchi, and J. Yoshinobu, Appl. Surf. Sci. **234**, 162 (2004).

[10] W. C. Lu, W. G. Schmidt, and J. Bernholc, Phys. Rev. B **68**, 115327 (2003).

[11] M. S. Hybertsen and S. G. Louie, Phys. Rev. Lett. **55**, 1418 (1985).

[12] M. S. Hybertsen and S. G. Louie, Phys. Rev. B **34**, 5390 (1986).

[13] G. M. Rignanese, X. Blase, and S. G. Louie, Phys. Rev. Lett. **86**, 2110 (2001).

[14] G. Kresse and J. Furthmuller, Phys. Rev. B **54**, 11169 (1996).

[15] B. G. Pfrommer, M. Cote, S. G. Louie, and M. L. Cohen, J. Comput. Phys. **131**, 233 (1997).

[16] B. G. Pfrommer, J. Demmel, and H. Simon, J. Comput. Phys. **150**, 287 (1999).

[17] P. E. Blochl, Phys. Rev. B **50**, 17953 (1994).

[18] N. Troullier and J. L. Martins, Phys. Rev. B **43**, 1993 (1991).

[19] M. Rohlfing, P. Kruger, and J. Pollmann, Phys. Rev. B **52**, 1905 (1995).

[20] J. L. Pitters, I. Dogel, G. A. DiLabio, and R. A. Wolkow, J. Phys. Chem. B **110**, 2159 (2006).

[21] H. B. Liu and R. J. Hamers, Surf. Sci. **416**, 354 (1998).

[22] N. P. Guisinger, N. L. Yoder, and M. C. Hersam, PNAS **102**, 8838 (2005).

[23] T. Rakshit, G. C. Liang, A. W. Ghosh, and S. Datta, Nano Lett. **4**, 1803 (2004).

[24] J. L. Pitters and R. A. Wolkow, Nano Lett. **6**, 390 (2006).

[25] N. W. Ashcroft and N. D. Mermin, *Solid State Physics* (Saunders College Publishing, New York, 1976).

[26] E. Kaxiras, *Atomic and Electronic Structure of Solids* (Cambridge University Press, Cambridge, United Kingdom, 2003).

[27] T. Rakshit, G. C. Liang, A. W. Ghosh, M. C. Hersam, and S. Datta, Phys. Rev. B **72**, 125305 (2005).

[28] M. Koentopp, K. Burke, and F. Evers, Phys. Rev. B **73**, 121403(R) (2006).

[29] J. B. Neaton, M. S. Hybertsen, and S. G. Louie, arXiv: cond-mat/0606640 (2006).

[30] S. Machida, K. Hamaguchi, M. Nagao, F. Yasui, K. Mukai, Y. Yamashita, J. Yoshinobu, H. S. Kato, H. Okuyama, and M. Kawai, Journal of Physical Chemistry B **106**, 1691 (2002).

[31] M. McEllistrem, G. Haase, D. Chen, and R. J. Hamers, Phys. Rev. Lett. **70**, 2471 (1993).

[32] Z. Lin, T. Strother, W. Cai, X. P. Cao, L. M. Smith, and R. J. Hamers, Langmuir **18**, 788 (2002).

[33] P. M. Fahey, P. B. Griffin, and J. D. Plummer, Rev. of Mod. Phys. **61**, 289 (1989).

[34] M. Ramamoorthy, E. L. Briggs, and J. Bernholc, Phys. Rev. B **59**, 4813 (1999).

[35] Y. J. Wang, R. J. Hamers, and E. Kaxiras, Phys. Rev. Lett. **74**, 403 (1995).

[36] K. Seino, W. G. Schmidt, and F. Bechstedt, Phys. Rev. Lett. **93** (2004).